




5-2023

## Path Integral Monte Carlo for Entanglement in Bosonic Lattices at $T = 0$

Emanuel Casiano-Diaz

*University of Tennessee, Knoxville, [ecasiano@vols.utk.edu](mailto:ecasiano@vols.utk.edu)*

Follow this and additional works at: [https://trace.tennessee.edu/utk\\_graddiss](https://trace.tennessee.edu/utk_graddiss)

 Part of the [Quantum Physics Commons](#), and the [Statistical, Nonlinear, and Soft Matter Physics Commons](#)

---

### Recommended Citation

Casiano-Diaz, Emanuel, "Path Integral Monte Carlo for Entanglement in Bosonic Lattices at  $T = 0$ ." PhD diss., University of Tennessee, 2023.  
[https://trace.tennessee.edu/utk\\_graddiss/8079](https://trace.tennessee.edu/utk_graddiss/8079)

This Dissertation is brought to you for free and open access by the Graduate School at TRACE: Tennessee Research and Creative Exchange. It has been accepted for inclusion in Doctoral Dissertations by an authorized administrator of TRACE: Tennessee Research and Creative Exchange. For more information, please contact [trace@utk.edu](mailto:trace@utk.edu).

To the Graduate Council:

I am submitting herewith a dissertation written by Emanuel Casiano-Diaz entitled "Path Integral Monte Carlo for Entanglement in Bosonic Lattices at  $T = 0$ ." I have examined the final electronic copy of this dissertation for form and content and recommend that it be accepted in partial fulfillment of the requirements for the degree of Doctor of Philosophy, with a major in Physics.

Adrian Del Maestro, Major Professor

We have read this dissertation and recommend its acceptance:

Cristian Batista, Steven Johnston, Chris M. Herdman

Accepted for the Council:

Dixie L. Thompson

Vice Provost and Dean of the Graduate School

(Original signatures are on file with official student records.)

To the Graduate Council:

I am submitting herewith a thesis written by Emanuel Casiano-Diaz entitled "Path Integral Monte Carlo for Quantum Entanglement in Bosonic Lattices at  $T = 0$ ." I have examined the final paper copy of this thesis for form and content and recommend that it be accepted in partial fulfillment of the requirements for the degree of Doctor of Philosophy, with a major in Physics.

---

Adrian Del Maestro, Major Profes-

sor

We have read this thesis  
and recommend its acceptance:

---

Adrian Del Maestro

---

Chris M. Herdman

---

Steven Johnston

---

Cristian Batista

Accepted for the Council:

---

Dixie Thompson

Vice Provost and Dean of the Graduate School

To the Graduate Council:

I am submitting herewith a thesis written by Emanuel Casiano-Diaz entitled "Path Integral Monte Carlo for Quantum Entanglement in Bosonic Lattices at  $T = 0$ ."

I have examined the final electronic copy of this thesis for form and content and recommend that it be accepted in partial fulfillment of the requirements for the degree of Doctor of Philosophy, with a major in Physics.

Adrian Del Maestro, Major Professor

We have read this thesis  
and recommend its acceptance:

Adrian Del Maestro

---

Chris M. Herdman

---

Steven Johnston

---

Cristian Batista

---

Accepted for the Council:

Dixie Thompson

---

Vice Provost and Dean of the Graduate School

(Original signatures are on file with official student records.)

# Path Integral Monte Carlo for Quantum Entanglement in Bosonic Lattices at $T = 0$

A Dissertation Presented for the  
Doctor of Philosophy  
Degree  
The University of Tennessee, Knoxville

Emanuel Casiano-Diaz

May 2023

© by Emanuel Casiano-Diaz, 2023  
All Rights Reserved.

*To all of my family and loved ones for your unwavering support.*  
*To Abuelo Cano, my dear grandfather for your unconditional love and never ceasing*  
*to show how proud you were. We will miss you dearly.*

# Acknowledgements

During my time in graduate school, I have been beyond lucky to work with a *dream team* of mentors, colleagues, class mates, and friends that have made this undertaking one of the most enriching periods of my life.

First and foremost, I would like to thank my incredible advisor, Adrian Del Maestro. When we first met in Fall 2015 via Skype meeting, I only remember knowing that I wanted to do a master's degree with the thesis focused on a computational physics project. At the time, I could not narrow down my research interests to something more specific and did not consider myself to have the most stellar of undergraduate backgrounds, so I didn't hold my hopes up much, if at all. Somehow, I was then packing my bags on a sunny Summer day in my beloved home of Puerto Rico and heading out to Vermont in June of 2016 to join the Del Maestro Research Group. Graduate school was a completely new ball game to me that nobody in my close circle of friends and family had gone through at the time. Fortunately for me, Adrian was not just an amazing scientist, but an equally amazing person, educator, and advisor, which helped me feel like my graduate school pursuit was a perfectly attainable goal. One of the first things he told me was that his office door would be open to talk about science, a policy that was always proved to be true unless he was already on a meeting. I was also lucky to learn from his own example about other skills needed, or at the very least pretty useful in this trade, such as his second to none organizational skills, pedagogical skills, and the spirit of collaboration always instilled in the Del Maestro Group. My time in this group, which later moved to



UTK, was incredibly enjoyable and partly the reason why I decided to stick around to pursue the PhD too. Thanks to Adrian's support and teachings, I am now here, a few years later down the line, writing this dissertation.

I would also like to thank Hatem Barghathi, a mentor and friend that I was incredibly lucky to meet back in 2016 when he began postdoctoral research in the Del Maestro Group. Countless hours were spent together trying to learn about entanglement entropy calculations when these were new to both of us. Without Hatem's help, I would've had much more difficulties understanding these calculations that now almost seem easy, at least in principle, and have become the basis of my time in graduate school. Even though I was the first student in the group to work directly with Hatem, in the last seven years I have seen how pretty much every single person that has come and gone from the group has benefitted from his tutelage. His almost playful approach to physics and limitless curiosity has been a joy to watch. We are certainly lucky to have him around.

As I transitioned from my master's to PhD project, I began to delve more into quantum Monte Carlo simulations. Around 2018, I was once again fortunate to meet another incredible mentor, Chris Herdman, a former postdoc of the Del Maestro Group, and currently Physics faculty at Middlebury College in Vermont. The way Chris took Path Integral Monte Carlo concepts and explained them in a way that almost made it sound easy and intuitive, even before I ever coded a single quantum Monte Carlo line of code, was simply outstanding. More than 4 years and thousands of lines of PIMC code later, I'm still lucky to be able to work with Chris on an almost weekly basis and get to bounce off ideas on what problems our new Monte Carlo algorithm can help solve and to pick the brains of one of the most "attention to detail" and pedagogically sound kind of scientists that I've gotten to work with.

To every other Del Maestro Group member thank you very much for listening to my weekly updates on how research's going. Way too many times, even if we were not working on the same project, one would come out with a new suggestion, from a different perspective, that would make the difference between spending more time

stuck on a problem, or finally solving it. It was also great to hear you, see your learning process, and even move on to do amazing things outside of the group. To Nathan Nichols, the first PhD student to come out of our group and currently postdoctoral researcher at Argonne National Laboratory, and a friend, special thanks for all the help on the high performance computing side of things. Sometimes I wonder what kind of crazy, inefficient scripts I would be submitting to supercomputing clusters if it were not for your almost unrivaled computational insights.

I would also like to thank Nikolai Prokof'ev, inventor of the PIMC Worm Algorithm for all the insights given that morning in Amherst when I had been working on PIMC for less than a month. The physical and computational insights I learned that day had us hit the ground running with this project at a good pace from the very early stages.

Last but not least, an infinity of gratitude to all my family and loved ones. Whether I was young and trying to be a professional viola player, or then later maybe slightly less young, and now a scientist, your ever present love and support was something I was always fortunate to have. Mamita, China, Mami, Abuelo Cano, Abuela Yiya, Clare, Angel, Abdel, Kelianette, Wally, Tio Edwin, Tio Alex, and all the rest of you, thank you from the bottom of my heart.

# Citations to Published Work

In Chapters 2 and 3, a novel lattice Path Integral Ground State algorithm for the simulation of bosonic lattice models at zero temperature is introduced. The former chapter focuses on the introduction of the algorithm for the estimation of conventional observables, such as ground state energies. The latter, focuses on the algorithm as a tool for the estimation of Rényi full, accessible, and symmetry-resolved entanglement entropies. The work shown in these chapters has been published in SciPost Physics [1]:

“A Path Integral Ground State Monte Carlo Algorithm for Entanglement of Lattice Bosons.”

E. Casiano-Diaz, C. M. Herdman, and A. D. Maestro.

SciPost Phys. 14, 054 (2023).

In Chapter 5, a method for the direct sampling of two dimensional truncated exponential distributions is introduced. This method resulted in the reduction of autocorrelation times for lattice PIGS simulations in the  $1d$  Bose-Hubbard model. The work shown in this chapter is currently released as an Arxiv pre-print [2]:

“Reduction of autocorrelation times in lattice path integral quantum monte carlo via direct sampling of the truncated exponential distribution.”

E. Casiano-Diaz, K. Barros, Y. W. Li, and A. D. Maestro.

arXiv: 2302.04240 (2023)

In my first three years of graduate school, when the Del Maestro Research Group was still based at University of Vermont, I worked on entanglement calculations in fermionic lattice models. This project became a Master’s thesis that I defended in May 2019, from which two papers were published. In the first of these, we study entanglement entropy in the  $t - V$  model of itinerant fermions under a particle bipartition and the results were published in Journal of Statistical Mechanics: Theory and Experiment [3]:

“Particle partition entanglement of one dimensional spinless fermions.”

H. Barghathi, E. Casiano-Diaz, and A. Del Maestro

J. Stat. Mech. Theory Exp. 2017, 083108 (2017).

The second of these papers shows results that directly motivate some of the derivations shown in Chapter 4 for the finite-size scaling of the accessible and symmetry-resolved entanglement entropies in systems with Gaussian local particle number distribution. In this paper, we performed an intensive study of the full and accessible entanglement entropies in the interacting  $t - V$  model. The work was published in Physical Review A:

“Operationally accessible entanglement of one-dimensional spinless fermions.”

H. Barghathi, E. Casiano-Diaz, and A. Del Maestro

Phys. Rev. A 100 (2019).

# Abstract

Path-Integral Monte Carlo Worm Algorithm is one of many Quantum Monte Carlo (QMC) methods that serve as powerful tools for the simulation of quantum many-body systems. Developed in the late 90's, this algorithm has been used with great success to study a wide array of physical models where exact calculation of observables is not possible due to the exponential size of the Hilbert space. One type of systems that have eluded PIMC-WA implementation are lattice models at zero temperature, which are of relevance in experimental settings, such as in optical lattices of ultracold atoms. In this thesis, we develop a PIMC Worm Algorithm for the simulation of interacting bosonic lattices at zero temperature. The algorithm is benchmarked with exact diagonalization by computing conventional estimators, such as kinetic and potential energies, and also quantum entanglement estimators. We implement our algorithm to numerically confirm new finite-size scaling forms that we derive for various entanglement measures, such as the operationally accessible, and symmetry-resolved Rényi entropies in the Bose-Hubbard model. We finalize by introducing a method for the direct sampling of two dimensional truncated exponential distribution for the reduction of autocorrelation times, an example of the algorithmic development that will be needed moving forward to expand the applicability of our algorithm to even more complex systems.

# Table of Contents

<b>1</b>	<b>Introduction</b>	<b>1</b>
1.1	Quantum entanglement . . . . .	1
1.2	Information measures . . . . .	2
1.2.1	Classical Shannon entropy . . . . .	2
1.2.2	von Neumann entropy . . . . .	5
1.2.3	Rényi entanglement entropy . . . . .	6
1.2.4	Accessible Entanglement . . . . .	7
1.3	Bose-Hubbard Model . . . . .	9
1.4	Numerical computation of entanglement . . . . .	11
1.4.1	Monte Carlo (MC) . . . . .	14
1.4.2	Metropolis-Hastings Sampling . . . . .	15
1.4.3	Quantum Monte Carlo (QMC) . . . . .	16
1.5	Entanglement scaling . . . . .	18
1.6	Accessible and Symmetry-Resolved Entanglement Scaling . . . . .	20
1.7	Thesis contributions . . . . .	21
<b>2</b>	<b>Lattice PIGS</b>	<b>24</b>
2.1	Projection onto the Ground State . . . . .	27
2.2	Bose-Hubbard Model . . . . .	29
2.3	Configuration Space . . . . .	30
2.3.1	Off-Diagonal Configurations: Worms . . . . .	32

2.4	Sampling . . . . .	34
2.5	Original Finite Temperature Updates . . . . .	35
2.5.1	Insert/Delete worm (or antiworm) . . . . .	35
2.5.2	Advance/Recede . . . . .	38
2.5.3	Insert/Delete kink before worm head . . . . .	39
2.5.4	Insert/Delete kink after worm head . . . . .	43
2.5.5	Insert/Delete kink before worm tail . . . . .	45
2.5.6	Insert/Delete kink after worm tail . . . . .	45
2.6	New updates for $T = 0$ . . . . .	45
2.6.1	Insert/Delete worm from $\tau = 0$ . . . . .	48
2.6.2	Insert/Delete worm from $\tau = \beta$ . . . . .	51
2.7	Energy benchmarks . . . . .	54
2.8	Kinetic Energy . . . . .	57
2.9	Potential Energy . . . . .	62
<b>3</b>	<b>Rényi entanglement entropies in lattice PIGS</b>	<b>65</b>
3.1	Entanglement Entropy . . . . .	65
3.2	Symmetry-resolved and accessible entanglement entropies . . . . .	67
3.3	Entanglement entropy estimator . . . . .	68
3.4	Accessible and symmetry-resolved entanglement estimators . . . . .	71
3.5	Improved accessible entanglement estimator given limitations of sampling particle number sectors . . . . .	75
3.6	Entanglement entropies via PIGSFLI . . . . .	76
3.7	SWAP Updates . . . . .	77
3.7.1	Insert/Delete SWAP kink . . . . .	77
3.7.2	Advance/Recede along SWAP kink . . . . .	79
3.8	Large Imaginary Time Projection of Entanglement . . . . .	81
3.9	Results . . . . .	81
3.10	Conclusion . . . . .	94

<b>4</b>	<b>Finite Size Scaling of Entanglement in the 1D Bose-Hubbard Model</b>	<b>96</b>
4.1	Entanglement Measures . . . . .	97
4.2	Bose-Hubbard Model . . . . .	98
4.3	Scaling of operationally accessible entanglement . . . . .	99
4.4	Scaling of symmetry-resolved entanglement . . . . .	102
4.5	Luttinger parameter extraction from non-accessible entanglement . . . . .	106
4.6	Conclusion . . . . .	106
<b>5</b>	<b>Improving autocorrelation times via direct sampling of the truncated exponential distribution</b>	<b>109</b>
5.1	Introduction . . . . .	109
5.2	Direct sampling of 1D truncated exponential distribution . . . . .	111
5.3	Direct sampling of 2D truncated exponential distribution . . . . .	115
5.4	Application: Lattice Path Integral Quantum Monte Carlo . . . . .	119
5.5	Conclusions . . . . .	129
<b>6</b>	<b>Discussion and Future Work</b>	<b>131</b>
6.1	Future Work . . . . .	135
6.1.1	Luttinger Parameter Estimation . . . . .	135
6.1.2	Symmetry-resolved entanglement interaction dependence . . . . .	136
6.1.3	Accessible and symmetry-resolved entanglement in two dimensions . . . . .	138
<b>A</b>	<b>Obtaining and Running the Code</b>	<b>168</b>
	<b>Appendix</b>	<b>168</b>
	<b>Vita</b>	<b>173</b>



# List of Figures

1.1	Shannon entropy for the coin flip example as a function of the probability of landing heads. At the extreme cases where the probability is either zero or 1, there is complete certainty of the coin flip outcome, and hence the Shannon entropy vanishes. Maximum uncertainty about the outcome occurs when there is equal probability, 1/2, of landing either side, and the Shannon entropy thus reaches a maximum. The entropy is symmetrical about the dashed vertical line denoting probability 1/2. . . . .	4
1.2	Schematic of the 1d Bose-Hubbard model phase diagram. At large interaction strengths, $U \gg 1$ , the model is in the Mott insulating phase, where bosons strongly repel each other, which in the case of unit-filling, $L = N$ , results in one particle on each site. At weak interaction strengths, the model is in the superfluid phase, where particles are highly non-localized. The superfluid-insulating quantum phase transition occurs at a value of the interaction strength estimated to be in the range $U/t \gtrsim 3.3$ . . . . .	10

- 1.3 Number of basis states making up the Hilbert Space for a Bose-Hubbard Lattice as a function of system size,  $M$  in the case of unit filling,  $M = N$ . For systems of  $M = 32$  sites, the Hilbert Space size is approximately  $10^{17}$  basis states. With the memory required being on the order of  $\mathcal{O}(D_{\text{Hil}}^2)$ , ED quickly becomes unsuitable for the study of larger systems. . . . . 13
- 1.4 Second Rényi entanglement entropy scaling with subsystem cordlength in the  $1d$  Bose-Hubbard model. The system consists of  $L = 64$  sites at unit filling at interaction strengths  $U/t = 3.3$ , near the superfluid-insulating quantum critical point and  $U/t = 2$ , deeper into superfluid phase. The data points were obtained from PIMC and are fitted to Eq. (1.30), shown as a solid line. The estimated central charge for each curve is shown as an annotation, agreeing with the CFT prediction,  $c = 1$ . 22
- 2.1 Example of a 4-site worldline configuration. Paths evolve in the direction of imaginary time (vertical axis) and particles can hop between sites (horizontal axis). Imaginary times at which the Fock state changes have been labeled on the left side of the diagram and the corresponding states are shown to the right. Increasing line thicknesses have been used to denote the addition of a particle to that path segment, and a vertical dashed line indicates the absence of a particle. The segment on site  $i = 0$  extending from imaginary time  $\tau_3$  to  $\tau_5$ , where a particle was spontaneously created and annihilated later, is called a worm and it will be an integral part of our algorithm. The lattice sites are subject to periodic boundary conditions, as illustrated by the particle hopping from site  $i = 3$  to  $i = 0$  at imaginary time  $\tau_7$ . 33

2.2 **Insert/Delete worm.** A worm is inserted by first randomly sampling imaginary times  $\tau_t, \tau_h$  inside an also randomly sampled flat interval, delimited by the times  $\tau_{\text{prev}}$  and  $\tau_{\text{next}}$ . A worm head and tail are then inserted at  $\tau_h$  and  $\tau_t$ , respectively.  $\epsilon$  and  $\epsilon_w$  correspond to the eigenvalues of the diagonal part of the Hamiltonian for Fock states  $|\alpha\rangle$  and  $|\alpha_w\rangle$ , respectively. The case of  $\tau_h < \tau_t$  is also valid and would correspond to an antiworm insertion, in which case a particle is first deleted by the worm head, then one created by the tail. . . . . 36

2.3 **Advance/Recede.** Worm end is selected at random. It is then moved to a randomly sampled time inside the flat interval. The diagram above illustrates the example of advancing/receding a head in imaginary time. Either the worm head or tail can be timeshifted. . . . . 40

2.4 **Insert/Delete kink before head.** A kink is inserted between neighboring sites  $i, j$  before the worm head at a randomly sampled time  $\tau_{\text{kink}} \in [\tau_{\text{min}}, \tau_h)$  and the head moved to the site where the particle hops to. The lower bound of the sampling interval  $\tau_{\text{min}}$  is chosen to be the largest out of the two lower bounds of the corresponding flat intervals. This ensures that the new kink does not interfere with other kinks, which simplifies the implementation. The complementary update is to delete the kink and move the head back to the site from where the particle is hopping from. . . . . 41

2.5 **Insert/Delete kink after head.** A kink is inserted between neighboring sites  $i, j$  after the worm head at a randomly sampled time  $\tau_{\text{kink}} \in [\tau_{\text{h}}, \tau_{\text{max}})$  and the head moved to the site where the particle hops to. The upper bound of the sampling interval  $\tau_{\text{max}}$  is chosen to be the smallest out of the two upper bounds of the corresponding flat intervals. This ensures that the new kink does not interfere with other kinks, which simplifies the implementation. The complementary update is to delete the kink and move the head back to the site from where the particle is hopping from. . . . . 44

2.6 **Insert/Delete kink before tail.** A kink is inserted between neighboring sites  $i, j$  before the worm tail at a randomly sampled time  $\tau_{\text{kink}} \in [\tau_{\text{min}}, \tau_{\text{t}})$  and the tail moved to the site where the particle hops from. The lower bound of the sampling interval  $\tau_{\text{min}}$  is chosen to be the largest out of the two lower bounds of the corresponding flat intervals. This ensures that the new kink does not interfere with other kinks, which simplifies the implementation. The complementary update is to delete the kink and move the tail back to the site from where the particle is hopping to. . . . . 46

2.7 **Insert/Delete kink after tail.** A kink is inserted between neighboring sites  $i, j$  after the worm tail at a randomly sampled time  $\tau_{\text{kink}} \in [\tau_{\text{t}}, \tau_{\text{max}})$  and the tail moved to the site where the particle hops from. The upper bound of the sampling interval  $\tau_{\text{max}}$  is chosen to be the smallest out of the two upper bounds of the corresponding flat intervals. This ensures that the new kink does not interfere with other kinks, which simplifies the implementation. The complementary update is to delete the kink and move the tail back to the site from where the particle is hopping to. . . . . 47

2.8	<p><b>Insert/Delete worm from <math>\tau = 0</math>.</b> A worm is inserted at the <math>\tau = 0</math> edge by inserting a worm head at a randomly sampled time <math>\tau_h \in [0, \tau_{\text{next}})</math> and adding a particle to the segment spanning the interval <math>\tau : [0, \tau_h)</math>. An antiworm can instead be inserted by placing a worm tail at the sampled time and destroying a particle in the segment <math>\tau : [0, \tau_t)</math>.</p>	49
2.9	<p><b>Insert/Delete worm from <math>\tau = \beta</math>.</b> A worm is inserted at the <math>\tau = \beta</math> edge by inserting a worm tail at a randomly sampled time <math>\tau_t \in [\tau_{\text{prev}}, \beta)</math> and adding a particle to the segment spanning the interval <math>\tau : [\tau_t, \beta)</math>. An antiworm can instead be inserted by placing a worm head at the sampled time and destroying a particle in the segment <math>\tau : [\tau_h, \beta)</math>.</p>	52
2.10	<p>Relative error of the ground state kinetic energy (<b>left</b>) and potential energy (<b>right</b>) as a function of <math>\beta t</math> for a Bose-Hubbard chain of <math>L = 8</math> sites at unit-filling. As <math>\beta</math> increases, the relative error decays exponentially to zero, as evidenced by the fits (solid lines). Regimes where the interaction strength is large possess a sizeable energy gap and more accurate results can be obtained at lower <math>\beta t</math> values, since the ground state is projected out of the trial wavefunction much faster. The different shapes and colors correspond to different interaction strengths. The interactions strengths <math>U/t = 0.5, 3.3, 10.0</math> represent values in the superfluid phase, the 1D critical point, and the Mott phase, respectively. The measurement window is <math>\Delta\tau = 0.2\beta t</math>.</p>	56
3.1	<p>Example of worldlines in the two-replica space in which entanglement entropies will be measured. A special type of kink between replicas that we refer to as a SWAP kink can now be inserted or deleted at <math>\tau = \beta/2</math> on the sites that belong to subregion <math>A</math>. In this example, two SWAP kinks are shown on sites <math>i = 0</math> and <math>i = 1</math>.</p>	69

3.2	Example systems: <b>(left)</b> 1D chain under equal spatial bipartitions of size $\ell$ and <b>(right)</b> a square lattice with square spatial subregion of linear size $\ell$ . The total number of sites in the subregions is $m \equiv \ell^D$ . Periodic boundary conditions are used in all cases. . . . .	78
3.3	Insert/Delete <b>SWAP</b> kink. The number of particles at the center of the path, $\tau = \beta/2$ , is measured for the same site on the two different replicas. If the number of particles is the same, then the <b>SWAP</b> kink is inserted. The kinks are shown to form an “X” in the diagram for visual clarity, but they both exist at exactly $\beta/2$ . Kink deletion occurs if the number of particles at $\beta/2$ is the same for site $i$ of both system and replica. In the figure, the replicas are labeled $R$ and $\tilde{R}$ . . . . .	78
3.4	Advance/Recede along <b>SWAP</b> kink. If a worm end, either head or tail is adjacent to a <b>SWAP</b> kink, it can be shifted in the imaginary time direction and moved to the other replica if the new randomly sampled time goes across $\beta/2$ . The diagram above shows the example of advancing/receding a worm head, at time $\tau_h$ , along a <b>SWAP</b> kink and moved to the other replica to a new time, $\tau_{\text{new}}$ . . . . .	80
3.5	Full second Rényi Entropy for a one-dimensional lattice of $L = 16$ sites at unit-filling under an equal spatial bipartition of size $\ell = 8$ . Three-parameter exponential fits in $\beta t$ (solid lines) have been performed on the Monte Carlo results (markers). The dashed horizontal lines denote exact diagonalization values for each of the various interaction strengths. The three-parameter exponential fits the data well and can be used to extrapolate the large $\beta$ limit results of measurements of interest. . . . .	82
3.6	$\beta$ -scaling of relative error of full entanglement $S_2$ for a 1D lattice of $L = 8$ sites at unit-filling. The system is bipartitioned into equally sized subregions $A, B$ of size $\ell = 4$ sites. The relative error of $S_2$ decays as a function of $\beta t$ . The solid lines are simple exponential fits. . . . .	84

- 3.7 **(left)** Full Rényi Entanglement Entropy  $S_2$  for a 1D Bose-Hubbard lattice with  $L = 16$  sites at unit-filling under an equal spatial bipartition of size  $\ell = 8$  at various interaction strengths  $U$ . The entropies were measured from simulations at four different values of  $\beta t$ . As expected, the exact ground state value (solid black line) is approached as  $\beta t$  increases. The vertical dashed line at  $U = 3.3$  is the exact value of the 1D Superfluid-Mott Insulator phase transition. The solid circles are large  $\beta t$  extrapolations of  $S_2$  obtained from a three-parameter exponential fit of  $S_2$  results at  $\beta t = 4, 6, 8, 10, 12$ . **(right)** Full Rényi Entanglement Entropy  $S_2$  for a 1D Bose-Hubbard lattice with  $L = 256$  sites at unit-filling under an equal spatial bipartition of size  $\ell = 128$  at various interaction strengths  $U/t$ . . . . . 85
- 3.8 Finite-size scaling of the second Rényi Entropy in a square lattice of size  $M = 32 \times 32$  at unit-filling for various subregion sizes. The subregions are made up of lattice sites arranged as squares of linear sizes  $\ell = 1, 2, \dots, 20$ . The entanglement is seen to increase linearly with the boundary of the subregion. The data is fit to a linear model with a sub-leading correction term that is logarithmic in  $\ell$ , as shown in Eq. (3.35), yielding  $a \approx 0.2, b \approx 0.5$ , and  $c \approx -0.6$ . The interaction strength was fixed to a value near the  $2D$  critical point. The inset shows a plot of  $S_2$  minus the leading term in Eq. (3.35), exposing the logarithmic dependence in  $\ell$  of the subleading term. . . . . 87
- 3.9  $\beta$ -scaling of the accessible entanglement  $S_2^{\text{acc}}$  in a 1D chain of  $L = 8$  sites at unit-filling under equal bipartition of size  $\ell = 4$ . In contrast to the full Rényi entanglement entropies, larger values of  $\beta$  are needed to achieve similar accuracy, especially in the superfluid phase. The solid horizontal lines denote the exact value of the accessible entanglement at the respective interaction strength. . . . . 89

3.10	Imaginary time projection length $\beta$ -scaling of the symmetry-resolved entanglement $S_2(\rho_{A_n})$ in a 1D Bose-Hubbard chain of $L = 8$ sites at unit-filling under an equal spatial bipartition of size $\ell = 4$ . From top to bottom, the rows correspond to interaction strengths in the superfluid phase ( $U/t = 0.5$ ), at the phase transition ( $U/t = 3.3$ ), and in the Mott phase ( $U/t = 10$ ). The first three columns correspond to entanglement entropies in the maximal local particle number sector $n_{\max}$ (i.e., with the largest probability), and the two neighboring sectors $n_{\max} - 1$ and $n_{\max} + 1$ . The solid horizontal lines are the exact diagonalization values for each symmetry resolved entanglement entropy. The rightmost column shows the local particle number distribution $P_n$ at each of the three interaction strengths. . . . .	91
3.11	Symmetry-resolved Rényi entanglement entropies as a function of local particle number sector, $n$ . The system is a one-dimensional lattice of $N = 64$ bosons at unit-filling under an equal spatial bipartition $\ell = 32$ near the critical interaction strength $U/t = 3.3$ . The bottom panel shows the local particle number distribution, $P_n$ , for this system. . . .	93
4.1	Accessible entanglement scaling with subsystem cordlength. The system consists of $L = 64$ sites at unit filling with interaction strengths $U/t = 2.0$ , in the superfluid phase, and $U/t = 3.3$ , near the superfluid-insulating quantum critical point. The data points were obtained from PIMC and are fitted to Eq. (4.10), shown as a solid line. Fit parameters are shown as annotations, with the central charge agreeing with the CFT prediction, $c = 1$ . . . . .	101



4.2	Scaling of the symmetry-resolved entanglement with subsystem scaling. The results shown correspond to the local particle number sector where the probability distribution, $P_n$ , is maximal, $n_{\max}$ , and adjacent sector, $n_{\max} - 1$ . Monte Carlo data points are fitted to Eq. (4.20) and the corresponding fit parameters are shown as annotations. . . . .	105
4.3	Extraction of Luttinger Parameter, $K$ , via fit to $e^{2\Delta S_2(\ell)}$ . The scaling form obtained for the difference $\Delta S_2$ is doubled and then exponentiated to obtain a linear relation in $D(\ell)$ from which the slope is directly proportional to $K$ . Near the critical interaction strength, Renormalization Group theory predicts that $K_c = 2$ [4], with its value increasing deeper in the superfluid phase, at lower interaction strengths.	107
5.1	One dimensional truncated exponential distribution Eq. (5.1) generated via rejection sampling (top) and direct sampling (bottom). For the number of samples shown (800,000), both methods successfully generate the desired one dimensional truncated exponential distribution of the random variate $x$ . The direct sampling data is closer to the exact distribution (solid curve) because it includes more good samples.	113
5.2	Kolmogorov-Smirnov (KS) test results. The KS-distance is plotted as a function of number of samples for two sampling methods. The KS-distance is smaller for the direct sampling dataset, which indicates that it better estimates the true one dimensional truncated exponential distribution, Eq. (5.1). . . . .	114
5.3	Two dimensional truncated exponential distributions, Eq. (5.4), generated via rejection and direct sampling. The heatmaps on the top row show the exact, rejection sampled, and directly sampled distributions for parameters $a = 0.1$ , $b = 1.5$ and $c = 2.0$ , with the relative error of each method compared to the exact shown in the bottom row. $8 \times 10^5$ samples of $x_1$ and $x_2$ each were used. . . . .	118

5.4	Cumulative average of $\langle x_1 \rangle$ , $\langle x_2 \rangle$ , and $\langle x_1 x_2 \rangle$ as a function of number of samples. The values of $x_1$ and $x_2$ have been sampled from the two dimensional truncated exponential distribution, Eq. (5.4), via rejection sampling and direct sampling. For all three averages, the dataset obtained via direct sampling converges faster to the exact result (horizontal line). . . . .	120
5.5	Example of a worldline configuration in Path Integral Monte Carlo for 2 particles on 4 lattice sites. The paths propagate in the direction of imaginary time (vertical) and space (horizontal). Three kinks are shown at imaginary times $\tau_1, \tau_2, \tau_3$ and occur due to a particle hopping between adjacent sites. More configurations can be sampled by performing updates on the worm shown with tail at $\tau_4$ and head at $\tau_5$ . Some estimators, like the kinetic energy, involve averaging a quantity, such as the number of kinks, over a window of user defined width centered around $\tau = \beta/2$ . . . . .	123
5.6	Integrated autocorrelation times for the ground state kinetic (top) and potential (bottom) energy estimators of the one dimensional Bose-Hubbard model obtained via path integral Monte Carlo as a function of system size, $L$ at unit filling: $L = N$ . Lower is better. The insets show the ratio of autocorrelation times obtained by sampling using direct and rejection (uniform distribution) methods for the one and two dimensional truncated exponential distributions. . . . .	126
5.7	Autocorrelation times for the ground state kinetic (top) and potential (bottom) energy estimators of the one dimensional Bose-Hubbard Model obtained via Path Integral Monte Carlo as a function of projection length, $\beta$ . Lower is better. The insets show the ratio of autocorrelation times obtained by sampling using direct and rejection (uniform distribution) methods for the one and two dimensional truncated exponential distributions. . . . .	128

5.8	Wall clock times for path integral Monte Carlo simulations for a 1D Bose-Hubbard lattice of size $L = N = 12$ at $U/t = 3.3$ using rejection (R) and direct (D) sampling of the truncated exponential distribution. Results are shown for 10 independent runs for each method starting from different random seeds and $10^6$ samples of the kinetic and potential energies were collected. The wall times did not change significantly when using different sampling schemes, with an average ratio of wall times $t^D/t^R = 1.02 + / - 0.01$ . . . . .	130
6.1	Scaling of bipartite fluctuations with the log of the cordlength for a $1d$ Bose-Hubbard chain of 64 bosons at unit filling, subject to periodic boundary conditions, and at interaction strength $U/t = 3.5$ , near the phase transition. The extracted Luttinger parameter is close to the prediction from Luttinger Liquid theory near the critical point, $K_c = 2$ . Finite size scaling analyses can be performed to extract a more accurate location of the superfluid-insulating phase transition. . . . .	137
6.2	Interaction dependence of the symmetry-resolved entanglement. These results have been obtained via exact diagonalization (ED). The maximal sector, $n_{\max}$ , and the $n_{\max} - 2$ sector peak near the superfluid-insulating phase transition (vertical line) although at different sides of it. We would like to use PIGSFLI to better understand the scaling of these peaks. For the $n_{\max} - 1$ sector, the symmetry-resolved entanglement saturates at $\ln 2$ in the insulating phase and vanishes in the superfluid, a result seen and explained in chapter 3 of this thesis.	139

# Chapter 1

## Introduction

### 1.1 Quantum entanglement

An entangled quantum many body system exhibits non-classical correlations between its constituents. Formally, a system partitioned into two subregions  $A$  and  $B$  is entangled if its wavefunction cannot be factored into a tensor product of the subregion states:

$$|\Psi\rangle \neq |\Psi_A\rangle \otimes |\Psi_B\rangle, \quad (1.1)$$

where  $|\Psi\rangle$  is the state of the system, which exists in a tensor product Hilbert Space of the two subregions:  $|\Psi\rangle \in \mathcal{H} = A \otimes B$ .

In the entanglement literature, the system is most commonly partitioned into contiguous spatial subregions, but other types of partitions can be chosen, such as subsets of particles [3, 5–7]. Focus will be given to the case of entanglement under a spatial bipartition into subsystems  $A$ , comprised of  $m$  lattice sites and a complementary subregion  $B$ , with the remaining  $M - m$  sites. Under this type of partition, states are represented in second quantization, where a state  $|\Psi\rangle = |n_1\rangle \otimes |n_2\rangle \cdots \otimes |n_N\rangle$  is characterized by the set of occupation numbers on each site.

In an entangled system, performing a measurement in  $A$ , in general gives information about subregion  $B$ . This information gain can be quantified via

von Neumann and Rényi entanglement entropies, which are quantum information theory analogs of the Shannon and Rényi entropies from classical information theory. The degree of entanglement between subsystems is proportional to these entanglement entropies. In the next section, information measures relevant to quantum entanglement quantification are reviewed after discussing the classical Shannon entropy for intuition.

## 1.2 Information measures

The probabilistic nature of quantum mechanics make it ideal for the application of information measures. Moreover, these information measures can be directly used for entanglement quantification. In this section, we give an overview of some information measures from classical and quantum information theory. To build intuition, first the Shannon entropy is introduced and an example is worked out to illustrate how much information is gained from the outcome of a simple classical probabilistic event, a coin flip. Then, we introduce the von Neumann entropy and the Rényi entanglement entropies used for quantification of entanglement.

### 1.2.1 Classical Shannon entropy

The Shannon entropy gives the average amount of information gained from an event in which the possible outcomes occur according to some probability distribution. It is defined as:

$$S = - \sum_i p_i \log_b p_i, \tag{1.2}$$

where the sum is carried over all possible outcomes and  $p_i$  is the probability of outcome  $i$ , with  $p_i > 0$ . The base  $b$  can be chosen arbitrarily depending on the context, but we will use  $e$  such that  $\log_b \rightarrow \ln$  for the remainder of this work. To give some intuition about how information gain can be estimated with Eq. (1.2), consider a regular coin flip. Disregarding all physical effects that could bias the outcome, heads or tails

randomly occur with equal probability,  $1/2$ . Since there is no bias towards any of the two possible outcomes of the coin flip, the information gain should be maximal. The Shannon entropy for this case is:

$$\begin{aligned} S &= -\frac{1}{2} \ln \frac{1}{2} - \frac{1}{2} \ln \frac{1}{2} \\ &= \ln 2 \\ S &\approx 0.69 \dots \end{aligned}$$

Now, consider a coin weighted such that it is more likely to land heads than tails. For the sake of this example, heads shall occur with probability  $2/3$  and tails with  $1/3$ . Since heads is now twice as likely to occur, more certainty about the outcome is known before the coin flip and thus the information gain must now be less. Shannon entropy gives:

$$\begin{aligned} S &= -\frac{2}{3} \ln \frac{2}{3} - \frac{1}{3} \ln \frac{1}{3} \\ S &\approx 0.64 \dots \end{aligned}$$

In Fig. 1.1, the Shannon entropy for the weighted coin flip example is plotted as a function of the probability of landing heads. For both the case where the probability of landing heads is low or that it is high, there is more certainty about the coin flip's outcome. When it is low, it is known with high certainty that the coin will probably land tails, and hence the information gained is low. Similarly, when there is high probability of landing heads, there is no much information gained, and once again the entropy is low. In the case of a fair coin, where both sides have probability  $1/2$ , there is the most uncertainty of the outcome and thus the Shannon entropy reaches a maximum. Notice the symmetry of the Shannon entropy about probability  $1/2$ , denoted by the vertical line.

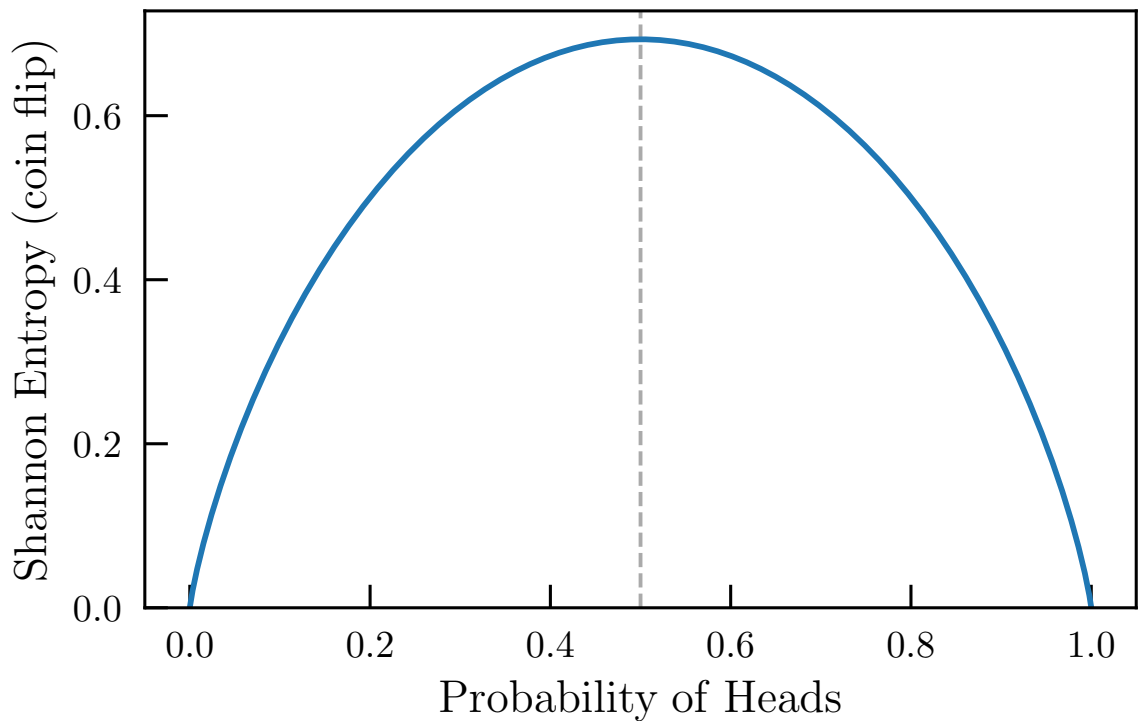


**Figure 1.1:** Shannon entropy for the coin flip example as a function of the probability of landing heads. At the extreme cases where the probability is either zero or 1, there is complete certainty of the coin flip outcome, and hence the Shannon entropy vanishes. Maximum uncertainty about the outcome occurs when there is equal probability,  $1/2$ , of landing either side, and the Shannon entropy thus reaches a maximum. The entropy is symmetrical about the dashed vertical line denoting probability  $1/2$ .

In an entangled system, entanglement entropies behave similarly in that they quantify the information gained about the state of one of the system's partitions after performing a measurement in the other. Now with the intuition obtained from this classical example, the quantum information theory analog of the Shannon entropy, the von Neumann entropy, will be presented.

### 1.2.2 von Neumann entropy

From the Shannon entropy example, notice that the probabilities of random events occurring had to be known. In a quantum many-body system, the probabilities of system configurations are encoded in its reduced density matrix,  $\rho_A$ , obtained by tracing out the degrees of freedom in subregion  $B$  from the full density matrix,  $\rho$ :

$$\rho_A = \text{Tr}_B \rho = \sum_b \langle \psi_b | \Psi | \psi_b \rangle, \quad (1.3)$$

where the sum is carried over all possible  $B$  states,  $\psi_b$ , and the full density matrix is:

$$\rho = |\Psi\rangle\langle\Psi|, \quad (1.4)$$

where  $|\Psi\rangle$  is the state of the system, defined in a tensor product Hilbert Space of the two subregions:  $|\Psi\rangle \in \mathcal{H} = A \otimes B$ . Normalization ensures that the trace of the density matrix is unity,  $\text{Tr} \rho = 1$ . The von Neumann entropy quantifies the information gained about subsystem  $B$  by performing a measurement on subsystem  $A$  and is defined as:

$$S_{\text{vN}} = -\text{Tr} \rho_A \ln \rho_A. \quad (1.5)$$

The density matrix can be obtained via exact diagonalization of the ground state Hamiltonian, but due to the exponentially large size of the Hilbert space, memory requirements also grow exponentially, limiting system sizes. Entanglement can be



calculated for larger systems in Quantum Monte Carlo (QMC) methods via the Rényi entanglement entropy (EE).

### 1.2.3 Rényi entanglement entropy

In QMC [1, 7–17] and even experimentally [18–20], entanglement can be computed via the Rényi entanglement entropy:

$$S_\alpha(\rho_A) = \frac{1}{1-\alpha} \ln \text{Tr} \rho_A^\alpha, \quad (1.6)$$

where  $\alpha$  is the Rényi index. In the limit  $\alpha \rightarrow 1$ , we can show that the Rényi EE becomes the von Neumann entropy:

$$\lim_{\alpha \rightarrow 1} S_\alpha(\rho_A) = \lim_{\alpha \rightarrow 1} \frac{1}{1-\alpha} \ln \text{Tr} \rho_A^\alpha, \quad (1.7)$$

The trace of the reduced density matrix is unity,  $\text{Tr} \rho_A = 1$ , which means that taking the limit  $\alpha \rightarrow 1$  will give an indeterminate form  $0/0$ . Instead, apply L'Hopital's rule:

$$\begin{aligned} \lim_{\alpha \rightarrow 1} S_\alpha(\rho_A) &\stackrel{\text{(H)}}{=} - \lim_{\alpha \rightarrow 1} \frac{d}{d\alpha} \ln \text{Tr} \rho_A^\alpha \\ &= - \lim_{\alpha \rightarrow 1} \frac{\frac{d}{d\alpha} \text{Tr} \rho_A^\alpha}{\text{Tr} \rho_A^\alpha} \\ &= - \lim_{\alpha \rightarrow 1} \text{Tr} \frac{\frac{d}{d\alpha} \rho_A^\alpha}{\text{Tr} \rho_A^\alpha} \\ &= - \lim_{\alpha \rightarrow 1} \text{Tr} \frac{\rho_A^\alpha \ln \rho_A}{\text{Tr} \rho_A^\alpha} \\ &= - \text{Tr} \frac{\rho_A \ln \rho_A}{\text{Tr} \rho_A} \\ \lim_{\alpha \rightarrow 1} S_\alpha(\rho_A) &= - \text{Tr} (\rho_A \ln \rho_A) = S_{\text{vN}}(\rho_A). \end{aligned} \quad (1.8)$$

In QMC methods, the second Rényi EE,  $S_2 = -\text{Tr} \rho_A^2$ , can be measured by writing the purity,  $\text{Tr} \rho_A^2$ , as the expectation value of a unitary  $\text{SWAP}_A$  operator that exchanges the state of  $A$  subregions between two identical replicas of a system,  $\text{SWAP}_A |a_1, b_1\rangle \otimes$

$|a_2, b_2\rangle = |a_2, b_1\rangle \otimes |a_1, b_2\rangle$  [8]:

$$S_2(\rho_A) = -\ln \text{Tr} \rho_A^2 = -\ln \langle \text{SWAP}_A \rangle. \quad (1.9)$$

The density matrix cannot be directly accessed in QMC, but  $\langle \text{SWAP}_A \rangle$  can be sampled. In principle, higher integer Rényi indices can also be sampled in QMC, but  $\alpha$  identical copies of the system are needed, which is computationally expensive. We will focus on the case of  $\alpha = 2$ , where only two copies of the system are needed.

### 1.2.4 Accessible Entanglement

Superselection rules (SSR), such as particle number, charge, or spin conservation restrict the amount of entanglement that is accessible as a resource for quantum information processing [21, 22]. Local operations on the state are limited to those that do not violate the global SSR.

As a simple, yet illustrative example, consider a system of one particle confined to two spatial modes  $A$  and  $B$  corresponding to site occupations, that conserves global particle number  $N = 1$ . For the state  $|\Psi\rangle = (|1\rangle_A \otimes |0\rangle_B + |0\rangle_A \otimes |1\rangle_B)_{\text{resource}} / \sqrt{2}$ , the von Neumann entropy, Eq. (1.5), gives that  $S_1 = \ln 2$ . We can in principle try to transfer the entanglement from this state (resource) into an unentangled register,  $|0, 0\rangle_{\text{register}}$ , by acting with local operators  $\text{SWAP}_A$  and  $\text{SWAP}_B$ , which exchange the modes in the  $A$  or  $B$  subregions, respectively, between register and resource:

$$\text{SWAP}_A |\phi\rangle_{A,\text{register}} \otimes |\psi\rangle_{A,\text{resource}} = |\psi\rangle_{A,\text{register}} \otimes |\phi\rangle_{A,\text{resource}}, \quad (1.10)$$

but this in general can violate the particle number SSR:

$$\begin{aligned} & \text{SWAP}_A \text{SWAP}_B |0, 0\rangle_{\text{register}} \otimes (|1, 0\rangle + |0, 1\rangle)_{\text{resource}} \\ &= (|1, 0\rangle + |0, 1\rangle)_{\text{register}} \otimes \underbrace{|0, 0\rangle_{\text{resource}}}_{N \neq 1; \text{SSR violated}}. \end{aligned}$$

In the entanglement transfer protocol described above, local operations resulted in an apparently entangled register, albeit at the cost of violating total particle number, which is not physically possible. Local operations will result in the accessible entanglement being less or equal to the full entanglement.

In Ref. [21], it was shown that the maximal amount of entanglement transferrable as a resource for quantum for information processing can be computed by averaging the von Neumann entropy over sectors of fixed local particle,  $n$ , in subregion  $A$ :

$$S_1^{\text{acc}}(\rho_A) = \sum_n P_n S_1(\rho_{A_n}), \quad (1.11)$$

where  $P_n$  is the probability of having  $n$  particles in subregion  $A$ , and  $\rho_{A_n}$  is the reduced density matrix of  $A$  projected onto the subspace of fixed local particle  $n$ :

$$\rho_{A_n} = \frac{\Pi_n \rho_A \Pi_n}{P_n}, \quad (1.12)$$

with  $\Pi_n$  the projection operator onto the  $n$  subspace. In Ref [22], the accessible entanglement entropy was generalized to the case of arbitrary Rényi EE:

$$S_\alpha^{\text{acc}}(\rho_A) = \frac{\alpha}{1-\alpha} \ln \left[ \sum_n P_n e^{\frac{1-\alpha}{\alpha} S_\alpha(\rho_{A_n})} \right], \quad (1.13)$$

which becomes  $S_1^{\text{acc}}$  in the limit  $\alpha \rightarrow 1$ . The quantity,  $S_\alpha(\rho_{A_n})$ , is known as the symmetry-resolved entanglement entropy of sector  $n$ . In this thesis, we introduce a novel QMC algorithm with the goal of investigating the entanglement properties (Rényi, accessible, and symmetry-resolved) of an experimentally relevant model of interacting bosons on a lattice, the Bose-Hubbard model.

### 1.3 Bose-Hubbard Model

The Bose-Hubbard model describes interacting itinerant bosons on a lattice and it is defined as [23]:

$$H = -t \sum_{\langle i,j \rangle} b_i^\dagger b_j + \frac{U}{2} \sum_i n_i(n_i - 1) - \mu \sum_i n_i, \quad (1.14)$$

where  $t$  is the tunneling between neighboring lattice sites  $\langle i, j \rangle$ ,  $U > 0$  is a repulsive interaction potential,  $\mu$  is the chemical potential, and  $b_i^\dagger (b_i)$  are bosonic creation (annihilation) operators on site  $i$ , satisfying the commutation relation:  $[b_i, b_j^\dagger] = \delta_{i,j}$ , with  $n_i = b_i^\dagger b_i$  the local number operator.

A schematic of the phase diagram of the one dimensional Bose-Hubbard model is shown in Fig. 1.2. At strong interaction strength,  $U/t \gg 1$ , the system is in the Mott insulating phase, where bosons are highly localized and, in the case of unit filling, which will be our focus, they repel each other resulting in a particle occupancy of unity on each lattice site. At weak interaction strengths, the system is a superfluid, where bosons are highly non-localized. The insulating-superfluid quantum phase transition is of the Berezinskii–Kosterlitz–Thouless (BKT) type, with its precise location being a subject of numerous research studies [24–39], with most recent estimates placing its value at  $U/t \gtrsim 3.3$ .

We will choose the basis states spanning the Hilbert space to be the set of Fock states, or number occupation states:

$$|\alpha\rangle = |n_0^\alpha, n_1^\alpha \dots, n_{M-1}^\alpha\rangle \quad (1.15)$$

where  $n_i^\alpha$  is the number of bosons on site  $i$  for the configuration  $\alpha$  and  $M = L^d$  is the total number of sites in a  $d$ -dimensional hypercubic lattice.

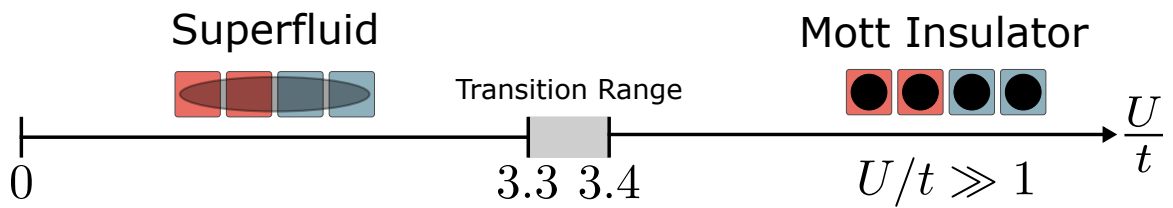


**Figure 1.2:** Schematic of the 1d Bose-Hubbard model phase diagram. At large interaction strengths,  $U \gg 1$ , the model is in the Mott insulating phase, where bosons strongly repel each other, which in the case of unit-filling,  $L = N$ , results in one particle on each site. At weak interaction strengths, the model is in the superfluid phase, where particles are highly non-localized. The superfluid-insulating quantum phase transition occurs at a value of the interaction strength estimated to be in the range  $U/t \gtrsim 3.3$ .

In this basis, the kinetic term of the Hamiltonian is off-diagonal, and the interaction and chemical potential terms constitute are diagonal:

$$H_0 \equiv \frac{U}{2} \sum_i n_i(n_i - 1) - \mu \sum_i n_i \quad (1.16)$$

$$H_1 \equiv -t \sum_{\langle i,j \rangle} b_i^\dagger b_j . \quad (1.17)$$

Explicit expressions for matrix elements in this basis can be obtained, which yield:

$$\epsilon_\alpha \equiv \langle \alpha | H_0 | \alpha \rangle = \frac{U}{2} \sum_i n_i^\alpha (n_i^\alpha - 1) - \mu \sum_i n_i^\alpha \quad (1.18)$$

$$H_1^{\alpha',\alpha} \equiv \langle \alpha' | H_1 | \alpha \rangle = -t \sum_{\langle i,j \rangle} \sqrt{n_j^\alpha (n_i^\alpha + 1)} \delta_{n_i^{\alpha'}, n_i^\alpha + 1} \delta_{n_j^{\alpha'}, n_j^\alpha - 1} \prod_{k \notin \{i,j\}} \delta_{n_k^{\alpha'}, n_k^\alpha} . \quad (1.19)$$

In Chapters 2 and 3, we will develop a Path Integral Ground State (PIGS) Monte Carlo QMC algorithm for lattice bosons at zero temperature ( $T = 0$ ) that will allow for the simulation of Bose-Hubbard lattices and the computation of Rényi, accessible, and symmetrized-entangled entropies.

## 1.4 Numerical computation of entanglement

The size of the Hilbert Space grows exponentially with system size. This makes the density matrix too large for analytical calculation except for small and trivial systems. Computational methods instead are employed for the calculation of entanglement entropies, the most ubiquitous being exact diagonalization (ED) [3, 40–43], density matrix renormalization group (DMRG) [44–48], and quantum Monte Carlo (QMC) [1, 7–17].

ED is a powerful numerical tool which, among other applications, allows for numerically exact results for the entanglement entropies across the phase diagram of the Bose-Hubbard model. The main limitation of this method is that due to the exponentially large size of the Hilbert Space, building and diagonalizing the

Hamiltonian also requires an exponentially large amount of memory. In Fig. 1.3, the size of the ground state Hamiltonian is shown as a function of system size,  $M$ , in the Bose-Hubbard model at unit filling,  $M = L^d = N$ . The size of the Hilbert Space grows as  $D_{\text{Hil}} = (N + M - 1)!/N!(M - 1)!$  and exact diagonalization of the Hamiltonian takes memory space on the order of  $\mathcal{O}(D_{\text{Hil}}^2)$  [49], quickly making memory requirements too large even for relatively small systems. Systems such as the largest one shown in the figure,  $M = 32$ , with  $D_{\text{Hil}} \approx 10^{17}$  are clearly intractable with ED. Nevertheless, such a system can easily be studied using our novel lattice PIGS algorithm. In this thesis, systems as large as  $M = 1032$  at unit filling, and in two dimensions, will be shown (Chapter 3).

To the best of our knowledge, the most state of the art ED calculation in the Bose-Hubbard model relies on the representation of the Hilbert Space using an integer basis to drastically reduce memory requirements [41]. With this astute integer basis representation, ED has been used to calculate the Rényi spatial EE and accesible EE exactly in any regime of the phase diagram of the  $1d$  Bose-Hubbard model in systems of up to  $N = 20$  bosons at unit-filling,  $L = N$ , bipartitioned into  $\ell = \lceil L/2 \rceil$  sites, where  $f(x) = \lceil x \rceil$  is the least-integer or ceiling function [41], with the required memory being less than 1.5 terabytes (TB).

DMRG methods allow for the computation of entanglement for large systems sizes. Due to the exponentially large size of the Hilbert space, the degrees of freedom are truncated in practice in order to obtain the DMRG representation of the ground state [45]. For the Bose-Hubbard model, it is common to work in the particle occupation basis, where the Hilbert space is truncated by enforcing an upper limit,  $n_{\text{max}}$ , on the on-site particle number [24, 50]. The validity of this truncation can be judged by computing conventional observables, such as the ground state energy. It has been seen that for quantities that are highly dependent of particle number fluctuations, such as entanglement measures, large errors occur in regimes where these particle fluctuations are large [41].

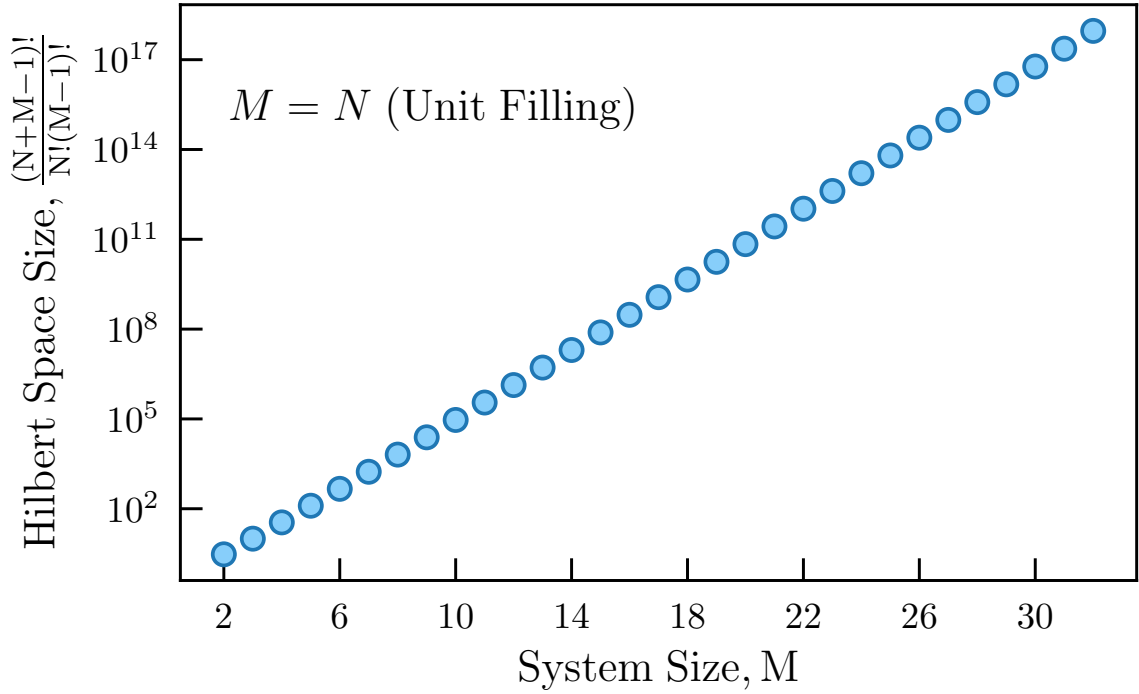


**Figure 1.3:** Number of basis states making up the Hilbert Space for a Bose-Hubbard Lattice as a function of system size,  $M$  in the case of unit filling,  $M = N$ . For systems of  $M = 32$  sites, the Hilbert Space size is approximately  $10^{17}$  basis states. With the memory required being on the order of  $\mathcal{O}(D_{\text{Hil}}^2)$ , ED quickly becomes unsuitable for the study of larger systems.



These errors thus hinder the capability of DMRG for entanglement entropy computation inside the superfluid phase of the Bose-Hubbard model, where particle fluctuations are large. In order to study larger systems and at any interaction strength value of the Bose-Hubbard model, quantum Monte Carlo (QMC) methods need to be employed.

### 1.4.1 Monte Carlo (MC)

Monte Carlo methods are a set of numerical algorithms that rely on repeatedly sampling random numbers to obtain the solution of physical and mathematical problems, typically the approximation of a complicated sum or integral. To develop some intuition, consider the case of performing a high-dimensional integration:

$$I = \int d\mathbf{x} F(\mathbf{x}), \quad (1.20)$$

where  $F(\mathbf{x})$  is a generic high-dimensional function of the vector  $\mathbf{x}$ . Without loss of generality,  $F(\mathbf{x})$  can be factored into the product of a probability density,  $\pi(\mathbf{x})$ , and a function  $f(\mathbf{x}) = F(\mathbf{x})/\pi(\mathbf{x})$  and the integral becomes:

$$I = \int d\mathbf{x} f(\mathbf{x})\pi(\mathbf{x}) \equiv \langle f(\mathbf{x}) \rangle, \quad (1.21)$$

where  $\langle \dots \rangle$  denotes an expectation value. For a large number of random samples,  $N_{\text{samples}} \gg 1$ , the value of the integral can be estimated as:

$$\langle f(\mathbf{x}) \rangle \approx \frac{1}{N_{\text{samples}}} \sum_{i=1}^{N_{\text{samples}}} f(\mathbf{x}_i), \quad (1.22)$$

where the random samples,  $f(\mathbf{x}_i)$ , are drawn according to the probability density  $\pi(\mathbf{x})$ . Monte Carlo expectation values also possess an associated variance,  $\sigma^2 = \langle f^2(\mathbf{x}) \rangle - \langle f(\mathbf{x}) \rangle^2$ , from which the error bars can be computed. Different methods are used to compute the error bars, such as jackknife, bootstrap and binning analysis.

Ref [51] provides an excellent introduction to error bar estimation using various methods. The variance of a Monte Carlo expectation value decreases with the number of samples as  $\sigma^2 \sim 1/\sqrt{N_{\text{samples}}}$  [51, 52], and thus in the asymptotic limit,  $N_{\text{samples}} \rightarrow \infty$ , the expectation value becomes exact.

Even though direct methods exist for the direct sampling of random samples from the probability density,  $\pi(\mathbf{x})$  [2, 53], it is not always possible to do so in general. Instead, schemes to indirectly sample the desired probability density are needed. These are known as Markov Chains. To ensure convergence of  $\pi(\mathbf{x})$ , the Markov Chain must satisfy two conditions. First, an equilibrium probability density  $\pi_{\text{eq}}(\mathbf{x})$  needs to exist. A sufficient, but not necessary condition to satisfy this stationarity is via the Principle of Detailed Balance [53]. That is, that the number of times in the Markov process that the transition  $\mathbf{x} \rightarrow \mathbf{x}'$  occurs, must be equal to the number of times that the transition  $\mathbf{x}' \rightarrow \mathbf{x}$  occurs. This statement can be mathematically posed as:

$$\pi(\mathbf{x})T(\mathbf{x} \rightarrow \mathbf{x}') = \pi(\mathbf{x}')T(\mathbf{x}' \rightarrow \mathbf{x}), \quad (1.23)$$

where  $\pi(\mathbf{x})$  is the probability density function of the configurations and  $T(\mathbf{x} \rightarrow \mathbf{x}')$  is the transition probability from  $\mathbf{x} \rightarrow \mathbf{x}'$ . The second condition that needs to be satisfied is that of ergodicity. This means that in an infinitely long Markov Chain, every possible configuration should be generated in an aperiodic way. The set of updates that can satisfy this ergodicity will depend on the specific Monte Carlo algorithm and configuration space.

## 1.4.2 Metropolis-Hastings Sampling

An ubiquitous sampling algorithm that is employed in Monte Carlo simulations that satisfies detailed balance is Metropolis Sampling [54]. In Metropolis Sampling, any probability density function can be sampled, as long as a function is known that is proportional to it:

$$W(\mathbf{x}) \propto \pi(\mathbf{x}) = \pi(\mathbf{x})/\mathcal{Z}, \quad (1.24)$$

where  $\mathcal{Z}$  is the normalization constant of the stationary distribution,  $\pi(\mathbf{x})$ . The computation of the normalization  $\mathcal{Z}$  is often difficult as the size of the configuration space increases, but thanks to the Metropolis-Hastings algorithm, computing  $\mathcal{Z}$  is not needed since it will cancel out when setting up the Detailed Balance condition. First, proceed by factoring the transition probability into a product of an a priori sampling probability,  $P(\mathbf{x} \rightarrow \mathbf{x}')$  and an acceptance probability,  $A(\mathbf{x} \rightarrow \mathbf{x}')$ :

$$T(\mathbf{x} \rightarrow \mathbf{x}') = A(\mathbf{x} \rightarrow \mathbf{x}')P(\mathbf{x} \rightarrow \mathbf{x}'). \quad (1.25)$$

Substituting these factorized transition probabilities and also  $W(\mathbf{x}) = \pi(\mathbf{x})/\mathcal{Z}$  into Eq. (1.23), the Detailed Balance condition becomes:

$$\frac{W(\mathbf{x})}{\mathcal{Z}}A(\mathbf{x} \rightarrow \mathbf{x}')P(\mathbf{x} \rightarrow \mathbf{x}') = \frac{W(\mathbf{x}')}{\mathcal{Z}}A(\mathbf{x}' \rightarrow \mathbf{x})P(\mathbf{x}' \rightarrow \mathbf{x}). \quad (1.26)$$

Notice that by replacing the stationary distribution with proportional functions led to the cancellation of the normalization constants,  $\mathcal{Z}$ .

In Metropolis-Hastings sampling, a transition  $\mathbf{x} \rightarrow \mathbf{x}'$  will be accepted by drawing a uniformly distributed random number,  $r \sim U(0, 1)$ , and comparing to the acceptance ratio,  $R$ . If  $r < R$ , then the transition occurs. Otherwise, the transition is rejected and the system stays in the same configuration.

### 1.4.3 Quantum Monte Carlo (QMC)

At the interface of Quantum Mechanics and Monte Carlo simulation are Quantum Monte Carlo Methods (QMC) methods. These methods provide a way to simulate quantum systems and estimate expectation values of observables and other physical quantities of interest, such as entanglement entropies, without the need to diagonalize the exponentially large Hamiltonian. There is a zoo of QMC methods, some of them being Variational Monte Carlo, Diffusion Monte Carlo, Reptation Monte Carlo,

Gaussian quantum Monte Carlo, Path Integral Monte Carlo, Path Integral Ground State Monte Carlo, among others.

Recall from Eq. (1.9) that the second or higher integer (i.e,  $\alpha \geq 2; \alpha \in \mathbb{Z}$ ) Rényi EE's can be sampled in QMC by rewriting these in terms of the expectation value of the  $\text{SWAP}_A$ , which can be estimated in simulations performed on a replicated configuration space [8].

Before starting work on this thesis project, QMC methods existed that allowed for the computation of entanglement in many different bosonic or fermionic, and discrete or continuous physical systems [7–9, 11, 12], but there was still an absence of a zero temperature QMC algorithm for the simulation of soft core interacting bosonic lattice models. Our choice of QMC method to fill this algorithmic gap was a special case of the Path Integral Monte Carlo (PIMC) for the simulation of  $T = 0$  systems, Path Integral Ground State quantum Monte Carlo, or PIGS.

PIGS utilizes the projection of a trial wave function in imaginary time to obtain stochastically exact results for the ground state of a quantum many-body system:

$$|\Psi_0\rangle \propto e^{-\beta H} |\Psi_T\rangle, \quad (1.27)$$

where  $e^{-\beta H}$  is the density operator and the projection becomes exact in the limit of infinitely large powers of it. PIGS has been previously formulated in first quantization for non-relativistic Hamiltonians in the spatial continuum [55, 56] and in second quantization on a lattice at finite temperature [57–60].

The configuration space in the PIGS algorithm is a set of paths that extend in the imaginary and spatial directions, known as worldlines. The set of worldline configurations can be sampled via Worm Algorithm updates [57, 61]. The so called worm in the Worm Algorithm is formally inserted into the worldline configurations by creating a particle, via a bosonic creation operator, at an imaginary time, then destroying a particle at a later imaginary time, via a bosonic annihilation operator. The worm has been shown to result improved dynamics in PIMC and allows this

algorithm to also operate in the grand canonical ensemble [57, 61]. In Chapter 2, we introduce a novel set of ergodic worm updates that allows for the simulation of bosonic lattices at  $T = 0$ , where the breaking of imaginary time translational variance results in a new topology of the worldline space and traditional,  $T > 0$ , worm updates do not suffice to satisfy ergodicity.

State of the art, large scale PIGS in the continuum has allowed for the study of the entanglement properties, including confirmation of an entanglement area law [62], in  $3d$  space for superfluid  $^4\text{He}$  [10]. Similar investigations of entanglement properties, such as its finite size scaling are now possible in the Bose-Hubbard model thanks to our new lattice PIGS algorithm.

## 1.5 Entanglement scaling

The information shared between partitions of an entangled quantum many-body system can only be shared across their boundary. With entanglement entropies being measures of information, these quantities then depend directly on the size of this boundary. Many, but not all, quantum many-body systems obey an entanglement area law [10, 62–64]; that is, that the entanglement grows proportionally to the area of the boundary between subregions,  $S_2 \sim \ell^{d-1}$ , where  $d$  is the spatial dimension of the system and  $\ell$  the linear size of the boundary. Area laws were first observed by Bekenstein and Hawking in the context of the entropy of black holes [65–67].

Sub-leading terms of the entanglement finite-size scaling can encode universal numbers. For example, in the  $2d$  Bose-Hubbard model, the second Rényi EE scales as:

$$S_2(\ell) = a\ell + b \ln \ell + c, \tag{1.28}$$

where  $a$ ,  $b$ , and  $c$ , fit parameters. The subleading logarithmic correction  $b$  and constant  $c$  have been shown to contain universal information about the number of Goldstone modes and central charge underlying the conformal field theory [67–72].

In  $1d$  systems where the continuum limit is described by a conformal field theory, Rényi entanglement entropies scale logarithmically with subsystem size [73, 74]:

$$S_\alpha(\rho_A) \sim \frac{c}{6} \left(1 + \frac{1}{\alpha}\right) \ln \ell, \quad (1.29)$$

where  $\alpha$  is the Rényi index,  $c$  is the central charge underlying the CFT, and  $\ell$  is the subsystem size. This result has been confirmed numerically and it has been shown that in the superfluid phase of the Bose-Hubbard model, the central charge is  $c = 1$  [75], due to equivalence between superfluids and Tomonaga Luttinger Liquids [4]. As a preview of the capabilities of the lattice PIGS algorithm that will be introduced in this thesis, in Fig. 1.4 we show data obtained with it for the second Rényi EE as a function of the natural logarithm of the subsystem cordlength. The subsystem size  $\ell$  is replaced by the cordlength to account for distances measured on a ring (i.e,  $1d$  chain with periodic boundary conditions). The entanglement data is then fitted to Eq. (1.29) with  $\alpha = 2$ , with an additive constant:

$$S_2 = \frac{c}{4} \ln D(\ell) + \text{const.} \quad (1.30)$$

The results in Fig. 1.4 already illustrate several of the strengths of our novel lattice PIGS algorithm. First, the system, which consists of  $N = 64$  particles at unit filling,  $L = N$ , is much larger than what would be possible with  $ED$ . Second, the central charge  $c = 1$  was reliably extracted from the fit. And third, that the simulation works for phases of the Bose-Hubbard model with large particle fluctuations, such as the superfluid phase. In this phase, DMRG error is large for expectation values that depend strongly on particle fluctuations [41], due to the truncation of the on-site particle number. Here, only interaction strengths representative of the superfluid

phase,  $U/t = 2.0$ , and near the phase transition,  $U/t = 3.3$ , are shown. In Chapter 2,  $S_2$  is computed as a function of interaction strength for all phases of the Bose-Hubbard model in a chain of  $N = 256$  bosons at unit-filling, with the results resembling the ones obtained from an experiment done in an optical lattice of four  $^{87}\text{Rb}$  atoms [18].

## 1.6 Accessible and Symmetry-Resolved Entanglement Scaling

For the accessible entanglement entropy, there was still no known finite size scaling form, to the best of our knowledge. In Ref. [42], it was seen that the difference between the full and accessible entanglement entropy,  $S_\alpha - S_\alpha^{\text{acc}}$ , could be related to the variance of the local particle number distribution in the subsystem,  $\sigma^2 = \mathcal{F} = \langle n \rangle^2 - \langle n^2 \rangle$ , for systems in which this distribution is Gaussian:

$$S_\alpha - S_\alpha^{\text{acc}} = \frac{1}{2} \ln \sigma^2 + \frac{1}{2} \ln [2\pi\alpha^{1/\alpha-1}]. \quad (1.31)$$

The local particle number variance, or bipartite fluctuations, have been previously used as an entanglement-like measure and for the detection of quantum critical points [39, 76, 77] and in  $1d$  systems it has been found that they scale logarithmically with subsystem size:

$$\mathcal{F}(\ell) \equiv \langle n \rangle^2 - \langle n^2 \rangle \sim \frac{K}{\pi^2} \ln(\ell), \quad (1.32)$$

where  $K$  is the Luttinger liquid parameter [4]. We propose and show in Chapter 4 that the relationships between the entanglement difference shown above and the finite-size scaling fluctuations can be combined to obtain finite-size scaling forms for the operationally accessible entanglement entropy in  $1d$  systems with Gaussian local particle number probability distribution.

For the symmetry-resolved EE, the finite-size scaling has been previously obtained in a calculation employing the replica trick and twist-field operators in the spin- $\frac{1}{2}$   $XXZ$  chain [78]. In Chapter 4, it is shown that this finite-size scaling can also be obtained from entanglement and bipartite fluctuations in  $1d$  systems with Gaussian probability distribution. The scaling is seen to exhibit the property of entropy equipartition; that the scaling with subsystem size is independent of symmetry-resolved sector (i.e, local particle number sector) [78, 79].

Our novel lattice PIGS algorithm provides a tool to numerically confirm the obtained scaling forms. With it, we are able to compute the accessible entanglement in the  $1d$  Bose-Hubbard model for  $N = 64$  bosons at unit-filling,  $L = N$ , beyond the reach of exact diagonalization. These PIGS results for the accessible and symmetry-resolved entanglement scaling are obtained for an interaction strength value near the superfluid-insulating phase transition, and at a weaker interaction strength, deeper into the superfluid phase where DMRG has been seen to have large error due to the truncation of maximum on-site particle number in this phase where particle fluctuations are large [41].

## 1.7 Thesis contributions

A summary of the most important contributions of this thesis include: (1) the introduction of the ground state PIGSFLI algorithm. (2) the associated open source code base [80], (3) new estimators for the efficient measurement of Rényi entanglement entropies within the lattice path integral framework. (4) Results for the spatial entanglement entropy in the 1D and 2D Bose-Hubbard model both at the quantum critical point, and across the superfluid-insulator phase diagram for much larger system sizes than had been previously studied, and without any local restrictions on bosonic site occupations. (5) A finite size scaling analysis of subleading corrections near the 2D superfluid-insulator quantum critical point which can encode universal properties of the interacting system.



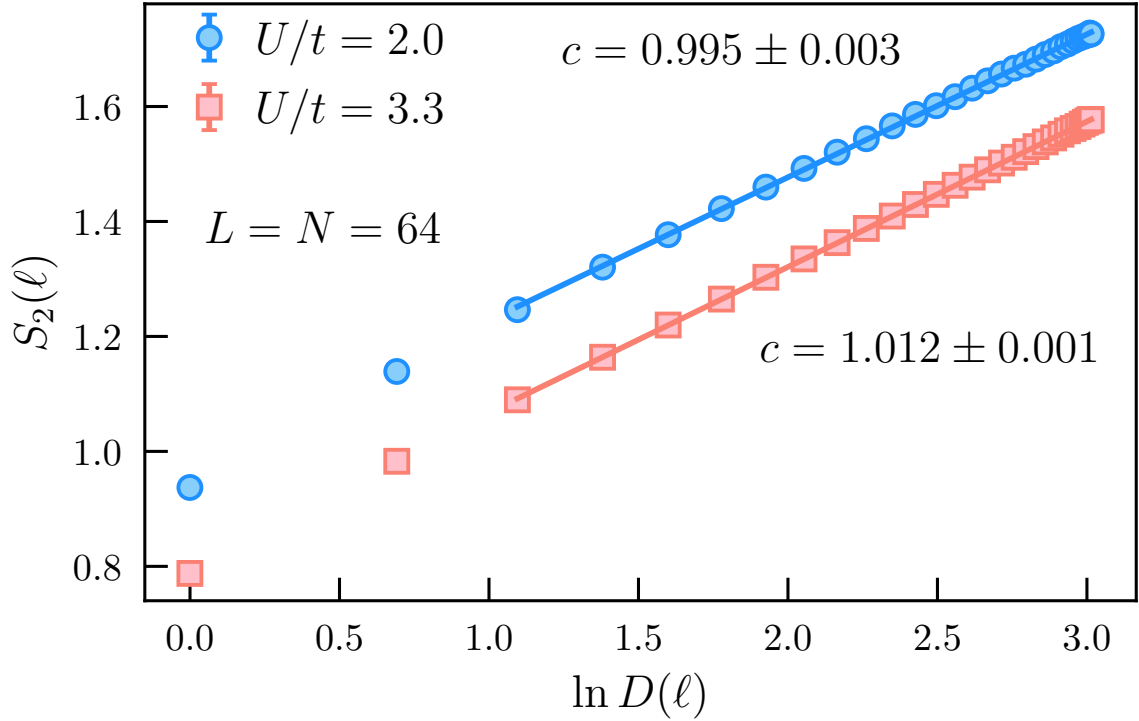


**Figure 1.4:** Second Rényi entanglement entropy scaling with subsystem cordlength in the  $1d$  Bose-Hubbard model. The system consists of  $L = 64$  sites at unit filling at interaction strengths  $U/t = 3.3$ , near the superfluid-insulating quantum critical point and  $U/t = 2$ , deeper into superfluid phase. The data points were obtained from PIMC and are fitted to Eq. (1.30), shown as a solid line. The estimated central charge for each curve is shown as an annotation, agreeing with the CFT prediction,  $c = 1$ .

(6) Particle number distributions and symmetry resolved entanglement in the superfluid, critical, and Mott insulating regimes of the 1D Bose-Hubbard model, where a strong dependence of the symmetry resolved entanglement with respect to the local particle number is interpreted in terms of interactions between quasiparticles. (7) Derivation and numerical confirmation of finite size scaling of accessible and symmetry-resolved entanglement in one dimensional systems with Gaussian local particle number distribution. (8) The introduction of a method for the direct sampling of  $2d$  truncated exponential distributions that results in the reduction of autocorrelation times in lattice PIMC data.

We believe that the new algorithm has wide utility in the measurement and quantification of quantum correlations in bosonic lattice models and can be extended to model current and next-generation experiments on lattice gases. The ability to measure the symmetry resolved and operationally accessible entanglement in such systems has direct implications for the exploitation of correlated superfluid and insulating phases as entanglement resources for quantum information processing.

To facilitate the reproduction of results presented in this work, and to promote further exploration using the PIGSFLI algorithm, the C++ source code has been released [80]. The scripts used to process the raw Monte Carlo data [81, 82], along with the processed data files and scripts used to generate most of the plots in this thesis are also available in public repositories [83, 84].

# Chapter 2

## Lattice PIGS

The advent of replica based methods in quantum many-body systems have provided a route to measuring entanglement entropies – a quantification of the amount of non-classical information shared between a bipartition of a pure state – without the need to construct the full density matrix via full state tomography [73]. Instead, the purity (related to the Rényi entanglement entropy) can be directly obtained via the expectation value of a local observable that is accessible in experimental quantum simulators based on ultra-cold lattice gases [20]. While the replica trick and its related SWAP algorithm have been implemented in numerical quantum Monte Carlo simulations to measure Rényi entropies at zero temperature [7, 8, 11, 17, 85] and the associated mutual information for finite temperature mixed states [15, 86–88] in many physical scenarios (e.g. localized spin systems, lattice fermions, and continuum quantum fluids), they have yet to be extended to the case of fully itinerant and indistinguishable softcore lattice bosons where experiments are presently possible [18, 19].

The bosonic Hamiltonians of relevance to these systems, both in the continuum and on a lattice, can be exactly simulated without a sign problem in any dimension via path integral Monte Carlo (PIMC) [55, 57, 61]. Of particular importance is the Worm Algorithm [58, 61, 89–91], which expands the configuration space of  $d+1$  dimensional

worldlines to include discontinuous paths representing finite particle trajectories in imaginary time. The imaginary-time dynamics of these *worms* improve ergodicity and allow for the direct sampling of the bosonic Hilbert space at finite temperature [58, 92], and open source packages implementing the algorithm are available [59, 60, 80]. At zero temperature, PIMC has a projector variant known as path integral ground state Monte Carlo (PIGS) that has been previously implemented for non-relativistic bosons in the spatial continuum [56, 93], with other Monte Carlo methods inspired by the PIGS formalism applied to spin models and fermionic lattices [94]. A continuous imaginary time  $T = 0$  variant of PIMC for lattice bosons has been elusive in the literature. This algorithmic gap is relevant to the physical modeling of experiments of ultracold atoms confined to optical lattices [95], where finite temperature PIMC require an extrapolation in temperature to properly describe ground state properties [96, 97], as well as the measurement of entanglement [18, 19] highlighted above.

In this thesis, we address both of these issues by introducing a zero temperature worm algorithm projector lattice quantum Monte Carlo algorithm (PIGS For Lattice Implementations or PIGSFLI) extending finite temperature PIMC to ground state calculations [80] where the Rényi entanglement entropy can be computed. Its domain of applicability includes any  $d$ -dimensional bosonic lattice Hamiltonian with arbitrary range interactions and hopping and it scales linearly in the total number of lattice sites ( $L^d$ ) and the projection length  $\beta$  such that Monte Carlo updates in the algorithm scale as  $O(\beta L^d)$ . The quantum Monte Carlo (QMC) method operates in the Fock space of bosonic occupation vectors  $|n_1, \dots, n_{L^d}\rangle$  with projection to the ground state proceeding from a trial state  $|\Psi_T\rangle$ . Here, a physically motivated choice for  $|\Psi_T\rangle$  can lead to a significant acceleration in algorithm convergence. In practice, any ground state expectation value can be obtained to arbitrary precision by performing simulations at different values of the imaginary time projection length  $\beta$  and performing an exponential fit to extract the  $\beta \rightarrow \infty$  result.

Working within an expanded configuration space consisting of  $\alpha$  independent copies of the imaginary time worldlines, the *replica trick* [73] is used to derive an

efficient estimator for the  $\alpha^{\text{th}}$  Rényi entanglement entropy using the SWAP algorithm [8] adapted to bosonic Hilbert space. While the PIGSFLI algorithm naturally operates in the grand canonical ensemble with the average filling fraction  $\langle n \rangle = \langle N \rangle / L^s$  controlled by a chemical potential  $\mu$ , by restricting updates that change the number of particles away from a target value ( $N$ ), the canonical ensemble can also be efficiently simulated at  $T = 0$ . In this case, where the number of particles is fixed, the symmetry resolved Rényi entanglement entropy [21, 22, 98] can be computed by projecting into the subspace of fixed local particle number in a spatial subregion. This latter quantity is important as it sets an upper bound on the amount of entanglement that could be extracted from the many-body system and transferred to a qubit register via local operations and classical communication (LOCC) [99].

The algorithm and proposed estimators are carefully benchmarked against exact diagonalization results for the Bose-Hubbard model. We find that relative errors of order  $10^{-4}$  can be obtained for both the kinetic and potential energies and for unconventional estimators like the Rényi entanglement entropies (both full and symmetry resolved), errors as small as  $10^{-3}$ . Extrapolation to  $\beta \rightarrow \infty$  can be performed using only a few finite  $\beta$  simulations with the largest value required for a bias-free fit scaling with system size  $L$ . While in one spatial dimension, the density matrix renormalization group (DMRG) can be used to obtain the spatial entanglement entropy in this model [100], recent work suggests that the required restriction of the local Hilbert space to a fixed number of bosons can lead to errors in the symmetry resolved entanglement that grows logarithmically in the system size for weak, but finite soft-core repulsion [41]. In two spatial dimensions, for lattice sizes up to 1024 sites at the critical point between a superfluid and insulator, we demonstrate a perimeter law, producing data that is suitable for the extraction of logarithmic corrections which can provide information on the underlying gapless excitations in the system. By exploiting relations between entanglement measures and local particle number fluctuations, we derive finite-size scaling forms for the accessible and symmetry-resolved entanglement entropies for one dimensional systems

with Gaussian local particle number distribution. These new scaling forms are then confirmed in systems of up to  $N = 64$  bosons via PIGSFLI simulations near the superfluid-insulating phase transition and for weaker interactions, deeper into the superfluid phase.

## 2.1 Projection onto the Ground State

The ground state  $|\Psi_0\rangle$  of a quantum many-body system described by Hamiltonian  $H$  can be obtained from a trial wavefunction  $|\Psi_T\rangle$  via projection in imaginary time:

$$|\Psi_0\rangle \propto \lim_{\beta \rightarrow \infty} \rho(\beta/2) |\Psi_T\rangle , \quad (2.1)$$

where  $\rho(\beta) = e^{-\beta H}$  is the imaginary time propagator and  $\beta$  is the projection length in imaginary time. Convergence is guaranteed provided  $\langle \Psi_0 | \Psi_T \rangle \neq 0$ . We expand the trial wavefunction in a complete orthonormal basis  $\{|\alpha\rangle\}$  via complex expansion coefficients  $C_\alpha \equiv \langle \alpha | \Psi_T \rangle \in \mathbb{C}$ :

$$|\Psi_T\rangle = \sum_{\alpha} C_{\alpha} |\alpha\rangle \quad (2.2)$$

chosen to partially diagonalize the Hamiltonian:

$$H = H_0 + H_1 \quad (2.3)$$

where

$$H_0 |\alpha\rangle = \varepsilon_{\alpha} |\alpha\rangle . \quad (2.4)$$

In the interaction picture,  $\rho(\beta)$  can then be expressed as:

$$\rho(\beta) = e^{-\beta H_0} T_{\tau} e^{-\int_0^{\beta} d\tau H_1(\tau)} \quad (2.5)$$

where  $T_\tau$  is the imaginary time-ordering operator and:

$$H_1(\tau) = e^{\tau H_0} H_1 e^{-\tau H_0} . \quad (2.6)$$

The propagator thus admits the expansion:

$$\rho(\beta) = e^{-\beta H_0} \left[ \mathbb{1} - \int_0^\beta d\tau H_1(\tau) + \sum_{Q=2}^{\infty} (-1)^Q \prod_{q=1}^Q \int_0^{\tau_{q+1}} d\tau_q H_1(\tau_q) \right] , \quad (2.7)$$

where  $\mathbb{1}$  is the identity operator,  $Q$  the expansion order, and imaginary times are ordered such that  $\tau_0 \equiv 0 < \tau_1 < \tau_2 < \dots < \tau_Q < \tau_{Q+1} \equiv \beta$ . Using Eq. (2.7), the matrix elements of the propagator can be written as

$$\rho(\alpha, \alpha'; \beta) = \langle \alpha' | e^{-\beta H} | \alpha \rangle = \sum_{Q=0}^{\infty} \rho^{(Q)}(\alpha, \alpha'; \beta) \quad (2.8)$$

where superscripts denote the order of the term in the expansion. The zeroth-order term reduces to:

$$\rho^{(0)}(\alpha, \alpha'; \beta) = e^{-\epsilon_{\alpha'} \beta} \langle \alpha' | \mathbb{1} | \alpha \rangle = e^{-\epsilon_{\alpha'} \beta} . \quad (2.9)$$

Similarly, the first-order term of Eq. (2.8) becomes:

$$\rho^{(1)}(\alpha, \alpha'; \beta) = - \int_0^\beta d\tau e^{-\epsilon_{\alpha'} \beta} \langle \alpha' | H_1(\tau) | \alpha \rangle = - \int_0^\beta d\tau e^{-\epsilon_{\alpha'}(\beta-\tau)} e^{-\epsilon_{\alpha} \tau} H_1^{\alpha', \alpha} \quad (2.10)$$

where we have introduced the notation  $H_1^{\alpha', \alpha} \equiv \langle \alpha' | H_1 | \alpha \rangle$  for the off-diagonal matrix element. Finally, the second and higher-order terms can be simplified by inserting appropriate resolutions of the identity:

$$\begin{aligned} \rho^{(2)}(\alpha, \alpha'; \beta) &= \int_0^\beta d\tau_2 \int_0^{\tau_2} d\tau_1 e^{-\epsilon_{\alpha'} \beta} \langle \alpha' | H_1(\tau_2) H_1(\tau_1) | \alpha \rangle \\ &= \sum_{\alpha_1} \int_0^\beta d\tau_2 \int_0^{\tau_2} d\tau_1 e^{-\epsilon_{\alpha'}(\beta-\tau_2)} e^{-\epsilon_{\alpha_1}(\tau_2-\tau_1)} e^{-\epsilon_{\alpha} \tau_1} H_1^{\alpha', \alpha_1} H_1^{\alpha_1, \alpha} . \end{aligned} \quad (2.11)$$

Examining the form of Eqs. (2.9), (2.10), and (2.11), we can write the general expansion:

$$\rho(\alpha_0, \alpha_\beta; \beta) = \sum_{Q=0}^{\infty} \sum_{\alpha_1 \dots \alpha_{Q-1}} \int d\boldsymbol{\tau}_Q (-1)^Q e^{-\epsilon_{\alpha_0} \tau_1} \prod_{q=1}^Q e^{-\epsilon_{\alpha_q} (\tau_{q+1} - \tau_q)} H_1^{\alpha_q, \alpha_{q-1}} \quad (2.12)$$

with the assignment  $\alpha_Q \equiv \alpha_\beta$  and  $\tau_{Q+1} \equiv \beta$ , and we have introduced the short-hand notation:

$$\int d\boldsymbol{\tau}_Q \equiv \int_0^{\tau_{Q+1}} d\tau_Q \int_0^{\tau_Q} d\tau_{Q-1} \dots \int_0^{\tau_2} d\tau_1. \quad (2.13)$$

In order to gain physical intuition about the form of the propagator in Eq. (2.12), we will consider a specific model of bosons on a lattice that will allow us to compute the explicit form of the matrix elements  $\epsilon_\alpha$  and  $H_1^{\alpha', \alpha}$ .

## 2.2 Bose-Hubbard Model

In this thesis, the algorithmic developments underlying PIGSFLI will be benchmarked on the Bose-Hubbard model describing the dynamics of itinerant bosons on a lattice [23]:

$$H = -t \sum_{\langle i, j \rangle} b_i^\dagger b_j + \frac{U}{2} \sum_i n_i (n_i - 1) - \mu \sum_i n_i. \quad (2.14)$$

Here,  $t$  is the tunneling between neighboring lattice sites  $\langle i, j \rangle$ ,  $U > 0$  is a repulsive interaction potential,  $\mu$  is the chemical potential, and  $b_i^\dagger (b_i)$  are bosonic creation(annihilation) operators on site  $i$ , satisfying the commutation relation:  $[b_i, b_j^\dagger] = \delta_{i, j}$ , with  $n_i = b_i^\dagger b_i$  the local number operator. Since our simulations will be performed in the canonical ensemble,  $\mu$  is a simulation parameter, that we set using the method described in Ref. [101] to improve efficiency by controlling the average number of particles to be around the target value  $N$ . Appendix A shows  $\mu$  being updated in an example simulation.



For this model, it is natural to choose  $\{|\alpha\rangle\}$  to be the Fock basis of bosonic number occupation states where

$$|\alpha\rangle = |n_0^\alpha, n_1^\alpha \dots, n_{M-1}^\alpha\rangle \quad (2.15)$$

with  $n_i^\alpha$  the number of bosons on site  $i$  for the configuration  $\alpha$  and  $M = L^D$  is the total number of  $D$ -dimensional hypercubic lattice sites. Then, the kinetic term of the Hamiltonian in Eq. (2.14) is off-diagonal, whereas the interaction and chemical potential terms constitute the diagonal part:

$$H_0 \equiv \frac{U}{2} \sum_i n_i(n_i - 1) - \mu \sum_i n_i \quad (2.16)$$

$$H_1 \equiv -t \sum_{\langle i,j \rangle} b_i^\dagger b_j . \quad (2.17)$$

Expressing  $H_0$  and  $H_1$  in the Fock basis yields explicit expressions for the matrix elements:

$$\epsilon_\alpha \equiv \langle \alpha | H_0 | \alpha \rangle = \frac{U}{2} \sum_i n_i^\alpha (n_i^\alpha - 1) - \mu \sum_i n_i^\alpha \quad (2.18)$$

$$H_1^{\alpha',\alpha} \equiv \langle \alpha' | H_1 | \alpha \rangle = -t \sum_{\langle i,j \rangle} \sqrt{n_j^\alpha (n_j^\alpha + 1)} \delta_{n_i^{\alpha'}, n_i^\alpha + 1} \delta_{n_j^{\alpha'}, n_j^\alpha - 1} \prod_{k \notin \{i,j\}} \delta_{n_k^{\alpha'}, n_k^\alpha} . \quad (2.19)$$

The structure of Eq. (2.19) ensures that only those off-diagonal elements where  $|\alpha'\rangle$  and  $|\alpha\rangle$  differ by one particle hop between different sites will be non-vanishing.

## 2.3 Configuration Space

With access to a representation of the ground state wavefunction via the projection method described in Section 2.1 we can now consider the measurement of ground

state expectation values of a physical observable  $\mathcal{O}$  in the path integral picture:

$$\begin{aligned} \langle \mathcal{O} \rangle_0 &\equiv \frac{\langle \Psi_0 | \mathcal{O} | \Psi_0 \rangle}{\langle \Psi_0 | \Psi_0 \rangle} \\ &= \frac{1}{\mathcal{Z}_0} \lim_{\beta \rightarrow \infty} \sum_{\alpha_\beta, \alpha'', \alpha', \alpha_0} C_{\alpha_\beta}^* C_{\alpha_0} \rho(\alpha'', \alpha_\beta; \beta/2) \langle \alpha'' | \mathcal{O} | \alpha' \rangle \rho(\alpha', \alpha_0; \beta/2), \end{aligned} \quad (2.20)$$

where we have used the expansion of the trial wavefunction in Eq. (2.2). The normalization  $\mathcal{Z}_0$  can be written as:

$$\mathcal{Z}_0 \equiv \langle \Psi_0 | \Psi_0 \rangle = \lim_{\beta \rightarrow \infty} \sum_{\alpha_0, \alpha_\beta} C_{\alpha_\beta}^* C_{\alpha_0} \rho(\alpha_0, \alpha_\beta; \beta) = \lim_{\beta \rightarrow \infty} \sum_{Q, \alpha_Q} \int d\tau_Q W_0(Q, \alpha_Q, \tau_Q) \quad (2.21)$$

where we have used Eq. (2.12) to express the configurational weight:

$$W_0(Q, \alpha_Q, \tau_Q) \equiv C_{\alpha_\beta}^* C_{\alpha_0} (-1)^Q e^{-\epsilon \alpha_0 \tau_1} \prod_{q=1}^Q e^{-\epsilon \alpha_q (\tau_{q+1} - \tau_q)} H_1^{\alpha_q, \alpha_{q-1}} \quad (2.22)$$

with

$$\alpha_Q \equiv \alpha_0, \alpha_1, \dots, \alpha_{Q-1}, \alpha_\beta, \quad \tau_Q \equiv \tau_1, \tau_2, \dots, \tau_Q. \quad (2.23)$$

We can interpret Eq. (2.21) as an infinite sum over all configurations of particle worldlines connecting state  $|\alpha_0\rangle$  at  $\tau = 0$  to  $|\alpha_\beta\rangle$  at  $\tau = \beta$ , via  $\rho(\alpha_0, \alpha_\beta; \beta)$ , with each configuration having statistical weight  $W_0$ . This formulation can be contrasted with the more commonly studied finite temperature picture where paths are periodic in imaginary time. The expansion order  $Q$  in Eq. (2.21) corresponds to the number of insertions of the off-diagonal operator  $H_1$  which (as discussed in Section 2.2) changes the local occupation number of a site (a particle *hop*). These hops can be diagrammatically represented as *kinks* in otherwise straight particle worldlines. Fig. 2.1 shows an example of a worldline configuration for four bosonic particles on four lattice sites.

### 2.3.1 Off-Diagonal Configurations: Worms

A major algorithmic advance in path integral Monte Carlo was attained through the extension of the diagonal configuration space described above to one that includes non-continuous paths (worms), corresponding to insertions of the single particle imaginary time Green function [57]. This technology has also been adapted to continuous space methods [89, 92] and allows for improved sampling performance, extending simulations to  $N \simeq 10^4$  particles, as well as allowing for native operation in the grand canonical ensemble. A worm is shown in red in Fig. 2.1.

Worms can be included in the configuration space through the addition of a source term in the system Hamiltonian:

$$H = H_0 + H_1 \rightarrow H_0 + H_1 + H_{\text{worm}}, \quad (2.24)$$

where

$$H_{\text{worm}} = -\eta \sum_i (b_i^\dagger + b_i), \quad (2.25)$$

with  $\eta$  the worm fugacity – a tunable parameter associated with the energetic cost of inserting or removing a worm end that can only affect the sampling efficiency. Appendix A shows  $\eta$  being updated in an example simulation.

Expectation values of physical observables are only accumulated from configurations with no worms presents, however the configurational weight in Eq. (2.22) needs to be modified:

$$W_0(Q, \boldsymbol{\alpha}_Q, \boldsymbol{\tau}_Q) = C_{\alpha_\beta}^* C_{\alpha_0} (-1)^Q e^{-\epsilon_{\alpha_0} \tau_1} \prod_{q=1}^Q e^{-\epsilon_{\alpha_q} (\tau_{q+1} - \tau_q)} (H_1^{\alpha_q, \alpha_{q-1}} + H_{\text{worm}}^{\alpha_q, \alpha_{q-1}}) \quad (2.26)$$

where the matrix elements of the source term  $H_{\text{worm}}^{\alpha', \alpha}$  can be calculated explicitly in the Fock basis:

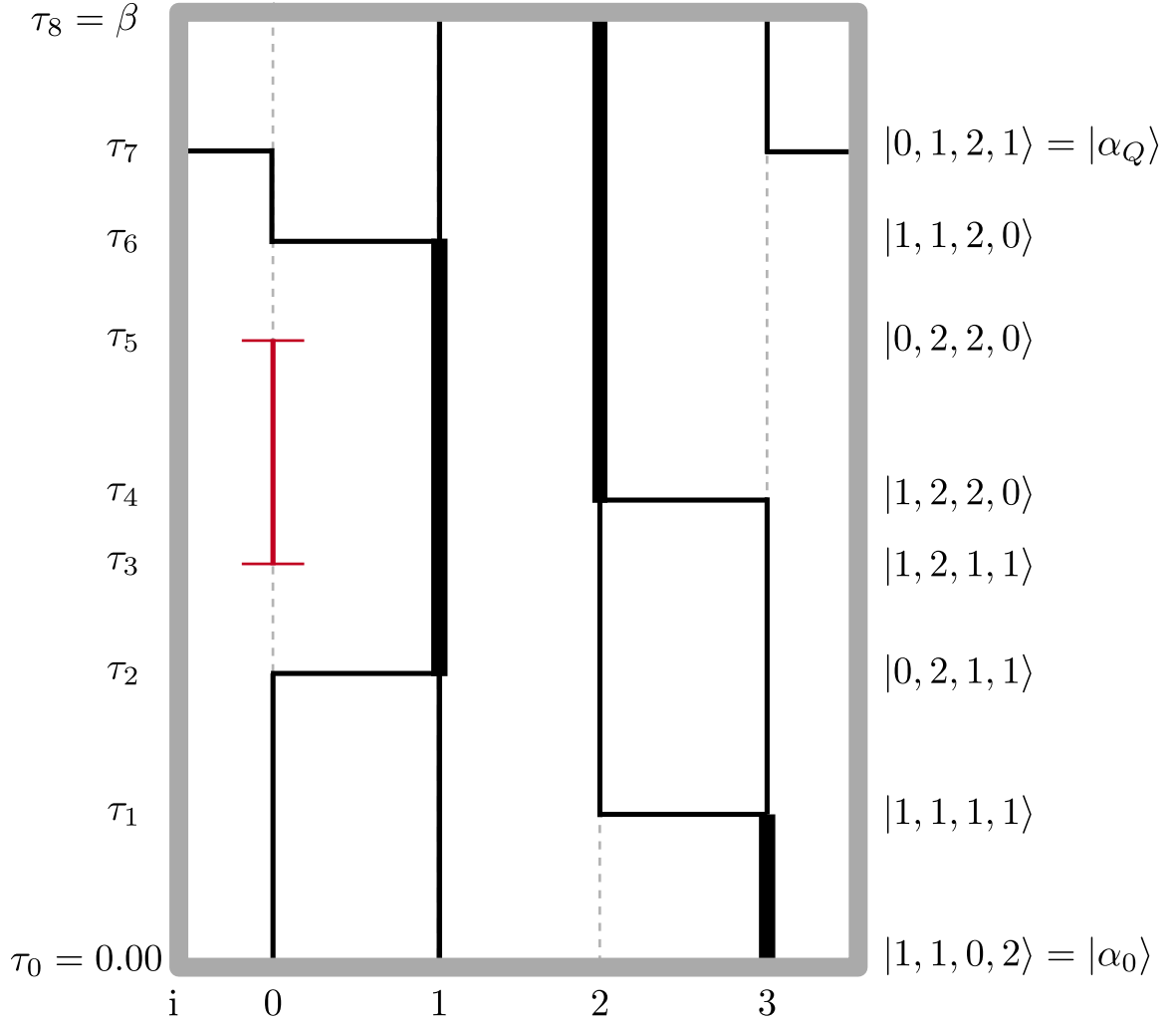


**Figure 2.1:** Example of a 4-site worldline configuration. Paths evolve in the direction of imaginary time (vertical axis) and particles can hop between sites (horizontal axis). Imaginary times at which the Fock state changes have been labeled on the left side of the diagram and the corresponding states are shown to the right. Increasing line thicknesses have been used to denote the addition of a particle to that path segment, and a vertical dashed line indicates the absence of a particle. The segment on site  $i = 0$  extending from imaginary time  $\tau_3$  to  $\tau_5$ , where a particle was spontaneously created and annihilated later, is called a worm and it will be an integral part of our algorithm. The lattice sites are subject to periodic boundary conditions, as illustrated by the particle hopping from site  $i = 3$  to  $i = 0$  at imaginary time  $\tau_7$ .

$$H_{\text{worm}}^{\alpha',\alpha} = -\eta \sum_i (\sqrt{n_i^\alpha + 1} \delta_{n_i^{\alpha'}, n_i^\alpha + 1} + \sqrt{n_i^\alpha} \delta_{n_i^{\alpha'}, n_i^\alpha - 1}) \prod_{k \neq i} \delta_{n_k^{\alpha'}, n_k^\alpha}. \quad (2.27)$$

## 2.4 Sampling

The Monte Carlo approach to estimating expectation values of observable as in Eq. (2.20) proceeds by creating a Markov chain from worldline configurations drawn according to the probability density function  $\pi(x) = W(x)/\mathcal{Z}$ , where  $x \equiv \{Q, \alpha_Q, \tau_Q\}$  such that the resulting infinite dimensional sum/integral can be recast as an importance sampling problem. The stochastic rules for transitions having probabilities  $T(x \rightarrow x')$  between configurations are independent of the history of the trajectory in state space, and  $\pi$  represents the steady state distribution. This is achieved through a set of (possibly pairs of) Monte Carlo updates satisfying detailed balance where  $\pi(x)T(x \rightarrow x') = \pi(x')T(x' \rightarrow x)$ , as well as fulfilling an ergodicity condition that all configurations are connected by a finite number of steps and there is no periodicity. We factorize the transition probability  $T(x \rightarrow x') = P(x \rightarrow x')A(x \rightarrow x')$  into the product of an a priori sampling distribution  $P(x \rightarrow x')$  and an acceptance probability  $A(x \rightarrow x')$ . Combined with detailed balance, the Metropolis-Hastings condition then leads to an expression for the acceptance ratio of a general Monte Carlo update:

$$\frac{A(x \rightarrow x')}{A(x' \rightarrow x)} = \frac{W(x')P(x' \rightarrow x)}{W(x)P(x \rightarrow x')} \equiv R \quad (2.28)$$

In [57], the original set of Worm Algorithm updates for finite temperature were introduced. For readers not familiar with them, they will be described in detail in Section 2.5. After reviewing these finite temperature updates, we introduce a new set of  $T = 0$  updates that are required due to the breaking of imaginary time translational invariance and the algorithm is then benchmarked on the 1D Bose-Hubbard model in Section 2.7

## 2.5 Original Finite Temperature Updates

In this section, we discuss the original set of worm algorithm updates. Traditionally, these are posed in terms of only one of the worm ends, either the head or the tail. For our  $T = 0$ , it will be necessary to implement all of these in order to satisfy ergodicity in the new configuration space.

### 2.5.1 Insert/Delete worm (or antiworm)

**Insert:** The insert worm update creates a finite particle worldline on a single site through the insertion of a creation operator at time  $\tau_t$  and destruction operator at  $\tau_h$  within a *flat* region of imaginary time delimited by imaginary times  $\tau_{\text{prev}}$  and  $\tau_{\text{next}}$  where the particle number does not change. A worm has a tail located at  $\tau_t$  and head at  $\tau_h$  and these times are subject to the constraint:  $\tau_h > \tau_t$ . This update is proposed only if there are no worm ends already present in the configuration.

An antiworm can instead be inserted if the sampled time of the worm head is smaller than the tail:  $\tau_h < \tau_t$ . This will first annihilate a particle and create one at a later time inside the flat region. This is only possible if there is at least one particle in the chosen flat region. Thus, if the sampled times correspond to an antiworm and there are no particles in the flat region, the update is rejected. For simplicity, we'll refer to either of these two types of path discontinuities as a worm when describing the updates. The insert worm update is illustrated in Fig. 2.2 and proceeds as follows:

0. Attempt update with probability  $p_{\text{insert}}$ . This is the bare probability of attempting this move from amongst the entire pool of updates. Every other update will have a similar bare attempt probability.
1. Randomly sample a flat region with probability  $1/N_{\text{flats}}$ , where  $N_{\text{flats}}$  is the total number of flat regions.
2. Randomly sample the worm head time  $\tau_h \in [\tau_{\text{prev}}, \tau_{\text{next}})$  with probability  $1/(\tau_{\text{next}} - \tau_{\text{prev}})$ .

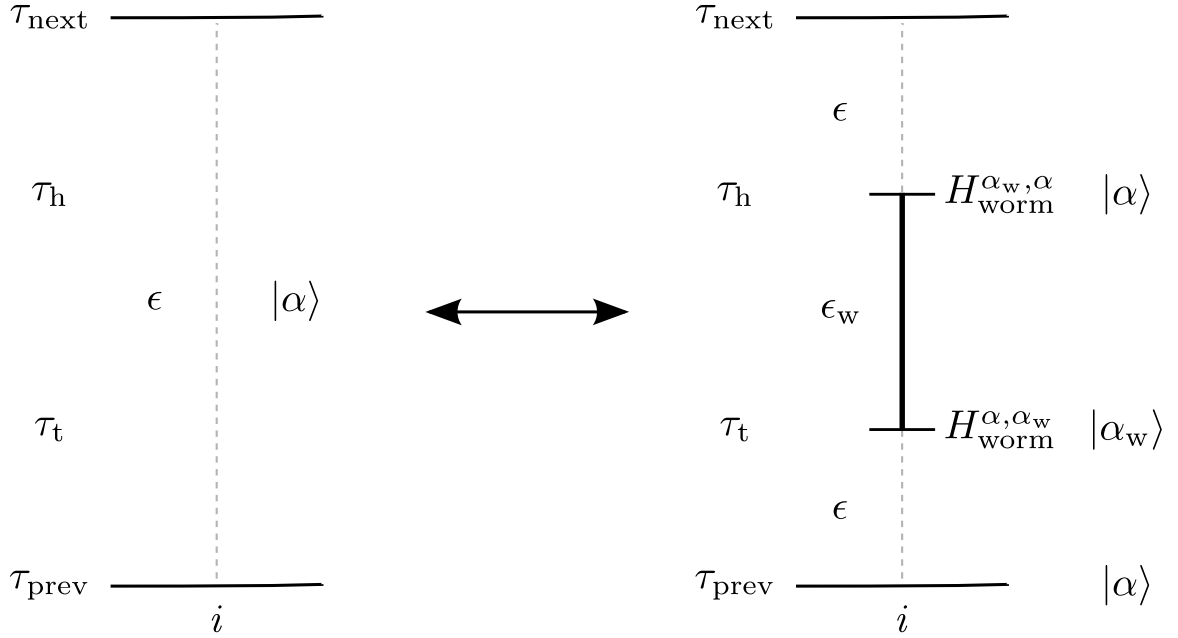


**Figure 2.2: Insert/Delete worm.** A worm is inserted by first randomly sampling imaginary times  $\tau_t, \tau_h$  inside an also randomly sampled flat interval, delimited by the times  $\tau_{prev}$  and  $\tau_{next}$ . A worm head and tail are then inserted at  $\tau_h$  and  $\tau_t$ , respectively.  $\epsilon$  and  $\epsilon_w$  correspond to the eigenvalues of the diagonal part of the Hamiltonian for Fock states  $|\alpha\rangle$  and  $|\alpha_w\rangle$ , respectively. The case of  $\tau_h < \tau_t$  is also valid and would correspond to an antiworm insertion, in which case a particle is first deleted by the worm head, then one created by the tail.

3. Randomly sample the worm tail time  $\tau_t \in [\tau_{\text{prev}}, \tau_{\text{next}})$  with probability  $1/(\tau_{\text{next}} - \tau_{\text{prev}})$ . Reject update if  $\tau_h < \tau_t$  and there are no particles in the flat interval.
4. Calculate the diagonal energy difference  $\Delta V \equiv \epsilon_w - \epsilon$ , where  $\epsilon_w$  is the diagonal energy of the segment of path inside the flat region with more particles, and  $\epsilon$  the diagonal energy in the segment with less particles.
5. Sample a random and uniformly distributed number  $r \in [0, 1)$ .
6. Check,
  - If  $r < R_{\text{insert}}$ , insert worm into worldline configuration.
  - Else, reject update and leave worldlines unchanged.

**Delete:** The complementary update of a worm insertion is a worm deletion, and it proceeds as follows:

0. Attempt update with probability  $p_{\text{delete}}$ .
1. Calculate diagonal energy difference  $\Delta V \equiv \epsilon_w - \epsilon$ .
2. Sample a random and uniformly distributed number  $r \in [0, 1)$ .
3. Check,
  - If  $r < R_{\text{delete}}$ , delete worm from worldline configuration.
  - Else, reject update and leave worldlines unchanged.

The constants  $R_{\text{insert}}$  and  $R_{\text{delete}}$  are the Metropolis acceptance ratios for the complementary pair of insert worm and delete worm updates and are computed using Eq. (2.28). Evaluating the configurational weights after and before worm insertion according to Eq. (2.26) and taking their ratio gives:

$$\frac{W_{\text{insert}}}{W_{\text{delete}}} = \eta^2 n_w e^{-(\epsilon_w - \epsilon)(\tau_h - \tau_t)}. \quad (2.29)$$



Here,  $n_w$  is the number of particles in the path segment with the extra particle (denoted by the subscript  $w$ ), or the segment after the worm tail, and  $\epsilon_w$  is the diagonal energy also in this path segment.

The proposal probabilities are obtained by multiplying all the probabilities associated with each step of the update's decision process:

$$\frac{P_{\text{delete}}}{P_{\text{insert}}} = \frac{p_{\text{delete}}}{p_{\text{insert}}} (\tau_{\text{next}} - \tau_{\text{prev}})^2 N_{\text{flats}}. \quad (2.30)$$

The total acceptance ratio for the worm insertion update thus becomes:

$$R_{\text{insert}} = \eta^2 n_w e^{-(\epsilon_w - \epsilon)(\tau_{\text{h}} - \tau_{\text{t}})} \frac{p_{\text{delete}}}{p_{\text{insert}}} (\tau_{\text{next}} - \tau_{\text{prev}})^2 N_{\text{flats}} \quad (2.31)$$

and for worm deletion, we have the reciprocal:

$$R_{\text{delete}} = \frac{1}{R_{\text{insert}}}. \quad (2.32)$$

## 2.5.2 Advance/Recede

This update can be proposed when there is at least one worm end (head/tail) present. A worm end is selected randomly, then it is moved backward or forward in the imaginary time direction. The update is illustrated in Fig. 2.3 and it proceeds as follows:

0. Randomly choose to move worm head or tail. If there is only one end, choose that one.
1. Depending on the worm end selected, sample a new worm end time  $\tau_{\text{new}} \in [\tau_{\text{prev}}, \tau_{\text{next}})$  from a truncated exponential distribution

$$p(\tau_{\text{new}}) = \begin{cases} \frac{\epsilon_w - \epsilon}{1 - e^{-(\epsilon_w - \epsilon)(\tau_{\text{next}} - \tau_{\text{prev}})}} e^{-(\epsilon_w - \epsilon)(\tau_{\text{new}} - \tau_{\text{prev}})} & \text{head} \\ \frac{\epsilon - \epsilon_w}{1 - e^{-(\epsilon - \epsilon_w)(\tau_{\text{next}} - \tau_{\text{prev}})}} e^{-(\epsilon - \epsilon_w)(\tau_{\text{new}} - \tau_{\text{prev}})} & \text{tail.} \end{cases} \quad (2.33)$$

The reason to sample the new time of the chosen worm end from a truncated exponential distributions is that the Metropolis acceptance ratio becomes unity and the update is always accepted. This is because the ratio of weights for the advance/recede update, as computed from Eq. (2.22), is either:

$$\frac{W_{\text{advance}}}{W_{\text{recede}}} = e^{-(\epsilon_w - \epsilon)(\tau_{\text{new}} - \tau_{\text{h}})} \quad (2.34)$$

for advance/recede of a worm head and:

$$\frac{W_{\text{advance}}}{W_{\text{recede}}} = e^{(\epsilon_w - \epsilon)(\tau_{\text{new}} - \tau_{\text{t}})} \quad (2.35)$$

for advance/recede of a worm tail. As for the proposal probabilities, they are computed from Eq. (2.33). Taking the ratio of the truncated exponential distribution  $p(\tau)$  between the new and old imaginary times, we obtain a complete cancellation and acceptance ratio for this update is just unity:

$$R_{\text{advance}} = R_{\text{recede}} = 1. \quad (2.36)$$

### 2.5.3 Insert/Delete kink before worm head

Worm ends can move to neighboring lattice sites by inserting a kink either before or after them. The imaginary time interval at which the kink can be inserted is delimited from above by the worm head itself and from below by the largest of the two lower bounds of the relevant flat regions on both sites. We reject all updates that would interfere with kinks on adjacent sites. The update is illustrated in Fig. 2.4, for the case of a worm head. In the figure, the matrix element corresponding to the worm end, in this case a head, is  $H_{\text{worm}}^{\alpha'_i, \alpha_i} = \langle \alpha'_i | H_{\text{worm}} | \alpha_i \rangle$ , where  $|\alpha_i\rangle$  and  $|\alpha'_i\rangle$  are the Fock states preceding and following the worm head, when it is on site  $i$  (i.e, before the kink is inserted). The matrix element  $H_{\text{worm}}^{\alpha'_j, \alpha_j} = \langle \alpha'_j | H_{\text{worm}} | \alpha_j \rangle$  is defined analogously, but for when the worm head is on site  $j$  (i.e, after the kink is inserted). The update

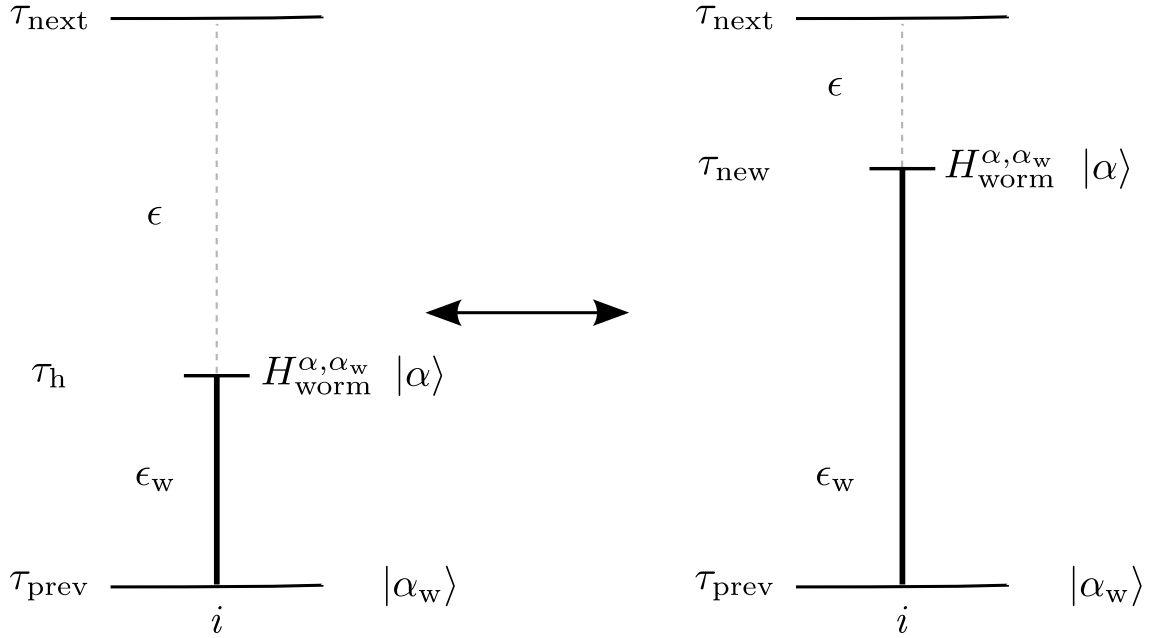


**Figure 2.3: Advance/Recede.** Worm end is selected at random. It is then moved to a randomly sampled time inside the flat interval. The diagram above illustrates the example of advancing/receding a head in imaginary time. Either the worm head or tail can be timeshifted.

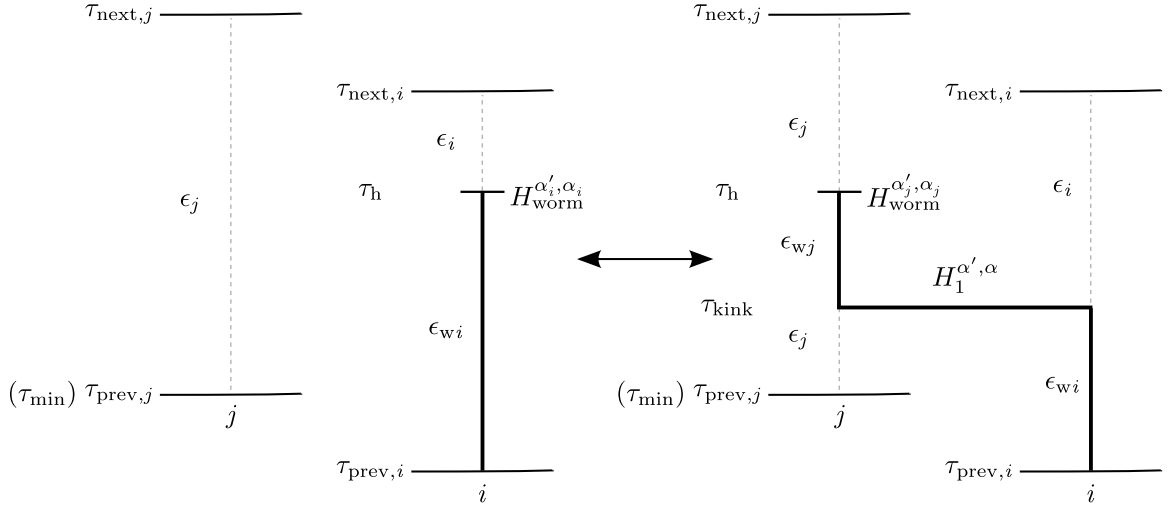


**Figure 2.4: Insert/Delete kink before head.** A kink is inserted between neighboring sites  $i, j$  before the worm head at a randomly sampled time  $\tau_{\text{kink}} \in [\tau_{\text{min}}, \tau_{\text{h}}]$  and the head moved to the site where the particle hops to. The lower bound of the sampling interval  $\tau_{\text{min}}$  is chosen to be the largest out of the two lower bounds of the corresponding flat intervals. This ensures that the new kink does not interfere with other kinks, which simplifies the implementation. The complementary update is to delete the kink and move the head back to the site from where the particle is hopping from.

proceeds as follows:

**Insert kink before head:**

0. Attempt update with probability  $p_{\text{insertKinkBeforeHead}}$ .
1. Randomly sample a nearest neighbor  $j$  of site  $i$  where the head resides with probability  $1/N_{\text{nn}}$ , where  $N_{\text{nn}}$  is the number of nearest-neighbor sites.
2. Randomly sample an imaginary time  $\tau_{\text{kink}} \in [\tau_{\text{min}}, \tau_{\text{h}})$  with probability  $1/(\tau_{\text{h}} - \tau_{\text{min}})$ .
3. Compute the diagonal energy differences  $\Delta V_i = \epsilon_{wi} - \epsilon$  and  $\Delta V_j = \epsilon_{wj} - \epsilon$ , where the  $i, j$  subscripts denote the source and destination sites of the kink.
4. Sample a random and uniformly distributed number  $r \in [0, 1)$ .
5. Check,  
If  $r < R_{\text{insertKinkBeforeHead}}$ , insert kink into worldline configuration  
Else, reject update and leave worldlines unchanged

**Delete kink before head:**

0. Attempt update with probability  $p_{\text{deleteKinkBeforeHead}}$ .
1. Compute the diagonal energy differences  $\Delta V_i = \epsilon_{wi} - \epsilon$  and  $\Delta V_j = \epsilon_{wj} - \epsilon$ .
2. Sample a random and uniformly distributed number  $r \in [0, 1)$ .
3. Check,  
If  $r < R_{\text{deleteKinkBeforeHead}}$ , delete kink from worldline configuration.  
Else, reject update and leave worldlines unchanged.

The Metropolis acceptance ratio for inserting a kink before a worm head becomes:

$$R_{\text{insertKinkBeforeHead}} = tn_{wj} e^{(\Delta V_i - \Delta V_j)(\tau_h - \tau_{\text{kink}})} \frac{p_{\text{deleteKinkBeforeHead}}}{p_{\text{insertKinkBeforeHead}}} (\tau_h - \tau_{\text{min}}) N_{\text{nn}} \quad (2.37)$$

where  $n_{wj}$  is the number of particles in the segment of site  $j$  with the extra particle.  $\tau_{\text{min}}$  is the lower bound of the sampling interval, defined such that the update does not interfere with other kinks. Out of the possible candidates for the lower bound in sites  $i, j$  it is the largest time:  $\tau_{\text{min}} = \max\{\tau_{\text{prev},i}, \tau_{\text{prev},j}\}$ . Other variations of this update, in which kinks can be inserted after a head, before a tail, and after a tail, will adapt the notational conventions introduced here. For the complementary update of deleting the kink before the head, the Metropolis acceptance ratio is just the reciprocal:

$$R_{\text{deleteKinkBeforeHead}} = \frac{1}{R_{\text{insertKinkBeforeHead}}}. \quad (2.38)$$

#### 2.5.4 Insert/Delete kink after worm head

A kink can also be inserted or deleted after the worm head. The update is illustrated in Fig. 2.5. The randomly sampled imaginary time  $\tau_{\text{kink}}$  is now in the interval  $[\tau_h, \tau_{\text{max}}]$ . The maximum time is chosen as the smallest of the upper bounds on both sites, such that the inserted kink does not interfere with other kinks:  $\tau_{\text{max}} = \min\{\tau_{\text{next},i}, \tau_{\text{next},j}\}$ . Other than the kink now being at a later imaginary time than where the head is, the procedure is analogous to inserting/deleting a kink before head. The Metropolis acceptance ratio for insertion of a kink after the head is:

$$R_{\text{insertKinkAfterHead}} = tn_{wj} e^{(-\Delta V_i + \Delta V_j)(\tau_{\text{kink}} - \tau_h)} \frac{p_{\text{deleteKinkAfterHead}}}{p_{\text{insertKinkAfterHead}}} (\tau_{\text{max}} - \tau_h) N_{\text{nn}} \quad (2.39)$$

and for deletion of a kink after the head:

$$R_{\text{deleteKinkAfterHead}} = \frac{1}{R_{\text{insertKinkAfterHead}}}. \quad (2.40)$$

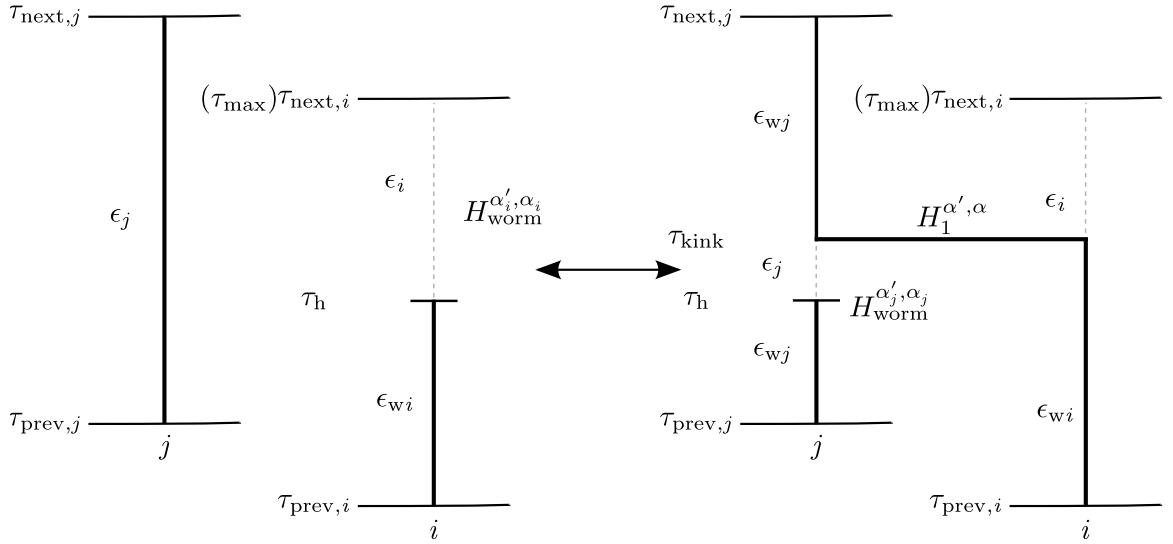


**Figure 2.5: Insert/Delete kink after head.** A kink is inserted between neighboring sites  $i, j$  after the worm head at a randomly sampled time  $\tau_{\text{kink}} \in [\tau_h, \tau_{\text{max}})$  and the head moved to the site where the particle hops to. The upper bound of the sampling interval  $\tau_{\text{max}}$  is chosen to be the smallest out of the two upper bounds of the corresponding flat intervals. This ensures that the new kink does not interfere with other kinks, which simplifies the implementation. The complementary update is to delete the kink and move the head back to the site from where the particle is hopping from.

### 2.5.5 Insert/Delete kink before worm tail

The update is illustrated in Fig. 2.6. The imaginary time of the kink is now sampled such that  $\tau_{\text{kink}} \in [\tau_{\text{min}}, \tau_{\text{t}})$ . The Metropolis acceptance ratio is:

$$R_{\text{insertKinkBeforeTail}} = tn_{\text{wj}} e^{(-\Delta V_i + \Delta V_j)(\tau_{\text{t}} - \tau_{\text{kink}})} \frac{p_{\text{insertKinkBeforeTail}}}{p_{\text{deleteKinkBeforeTail}}} (\tau_{\text{t}} - \tau_{\text{min}}) N_{\text{nn}}. \quad (2.41)$$

### 2.5.6 Insert/Delete kink after worm tail

The update is illustrated in Fig. 2.7. The imaginary time of the kink is now sampled such that  $\tau_{\text{kink}} \in [\tau_{\text{t}}, \tau_{\text{max}})$ . The Metropolis acceptance ratio is:

$$R_{\text{insertKinkAfterTail}} = tn_{\text{wj}} e^{(\Delta V_i - \Delta V_j)(\tau_{\text{kink}} - \tau_{\text{t}})} \frac{p_{\text{insertKinkAfterTail}}}{p_{\text{deleteKinkAfterTail}}} (\tau_{\text{max}} - \tau_{\text{t}}) N_{\text{nn}}. \quad (2.42)$$

The updates proposed in this section satisfy ergodicity at finite temperature. However, the set of additional updates shown in Section 2.6 are required to satisfy ergodicity at  $T = 0$ .

## 2.6 New updates for $T = 0$

At finite temperature, both the imaginary time and the spatial direction are subject to periodic boundary conditions, resulting in configurations living on the surface of a  $D + 1$  dimensional hypertorus. However, at  $T = 0$ , only the spatial directions may be periodic and configurations instead live on a cylinder of length  $\beta \rightarrow \infty$ . As such, the minimum set of updates needed to allow the random walk to visit all worldline configurations is different for  $T > 0$  and  $T = 0$  simulations. By proposing two new complementary pairs of updates, ergodicity can be satisfied for paths defined on the  $\beta$ -cylinder.



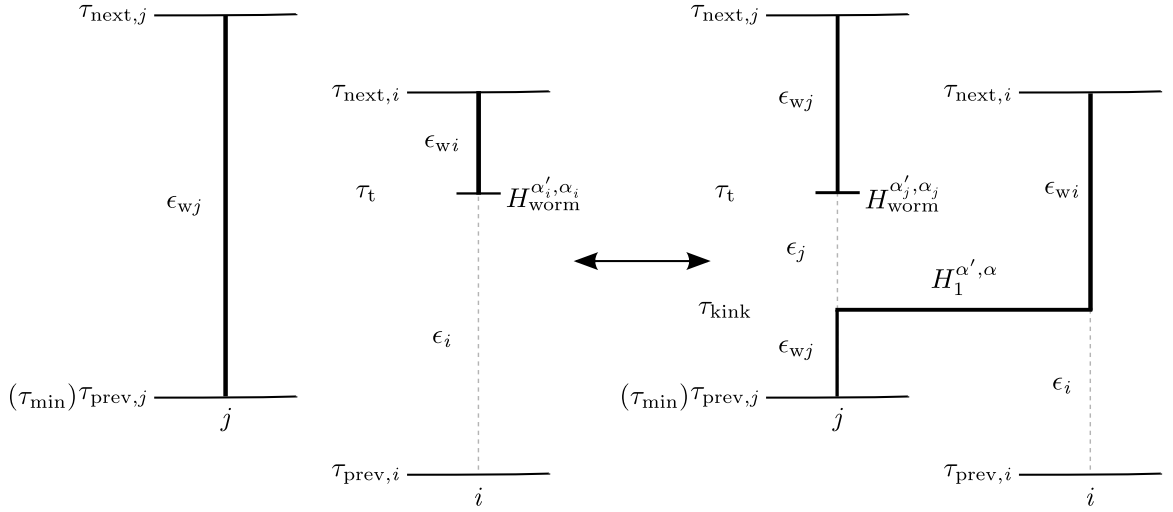


**Figure 2.6: Insert/Delete kink before tail.** A kink is inserted between neighboring sites  $i, j$  before the worm tail at a randomly sampled time  $\tau_{\text{kink}} \in [\tau_{\text{min}}, \tau_t)$  and the tail moved to the site where the particle hops from. The lower bound of the sampling interval  $\tau_{\text{min}}$  is chosen to be the largest out of the two lower bounds of the corresponding flat intervals. This ensures that the new kink does not interfere with other kinks, which simplifies the implementation. The complementary update is to delete the kink and move the tail back to the site from where the particle is hopping to.

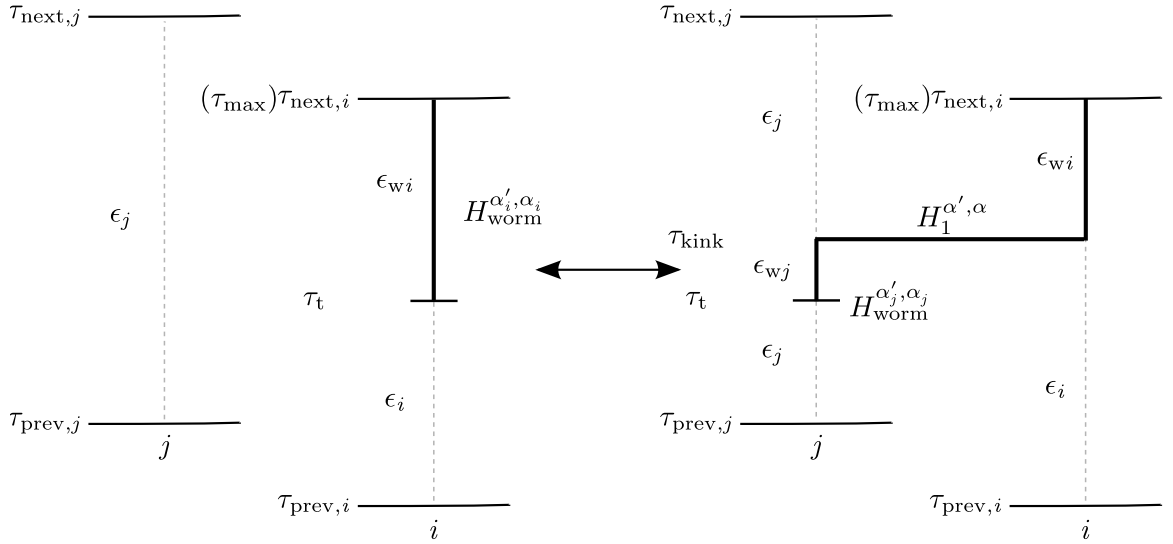


**Figure 2.7: Insert/Delete kink after tail.** A kink is inserted between neighboring sites  $i, j$  after the worm tail at a randomly sampled time  $\tau_{\text{kink}} \in [\tau_t, \tau_{\text{max}})$  and the tail moved to the site where the particle hops from. The upper bound of the sampling interval  $\tau_{\text{max}}$  is chosen to be the smallest out of the two upper bounds of the corresponding flat intervals. This ensures that the new kink does not interfere with other kinks, which simplifies the implementation. The complementary update is to delete the kink and move the tail back to the site from where the particle is hopping to.

### 2.6.1 Insert/Delete worm from $\tau = 0$

The first pair of updates required for a  $T = 0$  simulation is the insertion and deletion of a worm or antiworm that extends from  $\tau = 0$  to some time in the first flat region of the site (i.e., the flat region of the site that has lower bound  $\tau = 0$ ). To insert a worm from  $\tau = 0$ , a time is randomly sampled within the bounds of the first flat region,  $[0, \tau_{\text{next}})$ , a worm head is then inserted at the sampled time, and a particle is added to the path segment that extends from  $\tau = 0$  to the worm head. For the case of an antiworm, a worm tail is instead inserted at the randomly sampled time, then a particle destroyed from the segment preceding it. If one such worm or antiworm is present in the configuration, its deletion could also be proposed. The update is illustrated in Fig. 2.8 and proceeds as follows:

#### **Insert worm from $\tau = 0$ :**

0. Attempt update with probability  $p_{\text{insertFromZero}}$ . This is the bare probability of attempting this move from amongst the entire pool of possible updates. Every other update will have a similar bare attempt probability.
1. Randomly sample site of insertion with probability  $1/M$ , where  $M = L^D$  is the number of total sites.
2. Randomly choose to insert a worm or antiworm with probability  $p_{\text{type}}$ . If no worm ends are present, sample either worm end with probability  $p_{\text{type}} = 1/2$ . If there is one end present, select to insert the other type with probability  $p_{\text{type}} = 1$ .
3. Randomly sample insertion time  $\tau_{\text{new}}$  inside the flat region with probability  $1/\tau_{\text{next}}$ . If a worm has been chosen, then the sampled time corresponds to the time of a worm head,  $\tau_{\text{new}} = \tau_{\text{h}}$ . For an antiworm,  $\tau_{\text{new}} = \tau_{\text{t}}$  and the update is rejected if there are no particles to destroy in the flat region.

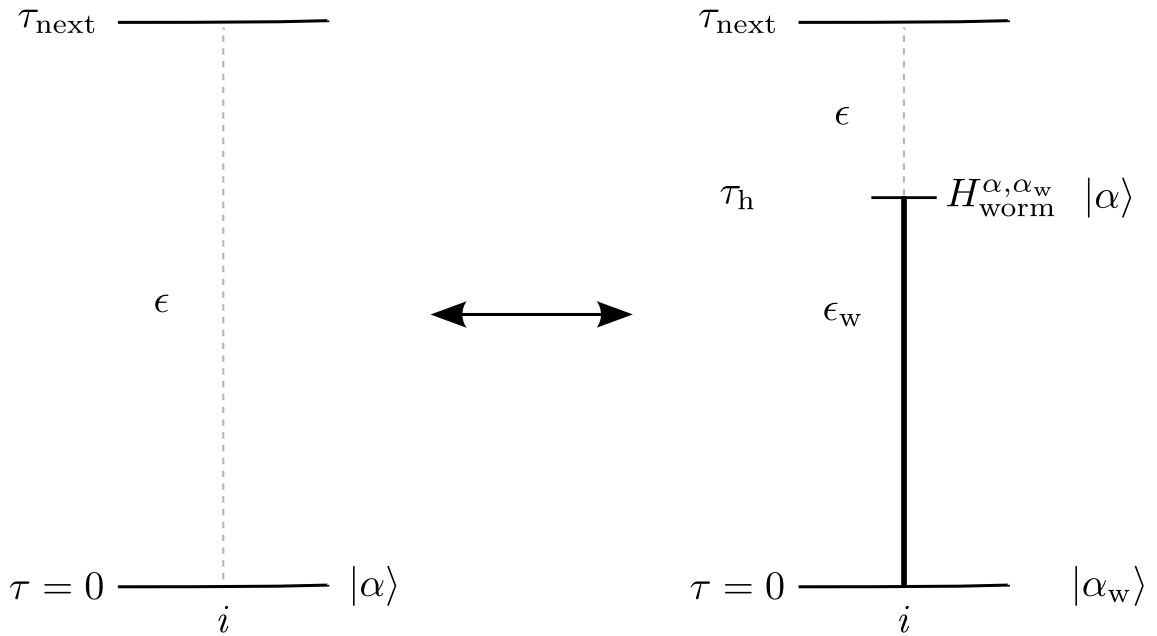


**Figure 2.8: Insert/Delete worm from  $\tau = 0$ .** A worm is inserted at the  $\tau = 0$  edge by inserting a worm head at a randomly sampled time  $\tau_h \in [0, \tau_{\text{next}})$  and adding a particle to the segment spanning the interval  $\tau : [0, \tau_h)$ . An antiworm can instead be inserted by placing a worm tail at the sampled time and destroying a particle in the segment  $\tau : [0, \tau_t)$ .

4. Calculate diagonal energy difference  $\Delta V \equiv \epsilon_w - \epsilon$ , where  $\epsilon_w$  is the diagonal energy of the segment of path inside the flat region with more particles, and  $\epsilon$  the diagonal energy in the segment with less particles.
5. Sample a random and uniformly distributed number  $r \in [0, 1)$ .
6. Check,
  - If  $r < R_{\text{insertFromZero}}$ , insert worm from  $\tau = 0$  into worldline configuration.
  - Else, reject update and leave worldlines unchanged.

**Delete worm from  $\tau = 0$ :**

0. Attempt update with probability  $p_{\text{deleteFromZero}}$ .
1. Randomly choose which of the worm ends present to delete with probability  $p_{\text{wormEnd}}$ . This can be 1/2 if there are two worm ends present and 1 if there is only one worm end.
2. Calculate diagonal energy difference  $\Delta V \equiv \epsilon_w - \epsilon$ .
3. Sample a random and uniformly distributed number  $r \in [0, 1)$ .
4. Check,
  - If  $r < R_{\text{deleteFromZero}}$ , delete worm from  $\tau = 0$  from worldline configuration.
  - Else, reject update and leave worldlines unchanged.

The acceptance ratios for the insertion from  $\tau = 0$  is:

$$R_{\text{insertFromZero}} = \begin{cases} \frac{C_{\alpha_w}}{C_\alpha} \eta \sqrt{n_w} e^{-(\epsilon_w - \epsilon) \tau_{\text{new}}} \frac{p_{\text{deleteFromZero}}}{p_{\text{insertFromZero}}} p_{\text{wormEnd}} \tau_{\text{next}} \frac{M}{p_{\text{type}}} & \text{worm} \\ \frac{C_\alpha}{C_{\alpha_w}} \eta \sqrt{n_w} e^{+(\epsilon_w - \epsilon) \tau_{\text{new}}} \frac{p_{\text{deleteFromZero}}}{p_{\text{insertFromZero}}} p_{\text{wormEnd}} \tau_{\text{next}} \frac{M}{p_{\text{type}}} & \text{anti} \end{cases} \quad (2.43)$$

and for deletion from  $\tau = 0$ :

$$R_{\text{deleteFromZero}} = \frac{1}{R_{\text{insertFromZero}}} . \quad (2.44)$$

Note the appearance of the expansion coefficients of the trial wavefunction  $C_{\alpha_w}$  and  $C_\alpha$ , with the former corresponding to the Fock State at  $\tau = 0$  with an extra particle on site  $i$ . For all simulations reported in this work, we have used a constant trial wavefunction, such that the ratio of coefficients becomes unity. The effect of changing the trial wavefunction might be an avenue for further exploration to improve convergence in imaginary time.

### 2.6.2 Insert/Delete worm from $\tau = \beta$

In analogy with insertion/deletion at  $\tau = 0$  we also need to consider the opposite end of the  $\beta$ -cylinder at  $\tau = \beta$  (i.e, the flat region bounded from above by  $\tau = \beta$ ). A worm from  $\tau = \beta$  is added by inserting a worm tail in the flat region  $[\tau_{\text{prev}}, \beta)$ , where  $\tau_{\text{prev}}$  is the time of the last kink on that site, then adding a particle to the path segment between the worm tail and the end of the flat region at  $\tau = \beta$ . For an antiworm insertion, a worm head is instead inserted, then a particle destroyed from the path segment between the head and  $\tau = \beta$ . This update is illustrated below in Fig. 2.9 and it proceeds as follows:

#### Insert worm from $\tau = \beta$ :

0. Attempt update with probability  $p_{\text{insertFromBeta}}$ .
1. Randomly sample site of insertion with probability  $1/M$ , where  $M$  is the number of total sites.
2. Randomly choose to insert a worm or antiworm with probability  $p_{\text{type}}$ . If no worm ends are present, sample either worm end with probability  $p_{\text{type}} = 1/2$ . If there's one end present, select to insert the other type with probability  $p_{\text{type}} = 1$ .

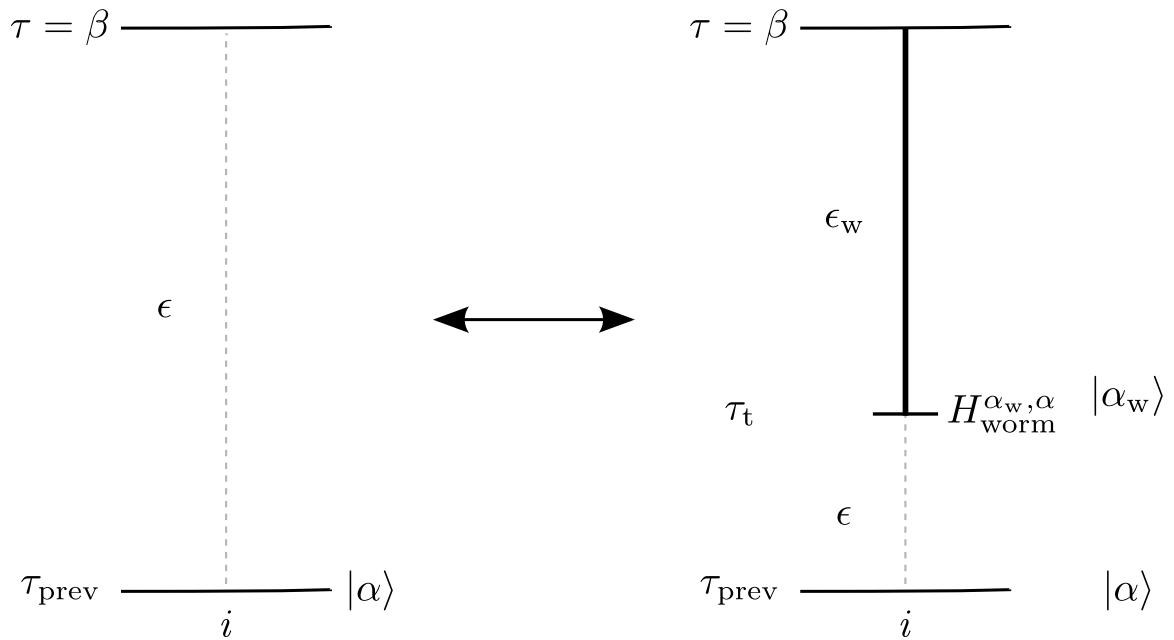


**Figure 2.9: Insert/Delete worm from  $\tau = \beta$ .** A worm is inserted at the  $\tau = \beta$  edge by inserting a worm tail at a randomly sampled time  $\tau_t \in [\tau_{\text{prev}}, \beta)$  and adding a particle to the segment spanning the interval  $\tau : [\tau_t, \beta)$ . An antiworm can instead be inserted by placing a worm head at the sampled time and destroying a particle in the segment  $\tau : [\tau_h, \beta)$ .

3. Randomly sample insertion time  $\tau_{\text{new}}$  inside the flat region with probability  $1/(\beta - \tau_{\text{prev}})$ . If a worm has been chosen, then the sampled time corresponds to the time of a worm head,  $\tau_{\text{new}} = \tau_t$ . For an antiworm,  $\tau_{\text{new}} = \tau_h$  and the update is rejected if there are no particles to destroy in the flat region.
4. Calculate diagonal energy difference  $\Delta V \equiv \epsilon_w - \epsilon$ .
5. Sample a random and uniformly distributed number  $r \in [0, 1)$ .
6. Check,
  - If  $r < R_{\text{insertFromBeta}}$ , insert worm from  $\tau = \beta$  into worldline configuration.
  - Else, reject update and leave worldlines unchanged.

**Delete worm from  $\tau = \beta$ :**

0. Attempt update with probability  $p_{\text{deleteFromBeta}}$ .
  1. Randomly choose which of the worm ends present to delete with probability  $p_{\text{wormEnd}}$ . This can be 1/2 if there are two worm ends present and 1 if there is only one worm end.
  2. Calculate diagonal energy difference  $\Delta V \equiv \epsilon_w - \epsilon$ .
  3. Sample a random and uniformly distributed number  $r \in [0, 1)$ .
  4. Check,
    - If  $r < R_{\text{deleteFromBeta}}$ , delete worm from  $\tau = \beta$  from worldline configuration.
    - Else, reject update and leave worldlines unchanged.

The acceptance ratios for the insertion/deletion from  $\tau = \beta$  update is:

$$R_{\text{insertFromBeta}} = \begin{cases} \frac{C_{\alpha_w}}{C_\alpha} \eta \sqrt{n_w} e^{-(\epsilon_w - \epsilon)(\beta - \tau_{\text{new}})} \frac{p_{\text{deleteFromBeta}}}{p_{\text{insertFromBeta}}} p_{\text{wormEnd}} (\beta - \tau_{\text{prev}}) \frac{M}{p_{\text{type}}} & \text{worm} \\ \frac{C_\alpha}{C_{\alpha_w}} \eta \sqrt{n_w} e^{+(\epsilon_w - \epsilon)(\beta - \tau_{\text{new}})} \frac{p_{\text{deleteFromBeta}}}{p_{\text{insertFromBeta}}} p_{\text{wormEnd}} (\beta - \tau_{\text{prev}}) \frac{M}{p_{\text{type}}} & \text{anti} \end{cases} \quad (2.45)$$



$$R_{\text{deleteFromBeta}} = \frac{1}{R_{\text{insertFromBeta}}} \quad (2.46)$$

The new moves described above, in combination with the original Worm Algorithm moves described for reference in Section 2.5, will allow for an ergodic PIMC simulation on the lattice at  $T = 0$ . In practice we weight all update attempt probabilities equally such that  $p_{\text{updateType}} = 1/N_{\text{updates}}$  but these could be optimized to improve simulation efficiency.

## 2.7 Energy benchmarks

To test the validity of the PIGSFLI algorithm, ground state energies have been estimated in a one dimensional Bose-Hubbard model consisting of 8 sites that is amenable to an exact solution. The ground state expectation value of the total energy:

$$\langle H \rangle_0 \simeq \langle H_0 \rangle_{\text{MC}} + \langle H_1 \rangle_{\text{MC}} \quad (2.47)$$

where the subscript MC indicates a Monte Carlo average over the weighted configuration space of worldlines. The potential energy estimator  $\langle H_0 \rangle_{\text{MC}}$  is derived in Section 2.9 and can be calculated by averaging the on-site interaction over an imaginary time window of size  $\Delta\tau$ , centered around  $\tau = \beta/2$ :

$$\langle H_0 \rangle_{\text{MC}} = \frac{1}{\Delta\tau} \left\langle \int_{\beta/2-\Delta\tau}^{\beta/2+\Delta\tau} \frac{U}{2} \sum_i n_i(\tau)(n_i(\tau) - 1) \right\rangle_{\text{MC}} \quad (2.48)$$

where the chemical potential contribution has been neglected as simulations have been performed in the canonical ensemble. The subscript MC has been added to distinguish Monte Carlo averages from usual quantum mechanical expectation values. The kinetic energy estimator is derived in Section 2.8 and is given by

$$\langle H_1 \rangle_{\text{MC}} = -\frac{\langle N_{\text{kinks}} \rangle_{\text{MC}}}{\Delta\tau} \quad (2.49)$$

where  $\langle N_{\text{kinks}} \rangle_{\text{MC}}$  is average number of kinks inside an imaginary time window of width  $\Delta\tau$ , centered around  $\tau = \beta/2$ .

Both of these estimators become stochastically exact in the limit  $\beta \rightarrow \infty$  and a suitable extrapolation procedure is described in Section 3.8. In the limit  $\beta \rightarrow \infty$ , the energy estimators are independent of the window size  $\Delta\tau$ . For finite  $\beta$  there will be additional systematic error from using a larger  $\Delta\tau$  due to lack of convergence to the ground state; decreasing  $\Delta\tau$  will generally increase the statistical errors due to a reduction in the imaginary time averaging. To balance these competing effects we set the window size to  $0.2\beta$ .

Fig. 2.10 shows the relative error between the exact and estimated ground state kinetic and potential energies, respectively, for a one-dimensional Bose-Hubbard lattice of  $L = 8$  sites at unit-filling as a function of  $\beta t$  for three different values of the on-site repulsion  $U/t = 0.5, 3.3, 10$  corresponding to the superfluid, critical point, and insulating phases. We would like to mention that the value of the quantum critical point for this system has been extensively studied throughout the years, with various methods giving slightly different estimates for it [24–39]. It is customary to report the interaction strengths in the dimensionless form  $U/t$ , which is the reason why the projection length is rescaled as  $\beta \rightarrow \beta t$ . In practice, we set the tunneling parameter to  $t = 1.0$  for all simulations and only adjust the potential  $U$  and projection length  $\beta$ . In all of these regimes, the relative error decays exponentially as a function of  $\beta$  as indicated by solid lines corresponding to the form:

$$E^{\text{err}}(\beta) = C_1 e^{-\beta t C_2} \equiv C_1 e^{-\beta C_2} \quad (2.50)$$

where  $C_1$  and  $C_2$  are fitting parameters,  $E^{\text{err}}$  denotes the relative error in either of the energies. Notice that for  $U/t = 10.0$ , the relative error in the energies becomes so small for the largest  $\beta$  values that it becomes difficult to resolve the error bars on this scale to high accuracy. This is due to the fact that in the presence of a finite energy gap, the exact ground state can be projected out from the trial wavefunction much

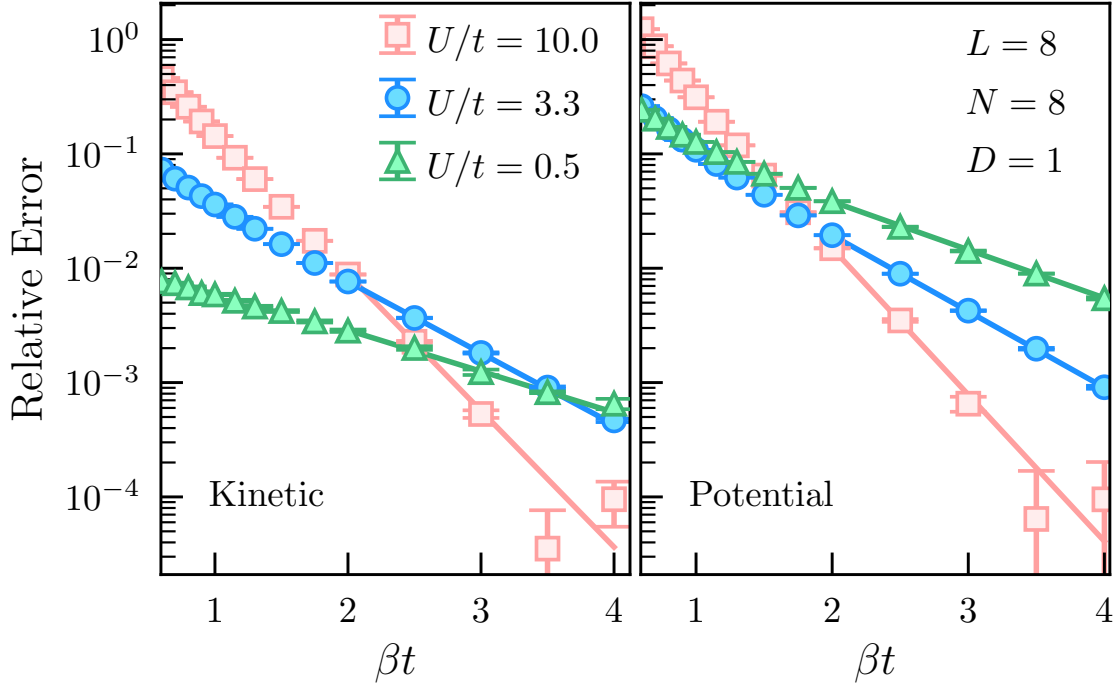


**Figure 2.10:** Relative error of the ground state kinetic energy (**left**) and potential energy (**right**) as a function of  $\beta t$  for a Bose-Hubbard chain of  $L = 8$  sites at unit-filling. As  $\beta$  increases, the relative error decays exponentially to zero, as evidenced by the fits (solid lines). Regimes where the interaction strength is large possess a sizeable energy gap and more accurate results can be obtained at lower  $\beta t$  values, since the ground state is projected out of the trial wavefunction much faster. The different shapes and colors correspond to different interaction strengths. The interaction strengths  $U/t = 0.5, 3.3, 10.0$  represent values in the superfluid phase, the 1D critical point, and the Mott phase, respectively. The measurement window is  $\Delta\tau = 0.2\beta t$ .

faster via Eq. (2.1). Conversely, near the superfluid phase, where interactions are low, the energy gap is much smaller and the error decays slowly in comparison. Formally, the superfluid phase will be gapless in the thermodynamic limit. In this regime the gap scales polynomially in the system size and thus we must increase  $\beta$  accordingly to identify the exponential behavior of observables as a function of projection length. This behavior is also expected when computing other ground state expectation values.

In the last two sections, we describe how to derive estimators for the kinetic and potential energies in a form that is amenable to computation in PIMC.

## 2.8 Kinetic Energy

In the Heisenberg representation, the kinetic energy operator, which is also just the off-diagonal term of the Bose-Hubbard Hamiltonian in Eq. (2.14), is:

$$H_1(\tau) = e^{\tau H} H_1 e^{-\tau H} \quad (2.51)$$

where  $\tau$  is an imaginary time. The ground state expectation value is, in principle, obtained in the usual way, by sandwiching  $H_1(\tau)$  in between the ground state  $|\psi_0\rangle$ :

$$\langle H_1(\tau) \rangle = \langle \psi_0 | H_1(\tau) | \psi_0 \rangle. \quad (2.52)$$

In practice, the expression above cannot be computed directly since the ground state is not exactly known. Instead, an estimator is needed that can be computed using our algorithm. Recall the projection relation:  $|\psi_0\rangle = \lim_{\beta \rightarrow \infty} e^{-\frac{\beta}{2} H} |\psi_T\rangle$ , where  $|\psi_T\rangle$  is a trial wavefunction. Substituting this projection, the expectation value becomes:

$$\langle H_1(\tau) \rangle = \lim_{\beta \rightarrow \infty} \langle \psi_T | e^{-(\frac{\beta}{2}-\tau)H} H_1 e^{-(\frac{\beta}{2}+\tau)H} | \psi_T \rangle. \quad (2.53)$$

In general, for a path-integral Monte Carlo algorithm, it is desirable to first write the estimator in terms of imaginary-time propagators. To do this, rewrite the expectation

value in terms of the trial wavefunction expansion in the Fock basis:  $|\psi_T\rangle = \sum_{\alpha} C_{\alpha} |\alpha\rangle$  and then insert some resolutions of the identity:

$$\langle H_1(\tau) \rangle = \lim_{\beta \rightarrow \infty} \sum_{\alpha_{\beta} \alpha'' \alpha' \alpha_0} \langle \psi_T | \alpha_{\beta} \rangle \langle \alpha_{\beta} | e^{-(\frac{\beta}{2} - \tau)H} | \alpha'' \rangle \langle \alpha'' | H_1 | \alpha' \rangle \langle \alpha' | e^{-(\frac{\beta}{2} + \tau)H} | \alpha_0 \rangle \langle \alpha_0 | \psi_T \rangle. \quad (2.54)$$

Rewriting the wavefunction coefficients as  $\langle \psi_T | \alpha_{\beta} \rangle = C_{\alpha_{\beta}}^*$  and  $\langle \alpha_0 | \psi_T \rangle = C_{\alpha_0}$ , the kinetic energy matrix elements as  $H_1^{\alpha'', \alpha'} = \langle \alpha'' | H_1 | \alpha' \rangle$ , and the short-time imaginary propagator between two states over an interval  $\tau$  as:  $\rho(\alpha, \alpha'; \tau) = \langle \alpha | e^{-\tau H} | \alpha' \rangle = \langle \alpha' | e^{-\tau H} | \alpha \rangle$ , the ground state expectation value of the kinetic energy becomes:

$$\langle H_1(\tau) \rangle = \lim_{\beta \rightarrow \infty} \sum_{\alpha_0 \alpha'' \alpha' \alpha_{\beta}} C_{\alpha_{\beta}}^* C_{\alpha_0} \rho(\alpha_{\beta}, \alpha''; \frac{\beta}{2} - \tau) H_1^{\alpha'' \alpha'} \rho(\alpha', \alpha_0; \frac{\beta}{2} + \tau) \quad (2.55)$$

Using Eq. (2.12), each of the propagators in the equation above can be expanded in the number of kinks inside the time interval they span (i.e,  $[\beta/2 + \tau, \beta]$  for the leftmost propagator and  $[0, \beta/2 + \tau]$  for the rightmost one).

In Eq. (2.55), the rightmost propagator will propagate the state  $\alpha_0$  from  $\tau = 0$  to state  $\alpha'$ , at  $\tau = \beta/2 + \tau$ , the time of the matrix element  $H_1^{\alpha'', \alpha'}$ . The leftmost propagator can be thought of as propagating in the direction of decreasing time, taking the state  $\alpha_{\beta}$  at  $\tau = \beta$  to state  $\alpha''$ , at  $\tau = \beta/2 + \tau$ , which is an interval of size  $\beta/2 - \tau$ . If the two states  $\alpha''$  and  $\alpha'$  differ only by a particle hop from one site to an adjacent site, the matrix element  $H_1^{\alpha'', \alpha'}$  is just a kink connecting the states, and zero otherwise, according to the kinetic matrix element in Eq. (2.19). In Eq. (2.55), take the example of expanding the leftmost and rightmost propagators up to orders

$Q_-$  and  $Q_+$ , respectively. The propagator on the right gives:

$$\begin{aligned} \rho(\alpha_\beta, \alpha''; \frac{\beta}{2} + \tau) = & \sum_{\alpha_{+1} \dots \alpha_{Q_+ - 1}} \int_0^{\tau_{Q_+ + 1} = \beta} d\tau_{Q_+} \int_0^{\tau_{Q_+}} d\tau_{Q_+ - 1} \dots \int_0^{\tau_{2_+}} d\tau_{1_+} \\ & \times \left[ (-1)^{Q_+} e^{-\epsilon_{\alpha_{0_+}} \tau_{1_+}} \prod_{q_+ = 1}^{Q_+} e^{-\epsilon_{\alpha_{q_+}} (\tau_{q_+ + 1} - \tau_{q_+})} H_1^{\alpha_{q_+}, \alpha_{q_+ - 1}} \right]. \end{aligned} \quad (2.56)$$

The propagator on the left gives:

$$\begin{aligned} \rho(\alpha', \alpha_0; \frac{\beta}{2} - \tau) = & \sum_{\alpha_{-1} \dots \alpha_{Q_- - 1}} \int_0^{\tau_{Q_- + 1} = \frac{\beta}{2} + \tau} d\tau_{Q_-} \int_0^{\tau_{Q_-}} d\tau_{Q_- - 1} \dots \int_0^{\tau_{2_-}} d\tau_{1_-} \\ & \times \left[ (-1)^{Q_-} e^{-\epsilon_{\alpha_{0_-}} \tau_{1_-}} \prod_{q_- = 1}^{Q_-} e^{-\epsilon_{\alpha_{q_-}} (\tau_{q_- + 1} - \tau_{q_-})} H_1^{\alpha_{q_-}, \alpha_{q_- - 1}} \right]. \end{aligned} \quad (2.57)$$

The subscripts  $-$ ,  $+$  can be dropped in favor of an "absolute" enumeration of the imaginary times, which will be relative to the total number of kinks  $Q$ :  $\tau_{1_+} \rightarrow \tau_1, \tau_{2_+} \rightarrow \tau_2, \dots, \tau_{Q_-} \rightarrow \tau_Q$ . Under this new enumeration, the contribution to the kinetic energy from expanding the left and right propagators to orders  $Q_-, Q_+$ , respectively, becomes:

$$\begin{aligned} \langle H_1(\tau) \rangle^{Q_- Q_+} = & \lim_{\beta \rightarrow \infty} \sum_{Q=0}^{\infty} \sum_{\alpha_0 \dots \alpha_Q} \int_0^{\tau_{Q+1} = \beta} d\tau_Q \int_0^{\tau_Q} d\tau_{Q-1} \dots \{ \quad \} \dots \int_0^{\tau_2} d\tau_1 \\ & \times \left[ C_{\alpha_\beta}^* C_{\alpha_0} (-1)^{Q-1} e^{-\epsilon_{\alpha_0} \tau_1} \prod_{q=1}^Q e^{-\epsilon_{\alpha_q} (\tau_{q+1} - \tau_q)} H_1^{\alpha_q, \alpha_{q-1}} \right] \end{aligned} \quad (2.58)$$

where the matrix elements and times associated to the states  $\alpha', \alpha''$  are now not explicitly written since they'll be contained in the product and summations over kink indices. The empty braces above are used to exaggerate the fact that, upon careful inspection, there is actually one integral missing. That is, there's only  $Q - 1$

integrals, rather than  $Q$  of them. This missing integral is due to the previously discussed propagators not having the time of the "special kink"  $H_1^{\alpha', \alpha''}$  as one of the integration variables. Instead, each of the propagators has integration variables for each of the kinks extending from  $\tau = 0$  up to but not including the special kink, and from  $\tau = \beta$  down to, but once again not including the special kink. This is also the reason for the exponent of the factor  $(-1)^{Q-1}$ .

Note also that at the moment, the time  $\tau$  has been constant. Instead, we would like to average the kinetic energy over a  $\Delta\tau$ -sized interval  $\tau : [-\Delta\tau/2, \Delta\tau/2]$ . This window-averaged kinetic energy becomes:

$$\begin{aligned} \langle H_1 \rangle^{Q-Q_+} = & -\frac{1}{\Delta\tau} \lim_{\beta \rightarrow \infty} \sum_{Q=0}^{\infty} \sum_{\alpha_0 \dots \alpha_Q} \int_0^{\tau_{Q+1}=\beta} d\tau_Q \int_0^{\tau_Q} d\tau_{Q-1} \dots \left\{ \int_{-\Delta\tau/2}^{\Delta\tau/2} d\tau \right\} \dots \\ & \times \int_0^{\tau_2} d\tau_1 \left[ C_{\alpha\beta}^* C_{\alpha_0} (-1)^Q e^{-\epsilon_{\alpha_0} \tau_1} \prod_{q=1}^Q e^{-\epsilon_{\alpha_q} (\tau_{q+1} - \tau_q)} H_1^{\alpha_q, \alpha_{q-1}} \right]. \end{aligned} \quad (2.59)$$

We can work with the absolute time of the special kink, as measured from  $\tau = 0$ , rather than  $\tau$ , the deviation from  $\beta/2$ , by performing the substitution  $\tau_{q^*} = \beta/2 + \tau$ :

$$\begin{aligned} \langle H_1 \rangle^{Q+Q_-} = & -\frac{1}{\Delta\tau} \lim_{\beta \rightarrow \infty} \sum_{Q=0}^{\infty} \sum_{\alpha_0 \dots \alpha_Q} \int_0^{\tau_{Q+1}=\beta} d\tau_Q \int_0^{\tau_Q} d\tau_{Q-1} \dots \left\{ \int_{\Delta\tau/2-\beta/2}^{\Delta\tau/2+\beta/2} d\tau_{q^*} \right\} \dots \\ & \times \int_0^{\tau_2} d\tau_1 \left[ C_{\alpha\beta}^* C_{\alpha_0} (-1)^Q e^{-\epsilon_{\alpha_0} \tau_1} \prod_{q=1}^Q e^{-\epsilon_{\alpha_q} (\tau_{q+1} - \tau_q)} H_1^{\alpha_q, \alpha_{q-1}} \right]. \end{aligned} \quad (2.60)$$

By averaging over the time of the special kink  $\tau_{q^*}$ , there are now a total of  $Q$  integrals. Moreover, notice that the kinetic energy starts to look like the configurational weight  $W_0(Q, \boldsymbol{\alpha}_Q, \boldsymbol{\tau}_Q)$  from Eq. (2.22), summed (and integrated) over all worldline configurations. The main difference is the limits of integration of the  $\tau_{q^*}$  integral. The integration limits can be rewritten as going from  $\tau_{q^*} = 0$  to  $\tau_{q^*} = \tau_{q^*+1}$  by multiplying the integrand by the box-car function, which can be defined to be zero for all values

of the special kink  $\tau_{q^*}$ , except inside the interval  $\tau_{q^*} : [\Delta\tau/2 - \beta/2, \Delta\tau/2 + \beta/2]$ , where it will be one. Formally, the box-car function can be written as:

$$B_{\Delta\tau}(\tau_{q^*}) = H(\tau_{q^*} - \Delta\tau/2 + \beta/2) - H(\tau_{q^*} - \Delta\tau/2 - \beta/2) \quad (2.61)$$

where  $H(x)$  is the Heaviside step-function. By multiplying the integrand of the  $\tau_q^*$  integral by this box-car function, the integration limits can be changed to a larger and arbitrary interval of imaginary times, while leaving the overall result unchanged. Changing the interval to  $\tau_q^* \in [0, \tau_{q+1}^*]$ :

$$\begin{aligned} \langle H_1 \rangle^{Q_+ Q_-} = & -\frac{1}{\Delta\tau} \lim_{\beta \rightarrow \infty} \sum_{Q=0}^{\infty} \sum_{\alpha_0 \dots \alpha_Q} \int_0^{\tau_{Q+1}=\beta} d\tau_Q \int_0^{\tau_Q} d\tau_{Q-1} \dots \left\{ \int_0^{\tau_{q^*+1}^*} d\tau_{q^*} B_{\Delta\tau}(\tau_{q^*}) \right\} \dots \\ & \times \int_0^{\tau_2} d\tau_1 \left[ C_{\alpha\beta}^* C_{\alpha_0} (-1)^Q e^{-\epsilon_{\alpha_0} \tau_1} \prod_{q=1}^Q e^{-\epsilon_{\alpha_q} (\tau_{q+1} - \tau_q)} H_1^{\alpha_q, \alpha_{q-1}} \right] \end{aligned} \quad (2.62)$$

where  $\tau_{q^*+1}$  denotes the time of the kink after the special kink. Eq. (2.62) is actually only the contribution to the kinetic energy coming from expanding the left propagator to order  $Q_-$  and the right one to  $Q_+$  in Eq. (2.55). There will be contributions coming from every possible combination of expansion orders of each propagator, with the result looking similar to Eq. (2.62), except with the location of the special kink being different. For example, there are three possible combinations of the propagator expansion orders that lead to  $Q = 3$  kinks, and these are  $(Q_-, Q_+) : (2, 0), (1, 1), (0, 2)$ , for which the special kink (i.e, the one that connects the two propagators) is at  $\tau_{q^*} : \tau_1, \tau_2, \tau_3$ , respectively. Thus, the total average kinetic energy can be written as:

$$\langle H_1 \rangle = -\frac{1}{\Delta\tau} \lim_{\beta \rightarrow \infty} \sum_{Q, \alpha_Q} \int d\tau_Q \left[ \sum_{q^*=1}^Q B_{\Delta\tau}(\tau_{q^*}) C_{\alpha\beta}^* C_{\alpha_0} (-1)^Q e^{-\epsilon_{\alpha_0} \tau_1} \prod_{q=1}^Q e^{-\epsilon_{\alpha_q} (\tau_{q+1} - \tau_q)} H_1^{\alpha_q, \alpha_{q-1}} \right]. \quad (2.63)$$



Recall that  $W_0(Q, \boldsymbol{\alpha}_Q, \boldsymbol{\tau}_Q) = C_{\alpha_\beta}^* C_{\alpha_0} (-1)^Q e^{-\epsilon_{\alpha_0} \tau_1} \prod_{q=1}^Q e^{-\epsilon_{\alpha_q} (\tau_{q+1} - \tau_q)} H_1^{\alpha_q, \alpha_{q-1}}$  is the weight of a ground state configuration of worldlines. In terms of these weights, the average kinetic energy is:

$$\langle H_1 \rangle = -\frac{1}{\Delta\tau} \lim_{\beta \rightarrow \infty} \sum_{Q, \boldsymbol{\alpha}_Q} \int d\boldsymbol{\tau}_Q [W_0(Q, \boldsymbol{\alpha}_Q, \boldsymbol{\tau}_Q) \sum_{q^*=1}^Q B_{\Delta\tau}(\tau_{q^*})] \quad (2.64)$$

$$= -\frac{1}{\Delta\tau} \lim_{\beta \rightarrow \infty} \sum_{Q, \boldsymbol{\alpha}_Q} \int d\boldsymbol{\tau}_Q [W_0(Q, \boldsymbol{\alpha}_Q, \boldsymbol{\tau}_Q) N_{\text{kinks}}]. \quad (2.65)$$

Recall that the box-car function  $B_{\Delta\tau}(\tau_{q^*})$  is one when the special kink is inside the time window  $\Delta\tau$ , centered around  $\beta/2$ , and zero otherwise. Thus, the summation  $\sum_{q^*=1}^Q B_{\Delta\tau}(\tau_{q^*}) \equiv N_{\text{kinks}}$  will measure how many kinks are inside the window for a worldline configuration with  $Q$  total kinks. The set of summations and integrals shown above correspond to a sum over all possible ground state configurations of worldlines. The ground state expectation value of the kinetic energy is therefore:

$$\langle H_1 \rangle_{\text{MC}} \approx -\frac{\langle N_{\text{kinks}} \rangle_{\text{MC}}}{\Delta\tau} \quad (2.66)$$

where  $\langle N_{\text{kinks}} \rangle$  is the average number of kinks inside the window. This expression for the kinetic energy can be easily computed in our path-integral Monte Carlo simulation and is exact in the limit of  $\beta \rightarrow \infty$ .

## 2.9 Potential Energy

The ground state expectation value of the potential energy can be obtained via:

$$\langle H_0(\tau) \rangle = \langle \psi_0 | H_0(\tau) | \psi_0 \rangle. \quad (2.67)$$

Rewriting the ground state in terms of the trial wavefunction and inserting various resolutions of the identity operator like it was done for the kinetic energy:

$$\langle H_0(\tau) \rangle = \lim_{\beta \rightarrow \infty} \sum_{\alpha_\beta, \alpha'', \alpha', \alpha_0} C_{\alpha_\beta}^* C_{\alpha_0} \langle \alpha_\beta | e^{-\beta/2} | \alpha'' \rangle \langle \alpha'' | H_0(\tau) | \alpha' \rangle \langle \alpha' | e^{-\beta/2} | \alpha_0 \rangle \quad (2.68)$$

where  $H_0(\tau) = e^{\tau H} H_0 e^{-\tau H}$ . Recall that  $H_0$  is also the diagonal part of the Hamiltonian, such that  $H_0 | \alpha \rangle = \epsilon_\alpha | \alpha \rangle$ , where  $\epsilon_\alpha$  is the potential energy of state  $\alpha$ , and the specific form of these matrix elements is given in Eq. (2.18). Acting with  $H_0(\tau)$  on the state  $\alpha'$ , a Kronecker-delta function is picked up, which will get rid of the  $\alpha''$  summation:

$$\langle H_0(\tau) \rangle = \lim_{\beta \rightarrow \infty} \sum_{\alpha_\beta, \alpha', \alpha_0} \epsilon_{\alpha'}(\tau) C_{\alpha_\beta}^* C_{\alpha_0} \langle \alpha_\beta | e^{-\beta/2} | \alpha' \rangle \langle \alpha' | e^{-\beta/2} | \alpha_0 \rangle. \quad (2.69)$$

Due to the convolutional property of propagators:

$$\sum_{\alpha'} \langle \alpha_\beta | e^{-\beta/2} | \alpha' \rangle \langle \alpha' | e^{-\beta/2} | \alpha_0 \rangle = \rho(\alpha_\beta, \alpha_0; \beta). \quad (2.70)$$

Using then the definition of the propagator in Eq. (2.12) and the configurational weight in Eq. (2.22), it is seen that:

$$\langle H_0(\tau) \rangle = \lim_{\beta \rightarrow \infty} \sum_{Q, \alpha_Q} \int d\tau_Q \epsilon_{\alpha'}(\tau) W_0(Q, \alpha_Q, \tau_Q) = \lim_{\beta \rightarrow \infty} \langle \epsilon_{\alpha'}(\tau) \rangle. \quad (2.71)$$

At the moment, the potential energy is only at a time  $\tau$  away from  $\beta/2$ . Averaging over a time window of size  $\Delta\tau$  centered around  $\beta/2$ , the potential energy gives:

$$\langle H_0 \rangle = \frac{1}{\Delta\tau} \lim_{\beta \rightarrow \infty} \int_{-\Delta\tau/2}^{\Delta\tau/2} d\tau \langle \epsilon_{\alpha'}(\tau) \rangle = \frac{1}{\Delta\tau} \lim_{\beta \rightarrow \infty} \int_{\beta/2 - \Delta\tau/2}^{\beta/2 + \Delta\tau/2} d\tau \langle \epsilon_{\alpha'}(\tau) \rangle. \quad (2.72)$$

where the transformation  $\tau \rightarrow \beta/2 + \tau$  was used. Therefore, the estimator for the average ground state potential energy is:

$$\langle H_0 \rangle_{\text{MC}} \approx \frac{1}{\Delta\tau} \int_{\beta/2 - \Delta\tau/2}^{\beta/2 + \Delta\tau/2} d\tau \langle \epsilon_{\alpha'}(\tau) \rangle_{\text{MC}} \quad (2.73)$$

where  $\epsilon_{\alpha'}(\tau) = \frac{U}{2} \sum_i n_i^{\alpha'}(\tau)(n_i^{\alpha'}(\tau) - 1) - \mu \sum_i n_i^{\alpha'}(\tau)$ . The operator  $n_i(\tau)$  counts the number of particles at site  $i$  and imaginary time  $\tau$ , for a Fock state  $\alpha'$ , which can be computed directly in the simulation. The potential energy estimator becomes exact in the limit  $\beta \rightarrow \infty$ .

In the next chapter, this algorithm is extended to a two-replica configuration space in which entanglement entropies can be sampled.

# Chapter 3

## Rényi entanglement entropies in lattice PIGS

With a working Path Integral Monte Carlo algorithm at  $T = 0$  at hand, we will now introduce a method to perform estimates of quantum entanglement in the Bose-Hubbard model under a spatial bipartition. This approach will allow for the investigation of the entanglement properties of much larger systems than those that can be studied with exact diagonalization and is based on extensive previous algorithmic development in quantum Monte Carlo based on the replica trick [7–9, 11, 13–16, 85, 86, 88, 102–108]. The goal is to recast the measurement of the Rényi entanglement entropy in terms of a local expectation value of an operator that can be sampled with our Monte Carlo method.

### 3.1 Entanglement Entropy

Entanglement quantifies the non-classical correlations present in a joint state of a quantum system. Its characterization requires defining a partition of the system into subsystems; here we only consider a bipartition into a spatial subregion  $A$  and its complement  $B$ , however other types of bipartitions are also interesting, including in

terms of particles (see e.g. [3, 7, 41, 43]). Given a pure state  $|\Psi\rangle$ , the reduced density matrix of the  $A$  subsystem is defined to be:

$$\rho_A = \text{Tr}_B |\Psi\rangle \langle \Psi| . \quad (3.1)$$

In general,  $\rho_A$  describes a mixed state due to entanglement between  $A$  and  $B$  which can be quantified by the Rényi entanglement entropy (EE):

$$S_\alpha(\rho_A) = \frac{1}{1-\alpha} \ln \text{Tr} \rho_A^\alpha . \quad (3.2)$$

For  $\alpha \rightarrow 1$ , the Rényi entanglement entropy reduces to the von Neumann entanglement entropy:  $S_1(\rho_A) = -\text{Tr} \rho_A \ln \rho_A$ . Despite the fact that  $S_\alpha$  as defined in Eq. (4.1) is not in the form of an expectation value of an observable, computational methods have been developed to compute Eq. (4.1) for many-body systems in Monte Carlo simulations [8]. Moreover, certain experimental many-body systems have the capability to directly experimentally measure Eq. (4.1) [96, 97].

The entanglement entropy has been studied in a wide array of quantum many-body systems [109], providing important insights into the nature of quantum correlations. In particular, for the ground states of interacting many-body systems, the scaling of the entanglement entropy with subsystem size can display universal features of phases of matter [110]. Generically, ground states display an “area-law” scaling, where the entanglement entropy grows with the size of the boundary between subregions [62, 63, 111]. For systems with gapless excitations, additional terms appear in the entanglement entropy that either scale logarithmically with the boundary, or are independent of boundary size; the dimensionless coefficients of these terms characterize universal features of such phases of matter, such as the number of Goldstone modes [66–68] or the central charge of the underlying conformal field theory [112].

## 3.2 Symmetry-resolved and accessible entanglement entropies

In physical systems which conserve particle number (such as trapped ultracold gases), the amount of entanglement that is operationally accessible using local operations and classical communications (LOCC) is limited by the superselection rule that forbids creating superpositions of different particle number [21]. For  $\alpha = 1$ , the von Neumann accessible entanglement entropy is simply a weighted average of the entanglement entropies for  $\rho_A$  projected onto a fixed subsystem particle number, known as the symmetry-resolved entanglement entropies  $S_1(\rho_{A_n})$  [98]:

$$S_1^{\text{acc}}(\rho_A) = \sum_n P_n S_1(\rho_{A_n}). \quad (3.3)$$

In Eq. (3.3)  $n$  is the number of particles in subregion  $A$ ,  $P_n$  is the probability of  $A$  having  $n$  particles  $P_n \equiv \text{Tr}(\Pi_n \rho_A \Pi_n)$ , where  $\Pi_n$  is a projector onto the subspace of  $A$  with  $n$  particles, and  $\rho_{A_n}$  is the reduced density matrix of  $A$ , projected onto fixed local particle number  $n$ :

$$\rho_{A_n} = \frac{1}{P_n} \Pi_n \rho_A \Pi_n. \quad (3.4)$$

For the Rényi entropy [22] for general  $\alpha$ , the operationally accessible entanglement is

$$S_\alpha^{\text{acc}}(\rho_A) = \frac{\alpha}{1-\alpha} \ln \left[ \sum_n P_n e^{\frac{1-\alpha}{\alpha} S_\alpha(\rho_{A_n})} \right], \quad (3.5)$$

which reduces to  $S_1^{\text{acc}}$  for  $\alpha \rightarrow 1$ .

$S_\alpha^{\text{acc}}$  represents an experimentally relevant bound on the entanglement that may be extracted from systems of indistinguishable and itinerant non-relativistic particles. The quantification of the symmetry-resolved and accessible entanglement entropies has garnered much interest recently in systems of both non-interacting and interacting particles [22, 41, 42, 78, 98, 99, 113–145]. We show in Section 3.4 that both the

symmetry resolved entanglement entropy,  $S_\alpha(\rho_{A_n})$ , and the accessible entanglement entropy,  $S_\alpha^{\text{acc}}$ , can be computed for interacting boson systems using Monte Carlo methods, opening up a number of exciting potential avenues of study.

### 3.3 Entanglement entropy estimator

We can compute the Rényi entanglement entropy in quantum Monte Carlo by performing simulations of two (or more) identical and non-interacting copies of the system. For  $\alpha = 2$ , we'll consider the system  $|\Psi\rangle$  and a replica  $|\tilde{\Psi}\rangle$ , and note that  $S_2(\rho_A)$  can be related to the expectation value of the unitary  $\text{SWAP}_A$  operator [8] that acts on the replicated Hilbert space. An example replicated worldline configuration is shown in Fig. 3.1.

Defining  $\{|a\rangle\}$  and  $\{|b\rangle\}$  to be bases of states that are localized to subregion A and its complement, respectively, the  $\text{SWAP}_A$  operator is defined on the tensor product states  $|a, b\rangle \equiv |a\rangle \otimes |b\rangle$  to exchange the states of the subsystem A between the replicas.:

$$\text{SWAP}_A \left[ |a, b\rangle \otimes |\tilde{a}, \tilde{b}\rangle \right] \equiv |\tilde{a}, b\rangle \otimes |a, \tilde{b}\rangle \quad (3.6)$$

For an arbitrary state  $|\Psi\rangle = \sum_{a,b} C_{ab} |a, b\rangle$ , the expectation value of  $\text{SWAP}_A$  takes the following form:

$$\begin{aligned} \langle \text{SWAP}_A \rangle &\equiv \langle \Psi_0 | \otimes \langle \tilde{\Psi}_0 | \text{SWAP}_A | \Psi_0 \rangle \otimes | \tilde{\Psi}_0 \rangle \\ &= \langle \Psi_0 | \otimes \langle \tilde{\Psi}_0 | \sum_{a,b} C_{ab} \sum_{\tilde{a}, \tilde{b}} C_{\tilde{a}\tilde{b}} |\tilde{a}, b\rangle \otimes |a, \tilde{b}\rangle = \sum_{a, \tilde{a}} \left( \sum_b C_{\tilde{a}b}^* C_{ab} \right) \left( \sum_{\tilde{b}} C_{a\tilde{b}}^* C_{\tilde{a}\tilde{b}} \right) \\ &= \sum_{a, \tilde{a}} \rho_A(\tilde{a}, a) \rho_A(a, \tilde{a}) = \text{Tr} \rho_A^2 \end{aligned}$$

where  $\rho_A(\tilde{a}, a) = \langle \tilde{a} | \rho_A | a \rangle$  are elements of the reduced density matrix.

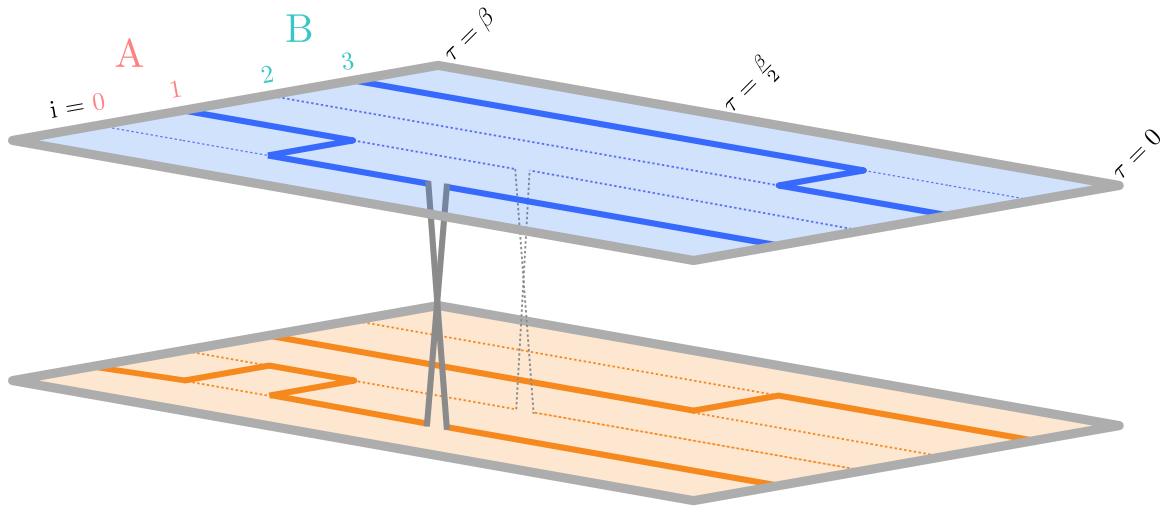


**Figure 3.1:** Example of worldlines in the two-replica space in which entanglement entropies will be measured. A special type of kink between replicas that we refer to as a SWAP kink can now be inserted or deleted at  $\tau = \beta/2$  on the sites that belong to subregion  $A$ . In this example, two SWAP kinks are shown on sites  $i = 0$  and  $i = 1$ .



The second Rényi EE can then be computed from the expectation value of  $\text{SWAP}_A$  as

$$S_2(\rho_A) = -\ln\langle\text{SWAP}_A\rangle. \quad (3.7)$$

To measure the  $\text{SWAP}_A$  estimator, two non-interacting replicas of the worldline configuration space are sampled. The sampling weight of these statistically independent sets of worldlines is the product of their weights  $W(Q, \alpha_Q, \tau_Q)\tilde{W}(\tilde{Q}, \tilde{\alpha}_Q, \tilde{\tau}_Q)$ , where the tilde vs non-tilde refers to quantities in different replicas. For the measurement of entanglement, the sampled ensemble also allows for the possibility of kinks occurring at  $\tau = \beta/2$  that connect the spatial subregion  $A$  of each of the replicas.

In the replicated configuration space, the ground state can be projected out of a trial wavefunction by generalizing the projection relation in Eq. (2.1) as:

$$|\Psi_0\rangle \otimes |\tilde{\Psi}_0\rangle = \lim_{\beta \rightarrow \infty} e^{-\frac{\beta}{2}H \otimes \mathbf{1}} |\Psi_T\rangle \otimes e^{-\frac{\beta}{2}\mathbf{1} \otimes H} |\tilde{\Psi}_T\rangle. \quad (3.8)$$

Where the operator structure reflects operation on the system (replica).

$$\begin{aligned} \langle\text{SWAP}_A\rangle &= \lim_{\beta \rightarrow \infty} \sum_{\substack{\alpha_0, \alpha_{\beta/2-} \\ \tilde{\alpha}_0, \tilde{\alpha}_{\beta/2-}}} \sum_{\substack{\alpha_{\beta/2+}, \alpha_\beta \\ \tilde{\alpha}_{\beta/2+}, \tilde{\alpha}_\beta}} C_{\alpha_\beta}^* C_{\tilde{\alpha}_\beta}^* C_{\alpha_0} C_{\tilde{\alpha}_0} \rho(\alpha_\beta, \alpha_{\beta/2+}; \beta/2) \tilde{\rho}(\tilde{\alpha}_\beta, \tilde{\alpha}_{\beta/2+}; \beta/2) \\ &\times \langle \alpha_{\beta/2+} \otimes \tilde{\alpha}_{\beta/2+} | \text{SWAP}_A | \alpha_{\beta/2-} \otimes \tilde{\alpha}_{\beta/2-} \rangle \rho(\alpha_{\beta/2-}, \alpha_0; \beta/2) \tilde{\rho}(\tilde{\alpha}_{\beta/2-}, \tilde{\alpha}_0; \beta/2), \end{aligned} \quad (3.9)$$

where  $\alpha_{\beta/2-}$  and  $\alpha_{\beta/2+}$  denote the Fock state immediately before and after  $\beta/2$ , respectively. Defining the bipartitioned Fock states  $|\alpha\rangle = |a, b\rangle$

$$\begin{aligned} &\langle \alpha_{\beta/2+} \otimes \tilde{\alpha}_{\beta/2+} | \text{SWAP}_A | \alpha_{\beta/2-} \otimes \tilde{\alpha}_{\beta/2-} \rangle \\ &= \left\langle a_{\beta/2+}, b_{\beta/2+} \otimes \tilde{a}_{\beta/2+}, \tilde{b}_{\beta/2+} \left| \tilde{a}_{\beta/2-}, b_{\beta/2-} \otimes a_{\beta/2-}, \tilde{b}_{\beta/2-} \right. \right\rangle \\ &= \delta_{a_{\beta/2+}, \tilde{a}_{\beta/2-}} \delta_{\tilde{a}_{\beta/2+}, a_{\beta/2-}}. \end{aligned} \quad (3.10)$$

Where the Kronecker-Delta functions are understood as the product of individual  $\delta$ -functions over the sites in spatial subregion  $A$ . The ground state expectation value is then given by:

$$\begin{aligned}
\langle \text{SWAP}_A \rangle &= \lim_{\beta \rightarrow \infty} \sum_{Q_-, \alpha_{Q_-}} \int d\tau_{Q_-} W_0(Q_-, \alpha_{Q_-}, \tau_{Q_-}) \sum_{Q_+, \alpha_{Q_+}} \int d\tau_{Q_+} W_0(Q_+, \alpha_{Q_+}, \tau_{Q_+}) \\
&\times \sum_{\tilde{Q}_-, \tilde{\alpha}_{\tilde{Q}_-}} \int d\tilde{\tau}_{\tilde{Q}_-} \tilde{W}_0(\tilde{Q}_-, \tilde{\alpha}_{\tilde{Q}_-}, \tilde{\tau}_{\tilde{Q}_-}) \sum_{\tilde{Q}_+, \tilde{\alpha}_{\tilde{Q}_+}} \int d\tilde{\tau}_{\tilde{Q}_+} \tilde{W}_0(\tilde{Q}_+, \tilde{\alpha}_{\tilde{Q}_+}, \tilde{\tau}_{\tilde{Q}_+}) \\
&\times \left( \delta_{a_{\beta/2+}, \tilde{a}_{\beta/2-}} \delta_{\tilde{a}_{\beta/2+}, a_{\beta/2-}} \right)
\end{aligned} \tag{3.11}$$

The expression above is in the form of a statistical average over paths of the product of  $\delta$ -functions  $\delta_{a_{\beta/2+}, \tilde{a}_{\beta/2-}} \delta_{\tilde{a}_{\beta/2+}, a_{\beta/2-}}$ , up to a normalization factor. The estimator of the expectation value of the  $\text{SWAP}_A$  operator finally becomes:

$$\langle \text{SWAP}_A \rangle_{\text{MC}} = \langle \delta_{a_{\beta/2+}, \tilde{a}_{\beta/2-}} \delta_{\tilde{a}_{\beta/2+}, a_{\beta/2-}} \rangle_{\text{MC}}. \tag{3.12}$$

In practice, this expectation value can be computed by building a histogram of the number of times each possible number of  $\text{SWAP}$  kinks was measured. This number of  $\text{SWAP}$  kinks will range from 0 to some maximum number  $m_A$ . One then takes the bin corresponding to the desired spatial partition size, and normalizes it by dividing by the bin corresponding to zero  $\text{SWAP}$  kinks measured. Histograms are only updated when both replicas have the same number of total particles.

### 3.4 Accessible and symmetry-resolved entanglement estimators

The second Rényi accessible entanglement entropy is:

$$S_2^{\text{acc}}(\rho_A) = -2 \ln \left[ \sum_n P_n e^{-\frac{1}{2} S_2(\rho_{A_n})} \right], \tag{3.13}$$

where  $\rho_{A_n}$  is the reduced density matrix of spatial partition  $A$ , projected onto the subspace of local fixed particle number  $n$ . Recall that one obtains this projected reduced density matrix via Eq. (3.4):  $\rho_{A_n} = \Pi_n \rho_A \Pi_n / P_n$ , where  $\Pi_n$  are projection operators onto the  $n$  subspace and the projected reduced density matrix is normalized by dividing by  $P_n$ , the probability of measuring a configuration with  $n$  particles in subregion  $A$ . Formally, one can define the projection operators as:

$$\Pi_n = \sum_{a^{(n)}} |a^{(n)}\rangle \langle a^{(n)}|, \quad (3.14)$$

where the summation runs over all possible configurations of the  $A$  subregion with fixed local particle number  $n$ . Recall that the reduced density matrix of subsystem  $A$  is obtained by taking the outer product of a wavefunction  $|\Psi_0\rangle$  with itself and taking the partial trace with respect to subregion  $B$ :

$$\rho_A = \sum_b \langle b | \Psi_0 \rangle \langle \Psi_0 | b \rangle, \quad (3.15)$$

where the summation is carried over the set of possible configurations in  $B$ .

The ground state of a spatially bipartitioned subsystem can be expressed as a Schmidt decomposition as:

$$|\Psi_0\rangle = \sum_{a,b} C_{ab} |a, b\rangle, \quad (3.16)$$

where the summation is carried over all configurations in  $A$  and  $B$ , and  $C_{ab}$  is the complex expansion coefficient for the bipartitioned configuration  $|a, b\rangle$ . In terms of this Schmidt decomposition, the reduced density matrix becomes:

$$\rho_A = \sum_{a,a'} \left( \sum_b C_{ab} C_{a'b}^* \right) |a\rangle \langle a'|. \quad (3.17)$$

One can now project the reduced density matrix onto the subspace of fixed local particle number  $n$  using Eq. (3.4) and Eq. (3.14):

$$\rho_{A_n} = \frac{1}{P_n} \sum_{a^{(n)}, a'^{(n)}, b^{(N-n)}} C_{a^{(n)}b^{(N-n)}} C_{a'^{(n)}b^{(N-n)}}^* |a^{(n)}\rangle \langle a'^{(n)}|. \quad (3.18)$$

Notice that the sum over  $B$  states now runs over configurations that have fixed local particle number  $N - n$ . This can be done without loss of generality since fixing the local particle number  $A$ , also fixes the local particle number in  $B$ . The matrix elements of the projected reduced density matrix can be identified as:

$$\rho_{A_n}(a^{(n)}, a'^{(n)}) \equiv \langle a^{(n)} | \rho_{A_n} | a'^{(n)} \rangle = \frac{1}{P_n} \sum_{b^{(N-n)}} C_{a^{(n)}b^{(N-n)}} C_{a'^{(n)}b^{(N-n)}}^*. \quad (3.19)$$

Now that the matrix elements have been identified, the next step is to build the replicated ground state wavefunction, akin to the one that shows up in Eq. (3.6), but for a ground state projected onto the  $n$  local particle number subspace. This can be done by first taking the Schmidt decomposition of a single replica wavefunction shown in Eq. (3.16), expanding it, and regrouping the terms that have same local particle number:

$$|\Psi_0\rangle = \sum_{a^{(0)}, b^{(N)}} C_{a^{(0)}b^{(N)}} |a^{(0)}\rangle |b^{(N)}\rangle + \sum_{a^{(1)}, b^{(N-1)}} C_{a^{(1)}b^{(N-1)}} |a^{(1)}\rangle |b^{(N-1)}\rangle + \dots \quad (3.20)$$

Then, acting with the projection operator in Eq. (3.14), only the part of the wavefunction that contributes to the  $n$ -particle sector is projected out:

$$\left| \Psi_0^{(n)} \right\rangle = \Pi_n |\Psi_0\rangle = \mathcal{N}^{-1} \sum_{a^{(n)}, b^{(N-n)}} C_{a^{(n)}b^{(N-n)}} |a^{(n)}\rangle |b^{(N-n)}\rangle \quad (3.21)$$

where  $\mathcal{N}^{-1}$  is a normalization constant, as the wavefunction may lose normalization after projection. The replicated ground state in the  $n$  subsector is represented by the tensor product of the state above and an identical copy of itself:  $\left| \Psi_0^{(n)} \right\rangle \otimes \left| \tilde{\Psi}_0^{(n)} \right\rangle$ ,

where the tilde is used to distinguish between the two replicas. Now acting with the  $\text{SWAP}_A$  operator on the replicated ground state, as was done in Eq. (3.6):

$$\text{SWAP}_A |\Psi_0^{(n)} \otimes \tilde{\Psi}_0^{(n)}\rangle = \sum_{a^{(n)}, b^{(N-n)}} \sum_{\tilde{a}^{(n)}, \tilde{a}^{(N-n)}} C_{a^{(n)}b^{(N-n)}} D_{\tilde{a}^{(n)}\tilde{b}^{(N-n)}} |\tilde{a}^{(n)}\rangle |b^{(N-n)}\rangle \otimes |a^{(n)}\rangle |\tilde{b}^{(N-n)}\rangle. \quad (3.22)$$

Taking the expectation value in the replicated projected space:

$$\begin{aligned} \langle \Psi_0^{(n)} \otimes \tilde{\Psi}_0^{(n)} | \text{SWAP}_A | \Psi_0^{(n)} \otimes \tilde{\Psi}_0^{(n)} \rangle = \\ \mathcal{N}^{-1} \sum_{a^{(n)}, \tilde{a}^{(n)}} \left( \sum_{b^{(N-n)}} C_{\tilde{a}^{(n)}b^{(N-n)}}^* C_{a^{(n)}b^{(N-n)}} \right) \left( \sum_{\tilde{b}^{(N-n)}} D_{a^{(n)}\tilde{b}^{(N-n)}}^* D_{\tilde{a}^{(n)}\tilde{b}^{(N-n)}} \right), \end{aligned} \quad (3.23)$$

where, using Eq. (3.19), the factors in parentheses can be replaced by unnormalized reduced projected density matrix elements:

$$\langle \Psi_0^{(n)} \otimes \tilde{\Psi}_0^{(n)} | \text{SWAP}_A | \Psi_0^{(n)} \otimes \tilde{\Psi}_0^{(n)} \rangle = \mathcal{N}^{-1} \sum_{\tilde{a}^{(n)}} P_n \tilde{P}_n \langle \tilde{a}^{(n)} | \rho_{A_n} \left( \sum_{a^{(n)}} |a^{(n)}\rangle \langle a^{(n)}| \right) \rho_{A_n} | \tilde{a}^{(n)} \rangle, \quad (3.24)$$

where the sum over  $a^{(n)}$  has been moved near the outer product  $|a^{(n)}\rangle \langle a^{(n)}|$  to explicitly illustrate that there is now a resolution of the identity operator present. The expectation value of the  $\text{SWAP}_A$  operator in the replicated and projected configuration space is thus:

$$\langle \text{SWAP}_{A_n} \rangle \equiv \langle \Psi_0^{(n)} \otimes \tilde{\Psi}_0^{(n)} | \text{SWAP}_A | \Psi_0^{(n)} \otimes \tilde{\Psi}_0^{(n)} \rangle = \mathcal{N}^{-1} \sum_{\tilde{a}^{(n)}} \langle \tilde{a}^{(n)} | \rho_{A_n}^2 | \tilde{a}^{(n)} \rangle, \quad (3.25)$$

where  $P_n$  and  $\tilde{P}_n$  have been absorbed into the normalization constant. Recognizing that the operation above is a trace, the expectation value can be simplified to

$$\langle \text{SWAP}_{A_n} \rangle = \mathcal{N}^{-1} \text{Tr} \rho_{A_n}^2. \quad (3.26)$$

The second Rényi entanglement entropy for local particle number  $n$  becomes (i.e, the symmetry-resolved entanglement entropy):

$$S_2(\rho_{A_n}) = -\ln [\mathcal{N}^{-1} \langle \text{SWAP}_{A_n} \rangle] . \quad (3.27)$$

Finally, substituting into Eq. (3.13), the  $\alpha = 2$  operationally accessible Rényi entanglement entropy becomes:

$$S_2^{\text{acc}}(\rho_A) = -2 \ln \left[ \sum_n P_n [\text{Tr} \rho_{A_n}^2]^{1/2} \right] = -2 \ln \left[ \sum_n P_n [\mathcal{N} \langle \text{SWAP}_{A_n} \rangle]^{1/2} \right] . \quad (3.28)$$

This expression is now amenable to estimation in the PIGSFLI algorithm.

### 3.5 Improved accessible entanglement estimator given limitations of sampling particle number sectors

In practice, the probability of measuring most local particle number sectors is small, and many of these sectors will not be visited in a given simulation. This can cause the argument of the natural logarithm in Eq. (3.28) to become vanishingly small, and the accessible entanglement estimator to be undefined. Additionally, if  $P_n$  is finite but very small, configurations with a certain number of SWAP kinks in that  $n$ -sector will not be sampled, again making Eq. (3.28) undefined.

To address this situation in practice, the summation in Eq. (3.28) can be expanded into two terms: the sum of all particle number sectors  $n$  that were measured more frequently in the simulation and have good statistics, and the contribution from  $\tilde{n}$ -sectors that were only rarely measured with poor statistics:

$$S_2^{\text{acc}}(\rho_A) \approx -2 \ln \left[ \sum_n P_n [\text{Tr} \rho_{A_n}^2]^{1/2} + \sum_{\tilde{n}} P_{\tilde{n}} [\text{Tr} \rho_{A_{\tilde{n}}}^2]^{1/2} \right] . \quad (3.29)$$

In practice, the second term can be discarded without consequence since it will be much smaller than the statistical error of the first term. Using the expansion

$$\ln(x + K) \approx \ln(K) + \frac{x}{K} - \mathcal{O}(x^2) , \quad (3.30)$$

the accessible entanglement in Eq. (3.29) can be approximated as:

$$S_2^{\text{acc}}(\rho_A) \approx -2 \left[ \ln \sum_n P_n [\text{Tr} \rho_{A_n}^2]^{1/2} + \frac{\sum_{\tilde{n}} P_{\tilde{n}} [\text{Tr} \rho_{A_{\tilde{n}}}^2]^{1/2}}{\sum_n P_n [\text{Tr} \rho_{A_n}^2]^{1/2}} \right] . \quad (3.31)$$

Since  $\text{Tr} \rho_{A_n}^2 \leq 1$  and  $P_{\tilde{n}} < 1$ , the second term is bounded from above by the sum of “bad“ (i.e., poorly measured) probabilities:

$$\sum_{\tilde{n}} P_{\tilde{n}} [\text{Tr} \rho_{A_{\tilde{n}}}^2]^{1/2} / \sum_n P_n [\text{Tr} \rho_{A_n}^2]^{1/2} < \sum_{\tilde{n}} P_{\tilde{n}} . \quad (3.32)$$

The first term of Eq. (3.31) is computed as a QMC average, with some associated statistical error  $\sigma$ . Thus the quantity  $\sum_{\tilde{n}} P_{\tilde{n}}$  can be compared to this statistical error and discarded if it is much smaller in comparison. To confirm this, a ratio between the so-called “throwaway error” and statistical error bar may be computed to confirm the relative accuracy of the procedure. For example, for the results presented in this work, the contribution to the second accessible Rényi Entropy coming from the poorly sampled  $n$ -sectors was thrown out if:  $\sum_{\tilde{n}} P_{\tilde{n}}/\sigma < 0.1$ .

In summary, the above scheme allows for the calculation of the second accessible Rényi entanglement entropy by discarding data coming from poorly sampled  $n$ -sectors that can result in undefined results.

## 3.6 Entanglement entropies via PIGSFLI

In order to measure estimators for the Rényi entanglement entropy (Eq. (3.7)), the symmetry-resolved entanglement entropy (Eq. (3.27)), and the operationally

accessible entanglement entropy (Eq. (3.28)), the simulation configuration space needs to be modified to include replicated worldlines [8] and additional updates are needed to sample the insertion of connections (SWAP kinks) between them. We will focus on the case of the  $1d$  and  $2d$  Bose-Hubbard hypercubic lattices shown in Fig. 3.2

## 3.7 SWAP Updates

### 3.7.1 Insert/Delete SWAP kink

The first pair of updates that need to be added is to insert/delete a pair of kinks, one for each replica, at  $\tau = \beta/2$  that connects worldlines between replicas. This pair of kinks can only originate/terminate from lattice sites inside subregion  $A$ . SWAP kinks are only inserted or deleted whenever the number of particles in the site at  $\tau = \beta/2$  is the same for both replicas.

The update is illustrated in Fig. 3.3 and proceeds as follows:

#### Insert SWAP kink:

0. Attempt update with probability  $p_{\text{insertSWAPKink}}$ .
1. Systemically choose a subregion site that has no kinks and get particle number on the site at  $\tau = \beta/2$  in both replicas. There is no unique way of systemically choosing the site. In 1D one can, for example, always choose to insert at site  $i + 1$  if site  $i$  already has a SWAP kink. In  $2D$ , where the subregion is also a square, one can propose insertions on a row  $i$  in the same way as the 1D case, and when full, move to the next row  $i + 1$ , then  $i + 2$ , etc ... Fig. 3.2 shows example lattices in one and two dimensions, with the subregion in which SWAP kinks will be inserted in pink.
2. Insert SWAP kink at  $\tau = \beta/2$  with unity acceptance rate if the on-site particle number at  $\tau = \beta/2$  is the same for both replicas.



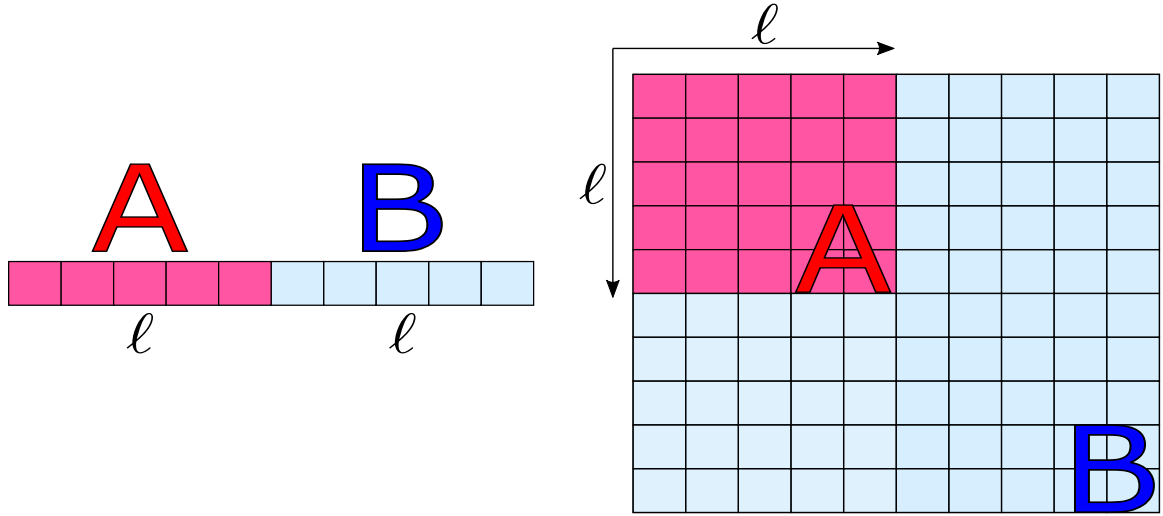


**Figure 3.2:** Example systems: (left) 1D chain under equal spatial bipartitions of size  $l$  and (right) a square lattice with square spatial subregion of linear size  $l$ . The total number of sites in the subregions is  $m \equiv l^D$ . Periodic boundary conditions are used in all cases.

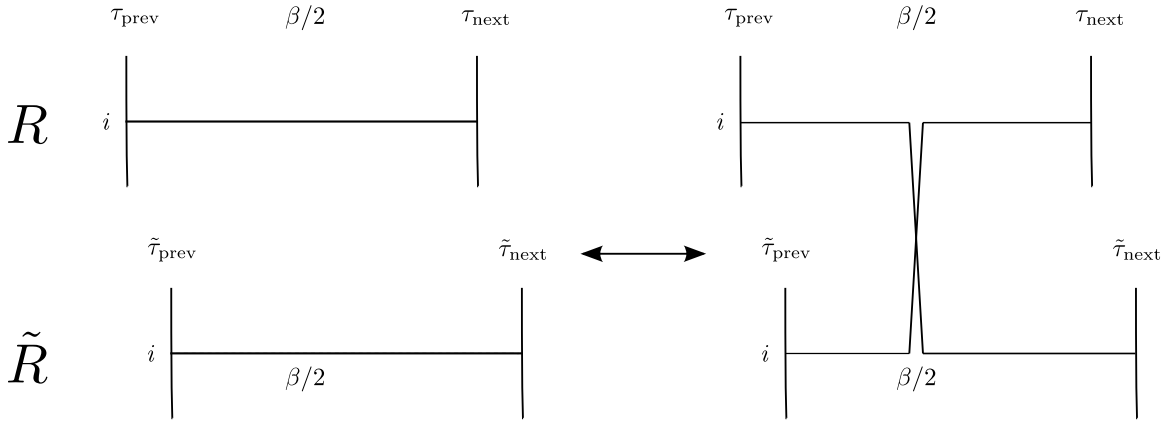


**Figure 3.3:** Insert/Delete SWAP kink. The number of particles at the center of the path,  $\tau = \beta/2$ , is measured for the same site on the two different replicas. If the number of particles is the same, then the SWAP kink is inserted. The kinks are shown to form an “X” in the diagram for visual clarity, but they both exist at exactly  $\beta/2$ . Kink deletion occurs if the number of particles at  $\beta/2$  is the same for site  $i$  of both system and replica. In the figure, the replicas are labeled  $R$  and  $\tilde{R}$ .

### Delete SWAP kink:

0. Attempt update with probability  $p_{\text{deleteSWAPKink}}$ .
1. Choose site at which last SWAP kink was inserted and get particle number on the site at  $\tau = \beta/2$  in both replicas.
2. Delete SWAP kink at  $\tau = \beta/2$  with unity acceptance rate if the on-site particle number at  $\tau = \beta/2$  is the same for both replicas.

The reason that the acceptance rate is unity for these updates is due to the restriction that local particle number be the same on both replicas at the SWAP kink insertion/deletion site. Since the number of particles will be unchanged at any path segment, there is no energetic difference for configurations post and pre update and the ratio of configurational weights post and pre update is one:  $W'/W = 1$ . The probability ratio of proposing a SWAP deletion to SWAP insertion also is unity:  $P(x' \rightarrow x)/P(x \rightarrow x') = 1$ . This is due to the systematic way in which the insertion and deletion sites are chosen. Taking the product of both ratios, then the Metropolis acceptance ratio is also unity:  $R = 1$ .

### 3.7.2 Advance/Recede along SWAP kink

This update can be seen in Fig. 3.4 and is a direct generalization of the advance/recede move of the original Worm Algorithm updates (see Section 2.5.2) to the case where a worm end is moved across a SWAP kink connecting the system and replica. Thus, the upper and lower imaginary time bounds of the flat interval will now be in different replicas. And in the same way as its single-replica counterpart, the new time of the worm end ( $\tau_{\text{new}}$ ) is sampled from the truncated exponential distribution in Eq. (2.33) to yield an acceptance ratio of unity.

The PIGSFLI algorithm has been now fully described. In the next section, entanglement entropy, symmetry resolved entanglement entropy and operationally accessible entanglement results obtained with the algorithm are presented.

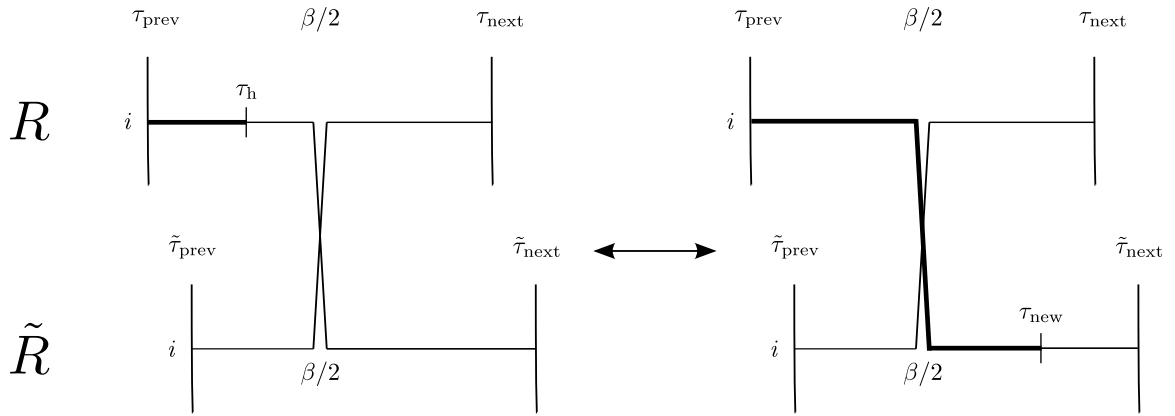


**Figure 3.4:** Advance/Recede along SWAP kink. If a worm end, either head or tail is adjacent to a SWAP kink, it can be shifted in the imaginary time direction and moved to the other replica if the new randomly sampled time goes across  $\beta/2$ . The diagram above shows the example of advancing/receding a worm head, at time  $\tau_{\text{h}}$ , along a SWAP kink and moved to the other replica to a new time,  $\tau_{\text{new}}$ .

## 3.8 Large Imaginary Time Projection of Entanglement

Since the time of a simulation scales proportionally with  $L^D\beta$ , performing measurements with sufficiently small systematic error will become difficult for large systems. To bypass this and still have a good estimate of the measurement, a three-parameter exponential fit in  $\beta$  can be performed, from which the large  $\beta$  result can be extrapolated. For the case of the second Rényi Entropy, this fit looks like:

$$S_2(\beta) = S_2^{(\beta \rightarrow \infty)} + C_1 e^{-C_2\beta} \quad (3.33)$$

where  $C_1, C_2$ , and  $S_2^{(\beta \rightarrow \infty)}$  are fitting parameters. The parameter  $S_2^{(\beta \rightarrow \infty)}$  is the extrapolation of the entanglement entropy in the asymptotic limit of  $\beta$ . Fig. 3.5 illustrates the three-parameter exponential fit to  $S_2$  data obtained from the PIGS simulation. Various interaction strengths  $U/t$  are chosen for this benchmark and the fit works well for all. For each of the interactions, extracting  $S_2^{(\beta \rightarrow \infty)}$  from the fits gives estimates for the entanglement entropy that are always within one standard deviation of the exact value, computed with exact diagonalization.

## 3.9 Results

Previous numerical studies of entanglement in the Bose-Hubbard model have mostly focused on small system sizes using exact diagonalization [41, 99, 146, 147] or matrix product based methods [24, 148–151] which enforce an occupation restriction on the local Hilbert space for soft-core bosons. Results in two spatial dimensions exist [69, 152, 153], but they are more scarce, especially for the symmetry resolved and accessible entanglements.

We begin by benchmarking the capability of the PIGSFLI algorithm for entanglement quantification. The relative error of the second Rényi entanglement entropy for

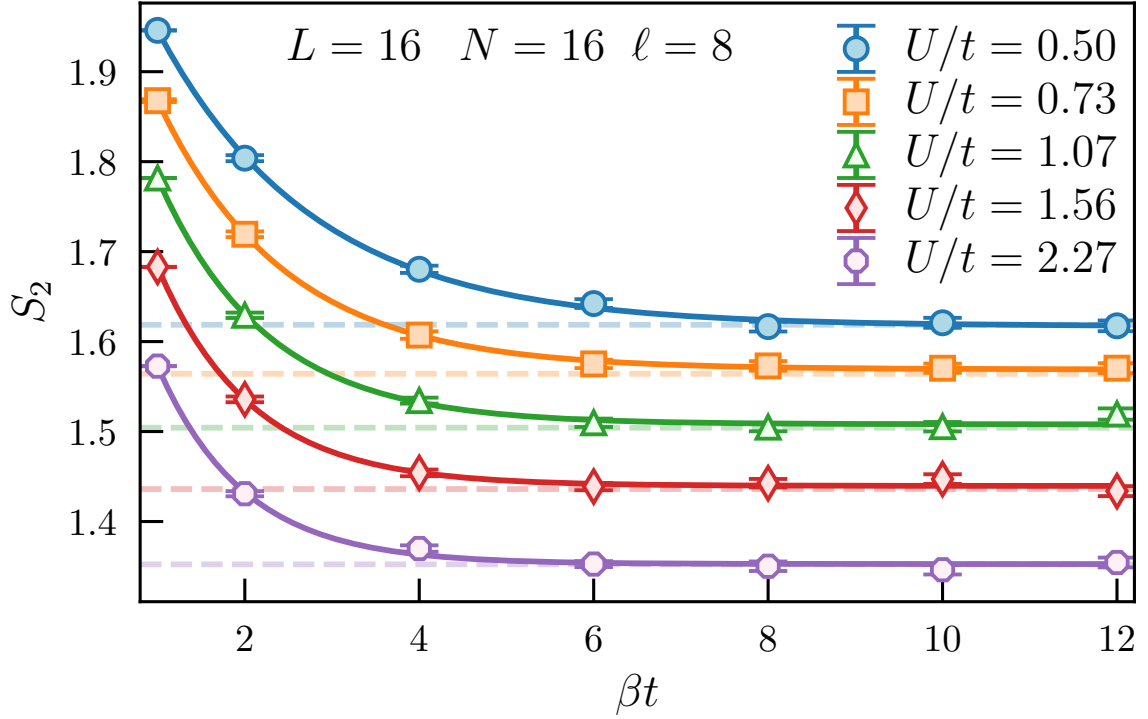


**Figure 3.5:** Full second Rényi Entropy for a one-dimensional lattice of  $L = 16$  sites at unit-filling under an equal spatial bipartition of size  $\ell = 8$ . Three-parameter exponential fits in  $\beta t$  (solid lines) have been performed on the Monte Carlo results (markers). The dashed horizontal lines denote exact diagonalization values for each of the various interaction strengths. The three-parameter exponential fits the data well and can be used to extrapolate the large  $\beta$  limit results of measurements of interest.

a small system of  $L = M = 8$  in one dimension as a function of the projection length  $\beta$  is shown in Fig. 3.6 for a maximal spatial bipartition with  $\ell = L/2 = 4$ . Here, the error is calculated using the exact result via a ground state diagonalization of the full Hamiltonian. The Monte Carlo estimates have been obtained by averaging over many seeds and using the jackknife method for error bar estimation.

We report results for interaction strengths  $U/t = 0.5, 3.3, 10.0$ , characteristic of the superfluid phase, the critical point, and Mott insulating phases, respectively. Due to the small energy gap in the superfluid phase, it is seen that the exact result is projected out via QMC at a much slower rate when increasing  $\beta$  than compared to regimes where the energy gap is large. However, for all three interaction strengths considered, good accuracy is achieved, with  $< 1\%$  relative error.

Moving to larger system sizes, and verifying how entanglement changes at quantum phase transitions, we show the second Rényi entropy in Fig. 3.7 across the phase diagram. The left panel displays results for a 1D Bose-Hubbard chain of  $L = 16$  sites at unit-filling, under an equal spatial bipartition composed of  $\ell = 8$  sites. For this 16 particle system, exact diagonalization can still be employed, and the exact result is included as a solid line. QMC results are obtained for a range of projection lengths  $\beta$  at each interaction strength. At small interactions  $U/t \ll 1$ , deep in the superfluid phase, and up to a value of  $U/t \approx 10$ , the systematic error falls as  $\beta$  increases. Deeper in the insulating phase, even though in principle this exponential decay of the systematic error is still happening, all data points are seen to collapse onto the exact result on this scale. This is again due to the finite energy gap causing the exact ground state expectation values to be projected out much faster (i.e., for smaller  $\beta$ ) from the trial (constant) wavefunction. Improved projection behavior could be obtained by tuning the trial state as a function of  $U/t$ .

The  $\beta \rightarrow \infty$  asymptotic value of  $S_2$  can be systematically obtained by performing a three-parameter exponential fit of QMC data to the form:

$$S_2(\beta) = S_2^{(\beta \rightarrow \infty)} + C_1 e^{-C_2 \beta} , \quad (3.34)$$

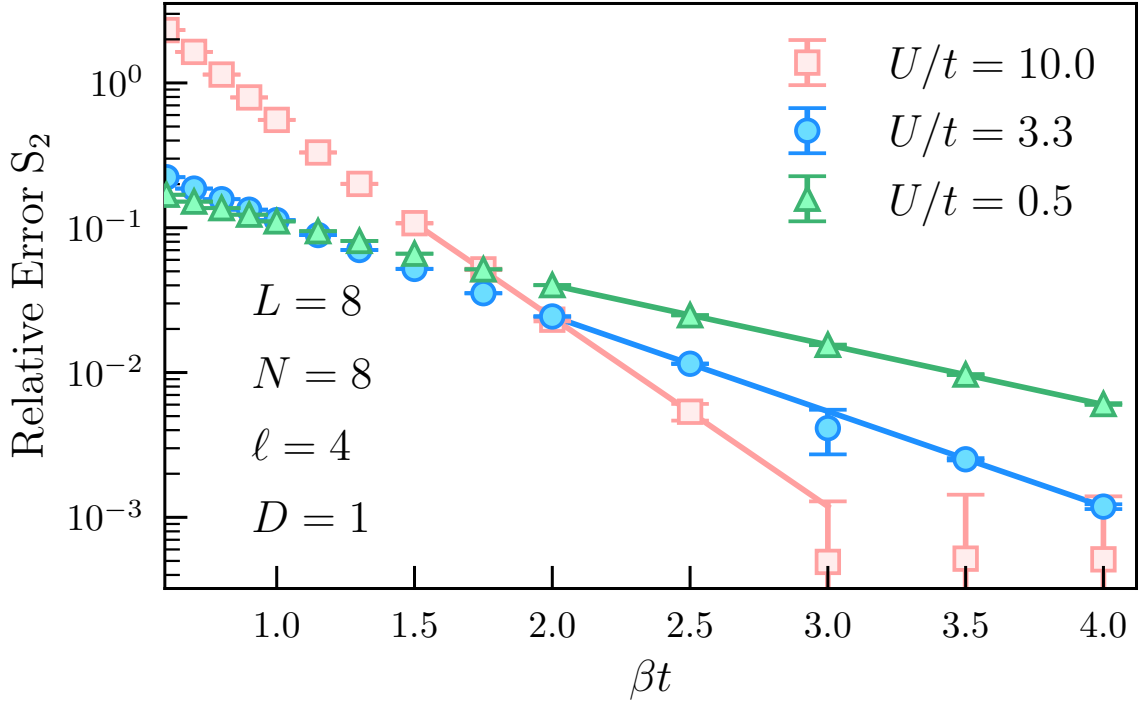


**Figure 3.6:**  $\beta$ -scaling of relative error of full entanglement  $S_2$  for a 1D lattice of  $L = 8$  sites at unit-filling. The system is bipartitioned into equally sized subregions  $A, B$  of size  $\ell = 4$  sites. The relative error of  $S_2$  decays as a function of  $\beta t$ . The solid lines are simple exponential fits.

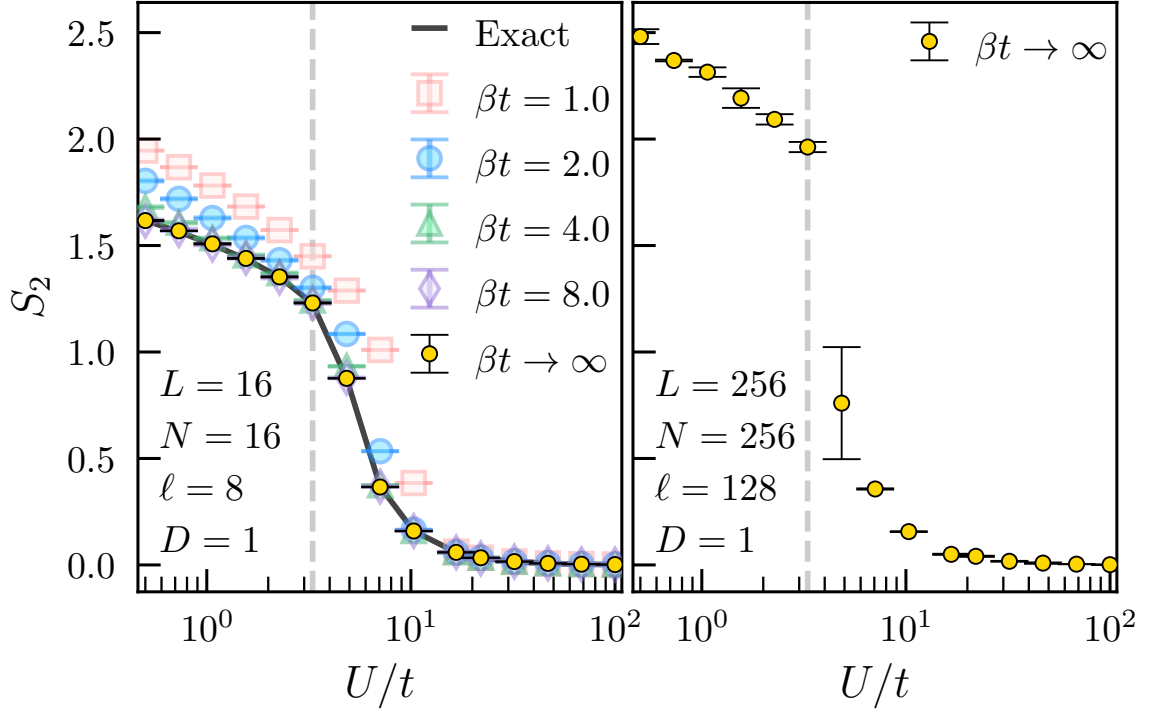


**Figure 3.7:** (left) Full Rényi Entanglement Entropy  $S_2$  for a 1D Bose-Hubbard lattice with  $L = 16$  sites at unit-filling under an equal spatial bipartition of size  $\ell = 8$  at various interaction strengths  $U$ . The entropies were measured from simulations at four different values of  $\beta t$ . As expected, the exact ground state value (solid black line) is approached as  $\beta t$  increases. The vertical dashed line at  $U = 3.3$  is the exact value of the 1D Superfluid-Mott Insulator phase transition. The solid circles are large  $\beta t$  extrapolations of  $S_2$  obtained from a three-parameter exponential fit of  $S_2$  results at  $\beta t = 4, 6, 8, 10, 12$ . (right) Full Rényi Entanglement Entropy  $S_2$  for a 1D Bose-Hubbard lattice with  $L = 256$  sites at unit-filling under an equal spatial bipartition of size  $\ell = 128$  at various interaction strengths  $U/t$ .



where  $S_2^{(\beta \rightarrow \infty)}$ ,  $C_1$ , and  $C_2$  are fitting parameters. The extrapolated second Rényi entanglement entropies are shown as solid circles. All extrapolations were observed to fall within one standard deviation of the exact result, and the range of  $\beta$  needed to access this exponential scaling regime is dependent both on interaction strength and system size.

The right panel of Fig. 3.7 shows the same interaction sweep, but for a 1D Bose-Hubbard ring of  $L = 256$  lattice sites at unit-filling under an equal spatial bipartition of  $\ell = 128$  sites. Here we only include results extrapolated to  $\beta \rightarrow \infty$ . For this larger system size, the phase transition is more clearly seen near its thermodynamic limit value  $(U/t)_c \approx 3.3$  [24–39] via an accompanying reduction in the spatial entanglement as signature of the adjacent insulating phase for strong repulsive interactions. In this regime, due to unit-filling, the ground state approaches a product state with one localized boson per site; thus the entanglement vanishes as  $U/t \rightarrow \infty$ . The behavior of  $S_2$  across the transition sweep is similar to what was seen in Ref. [18] for  $^{87}\text{Rb}$  atoms on a  $L = 4$  site lattice. Access to larger systems sizes opens the window for an accurate determination of the quantum critical point via a finite size scaling analysis using the second Rényi entropy, as it was done in Ref. [38] using a measurement based on the von Neumann entropy.

One of the main benefits of our QMC approach is that it can be easily adapted to general spatial dimension  $D$ , with spatial connections (e.g. hopping or interactions) in the Hamiltonian being encoded through an adjacency matrix. In Fig. 3.8, we show the scaling of the  $\alpha = 2$  Rényi entanglement entropy for the two dimensional Bose-Hubbard model with linear size  $L = 32$ , corresponding to  $M = 32 \times 32 = 1024$  total sites at unit-filling. Using the extrapolation method discussed above (and in Section 3.8),  $S_2$  was determined a function of  $\ell$ , the linear size of a square subregion. QMC calculations were performed at a single value of the interaction,  $U/t \approx 16.7$ , near the  $2D$  critical point [27, 154, 155]. Subregions with linear sizes  $\ell = 1, \dots, 20$  were investigated, and we observe the scaling  $S_2 \sim \ell$  as expected due to the presence of an entanglement area law [10, 62–64]. We fit the entanglement to the general

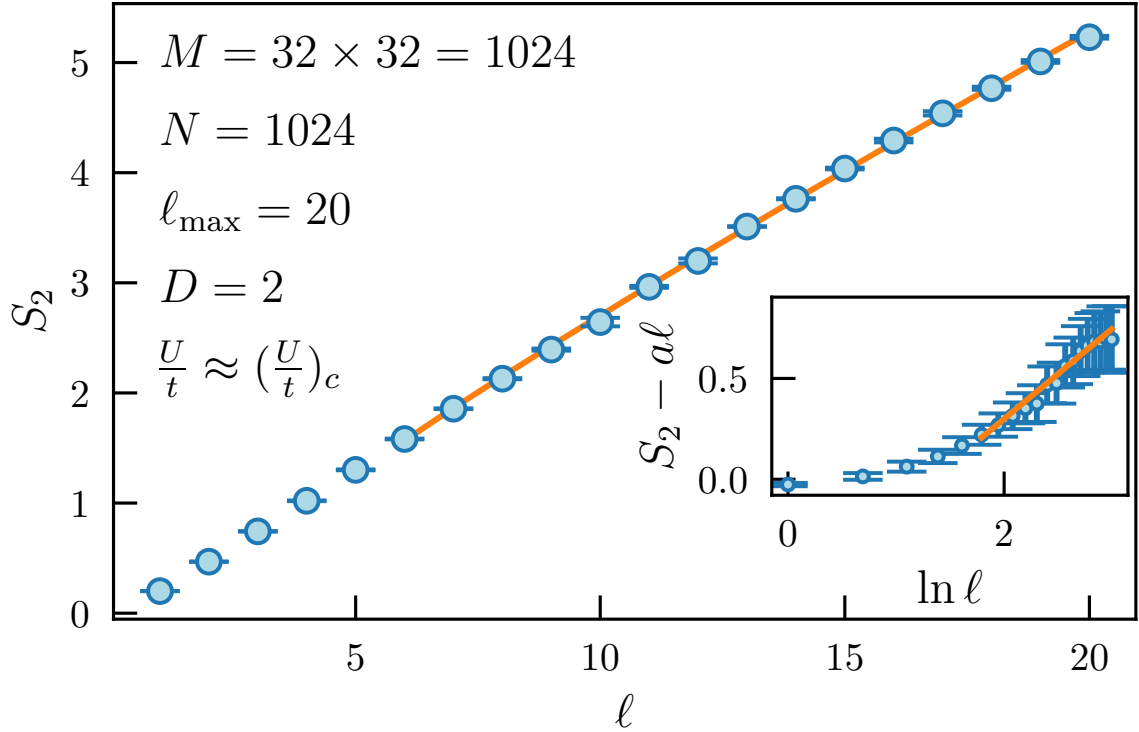


**Figure 3.8:** Finite-size scaling of the second Rényi Entropy in a square lattice of size  $M = 32 \times 32$  at unit-filling for various subregion sizes. The subregions are made up of lattice sites arranged as squares of linear sizes  $\ell = 1, 2, \dots, 20$ . The entanglement is seen to increase linearly with the boundary of the subregion. The data is fit to a linear model with a sub-leading correction term that is logarithmic in  $\ell$ , as shown in Eq. (3.35), yielding  $a \approx 0.2$ ,  $b \approx 0.5$ , and  $c \approx -0.6$ . The interaction strength was fixed to a value near the  $2D$  critical point. The inset shows a plot of  $S_2$  minus the leading term in Eq. (3.35), exposing the logarithmic dependence in  $\ell$  of the subleading term.

scaling form:

$$S_2(\ell) = a\ell + b \ln \ell + c, \quad (3.35)$$

where we ignore corrections of  $\mathcal{O}(1/\ell)$ , which we are unable to resolve with our current dataset. By subtracting off the dominant linear term in  $\ell$  scaling after fitting, we can investigate the sub-leading logarithmic correction as a function of subsystem linear size  $\ell$ , with the results shown in the inset of Fig. 3.8. In systems with a continuous symmetry breaking in the thermodynamic limit, the logarithmic correction,  $b$ , and constant,  $c$ , of Eq. (3.35) can contain universal information about the number of Goldstone modes, and the central charge of the underlying conformal field theory [66, 66, 67, 69–72, 156, 157]. Extracting this information will require access to the large system sizes possible with PIGSFLI, which opens up the door for further exploration of entanglement properties and scaling in the ground states of bosonic lattice models.

Having explored the  $\alpha = 2$  Rényi entanglement entropy, we now turn to the accessible entanglement entropy, named in this way due its original definition in terms of entanglement in a quantum many-body system accessible via local operations and classical communication [21]. In Fig. 3.9, we show results for a 1D Bose-Hubbard model of  $N = 8$  bosons at unit-filling under an equal size bipartition. Similar results have already been reported in the literature [41, 99], and these should be considered as demonstrating the utility of PIGSFLI in computing this important quantity. Quantum Monte Carlo results (symbols) are shown as a function of projection length along with values computed via exact diagonalization (solid line) for the same interaction strengths and system sizes ( $L = N = 8$ ) studied in Figs. 2.10 and 3.6. The accessible entanglement entropy  $S_2^{\text{acc}}$  is bounded from above by the full Rényi entanglement  $S_2$  and we find that it is considerably smaller, by a factor of 2 to 3 times in the Mott insulating phase and over 100 times in the superfluid phase. This is due to the fact that it is known to only be large near the quantum phase transition in this system [41] and goes to zero for the case of non-interacting bosons ( $U/t \rightarrow 0$ ) where

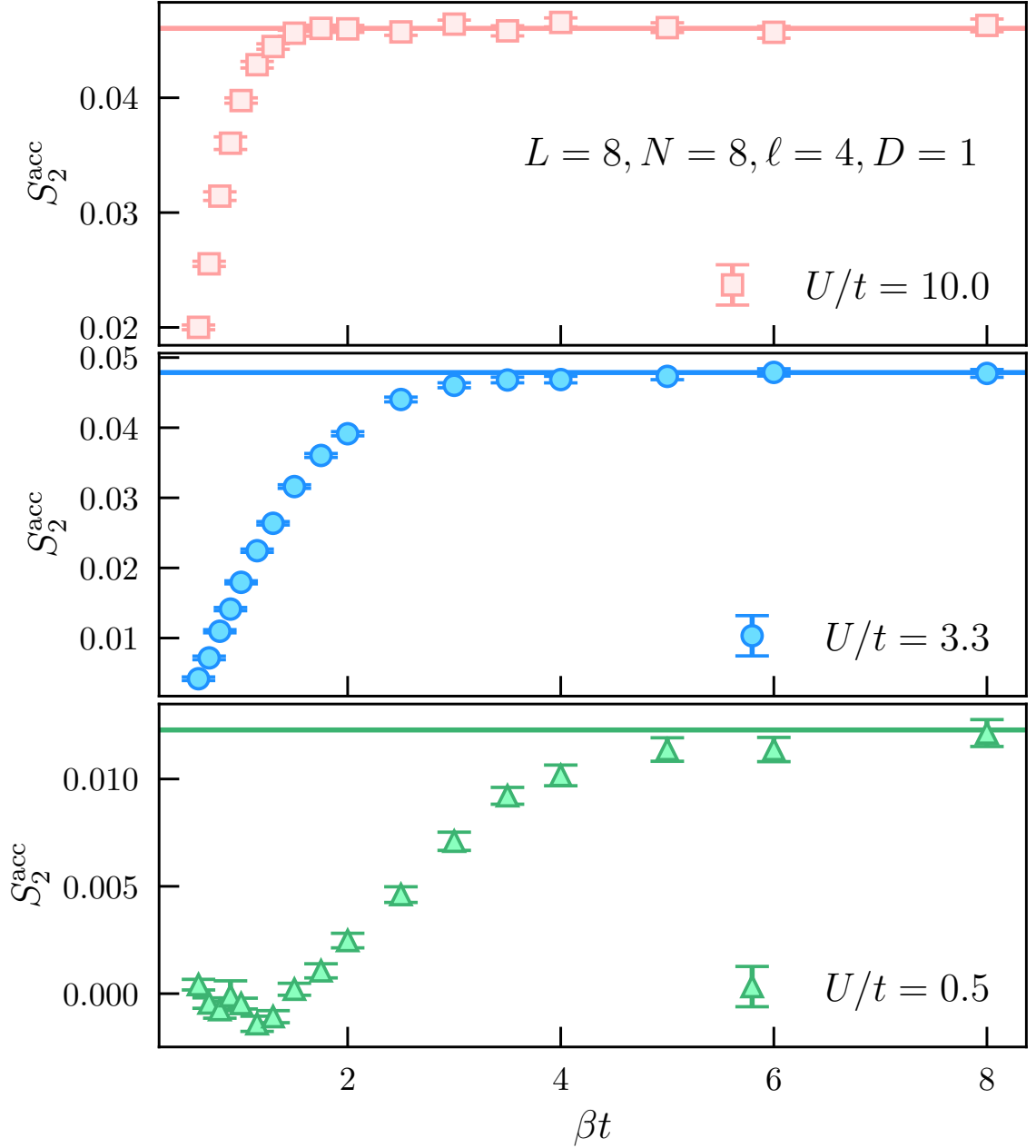


**Figure 3.9:**  $\beta$ -scaling of the accessible entanglement  $S_2^{\text{acc}}$  in a 1D chain of  $L = 8$  sites at unit-filling under equal bipartition of size  $\ell = 4$ . In contrast to the full Rényi entanglement entropies, larger values of  $\beta$  are needed to achieve similar accuracy, especially in the superfluid phase. The solid horizontal lines denote the exact value of the accessible entanglement at the respective interaction strength.

all entanglement is due to number fluctuations, or vanishes in the insulating phase, where the entanglement is non-accessible.

In Fig. 3.10, the symmetry-resolved entanglement entropy as a function of projection length is shown for the sector where the local particle number distribution  $P_n$  is maximal,  $n_{\max}$ , and its two adjacent sectors,  $n_{\max-1}$  and  $n_{\max+1}$ , with their corresponding exact diagonalization values shown as a solid horizontal line. Results are included for the same  $L = N = 8$  system from Fig. 3.9 with interaction strengths  $U/t = 0.5, 3.3, 10$ . For reference, the local particle number distributions,  $P_n$ , are shown for each value of the interaction strength. For  $U/t = 10$ , due to the strong repulsion between particles, the ground state configuration tends to an insulating state with one boson per site at unit-filling. Since the subregion is of size  $\ell = 4$ , it is seen that  $P_n$  is sharply peaked at a maximal value of  $n_{\max} = 4$ . In the superfluid phase with  $U/t = 0.5$  there are considerably larger particle number fluctuations, resulting in a broader  $P_n$ , although with the peak still at  $n_{\max} = 4$ .

The symmetry-resolved entropies corresponding to  $n_{\max} - 1$  and  $n_{\max} + 1$  are equivalent, up to statistical fluctuations due to the chosen partition and the symmetries of the Bose-Hubbard model [41]. When particle fluctuations are large, the symmetry resolved entanglement is nearly identical for  $n = n_{\max}, n_{\max} \pm 1$ , whereas in the insulating phase,  $n_{\max}$  may not correspond to maximal entanglement. For example, at  $U/t = 10$ , the contribution coming from the maximal sector is  $10\times$  smaller than the neighboring sectors, although their probability is much lower. This is because in the  $n_{\max}$  sector, the ground state in the Mott insulating phase is  $|\Psi_0\rangle_{\text{Mott}}^{n_{\max}} = |1, 1, \dots, 1\rangle_A \otimes |1, 1, \dots, 1\rangle_B$ , which is unentangled. In the  $n_{\max} - 1$  sector, the particles will once again try to repel each other, but there will be a vacancy in one of the  $A$  sites. The ground state then becomes a superposition of the only two possible states that have a hole in the  $A$  subregion that is adjacent to a doubly occupied site in the  $B$  subregion:  $|\Psi_0\rangle_{\text{Mott}}^{n_{\max}-1} = (|1, 1, \dots, 0\rangle_A \otimes |2, 1, \dots, 1\rangle_B + |0, 1, \dots, 1\rangle_A \otimes |1, 1, \dots, 2\rangle_B) / \sqrt{2}$ , which can be shown to have a second Rényi entanglement entropy of  $S_2 = \ln 2 \approx$

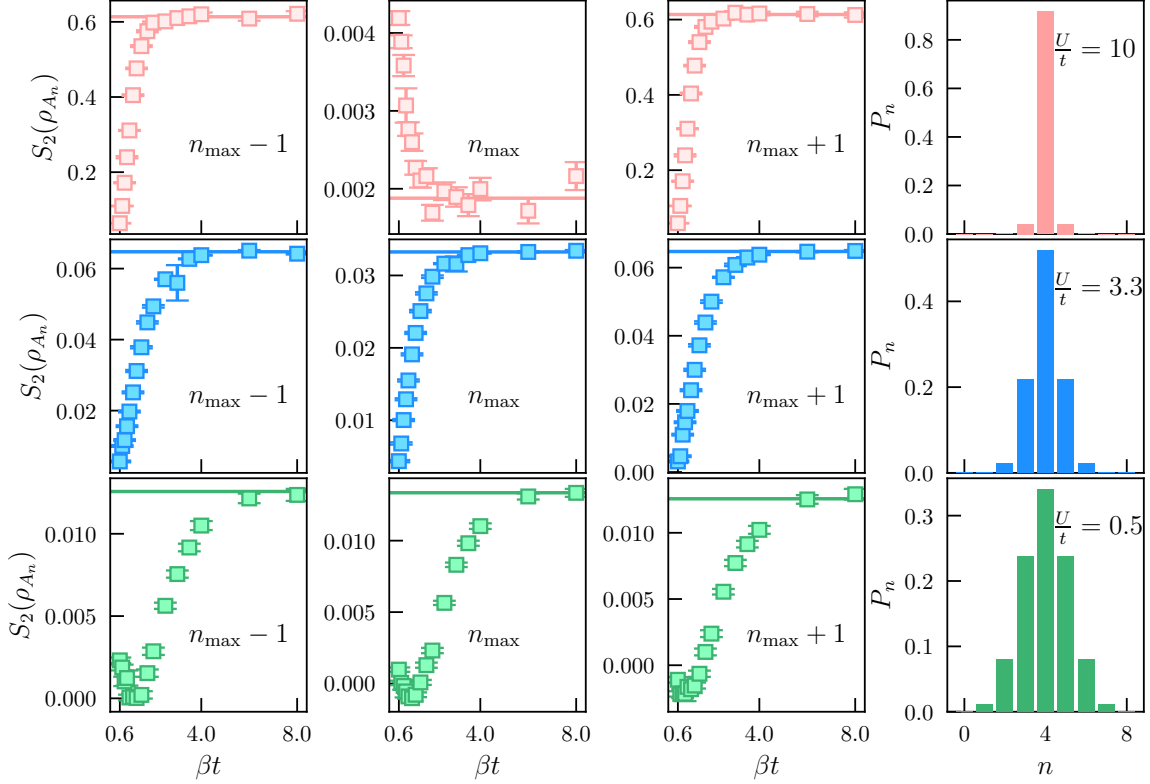


**Figure 3.10:** Imaginary time projection length  $\beta$ -scaling of the symmetry-resolved entanglement  $S_2(\rho_{A_n})$  in a 1D Bose-Hubbard chain of  $L = 8$  sites at unit-filling under an equal spatial bipartition of size  $\ell = 4$ . From top to bottom, the rows correspond to interaction strengths in the superfluid phase ( $U/t = 0.5$ ), at the phase transition ( $U/t = 3.3$ ), and in the Mott phase ( $U/t = 10$ ). The first three columns correspond to entanglement entropies in the maximal local particle number sector  $n_{\max}$  (i.e., with the largest probability), and the two neighboring sectors  $n_{\max} - 1$  and  $n_{\max} + 1$ . The solid horizontal lines are the exact diagonalization values for each symmetry resolved entanglement entropy. The rightmost column shows the local particle number distribution  $P_n$  at each of the three interaction strengths.

0.69... For the case of the insulating phase in the  $n_{\max} + 1$  sector, an equivalent argument can be applied to understand the value of the entanglement entropy.

As a practical matter, large  $\beta$  values are required in Fig. 3.9 and Fig. 3.10 for the PIGSFLI algorithm to converge on results with small relative errors, however in all interaction regimes, we find agreement with the exact result. Improved sampling procedures can be directly implemented (e.g. performing parallel simulations in different restricted  $n$ -sectors) to improve efficiency and statistical convergence. These results represent the first quantum Monte Carlo measurement of the Rényi generalized accessible entanglement in the Bose-Hubbard model.

Fig. 3.11 shows results for the symmetry-resolved entanglement entropy as a function of local particle number sector  $n$  for a 1D Bose-Hubbard model with  $N = 64$  bosons at unit filling under an equal spatial bipartition of size  $\ell = 32$  near the quantum critical point,  $U/t = 3.3$ . This result demonstrates the capability of our algorithm to compute the symmetry-resolved entanglement entropy in much larger systems than have been previously possible, even in strongly interacting quantum many-body systems. The bottom panel of Fig. 3.11 shows the probability distribution of local particle number in the  $A$  subregion. Notice that due to the onset of Mott insulating behavior, a similar behavior to Fig. 3.10 is observed, where the symmetry-resolved entanglement entropy at the maximal sector,  $n_{\max} = 32$ , is actually smaller than its two adjacent neighbors. In principle, the symmetry-resolved entanglement entropy is generally finite for the rest of the local particle numbers not shown, however as sectors outside of this range occur with increasingly vanishing probability, in practice they cannot be sampled without large statistical errors. This is apparent in the figure as  $|n - n_{\max}| > 1$ . The non-monotonic dependence of  $S_2(\rho_{A_n})$  with the minimum occurring at  $n_{\max}$  can be interpreted as originating from the presence of holon and doublon quasiparticles when the subsystem is away from unit-filling, on the insulating side of the phase transition .

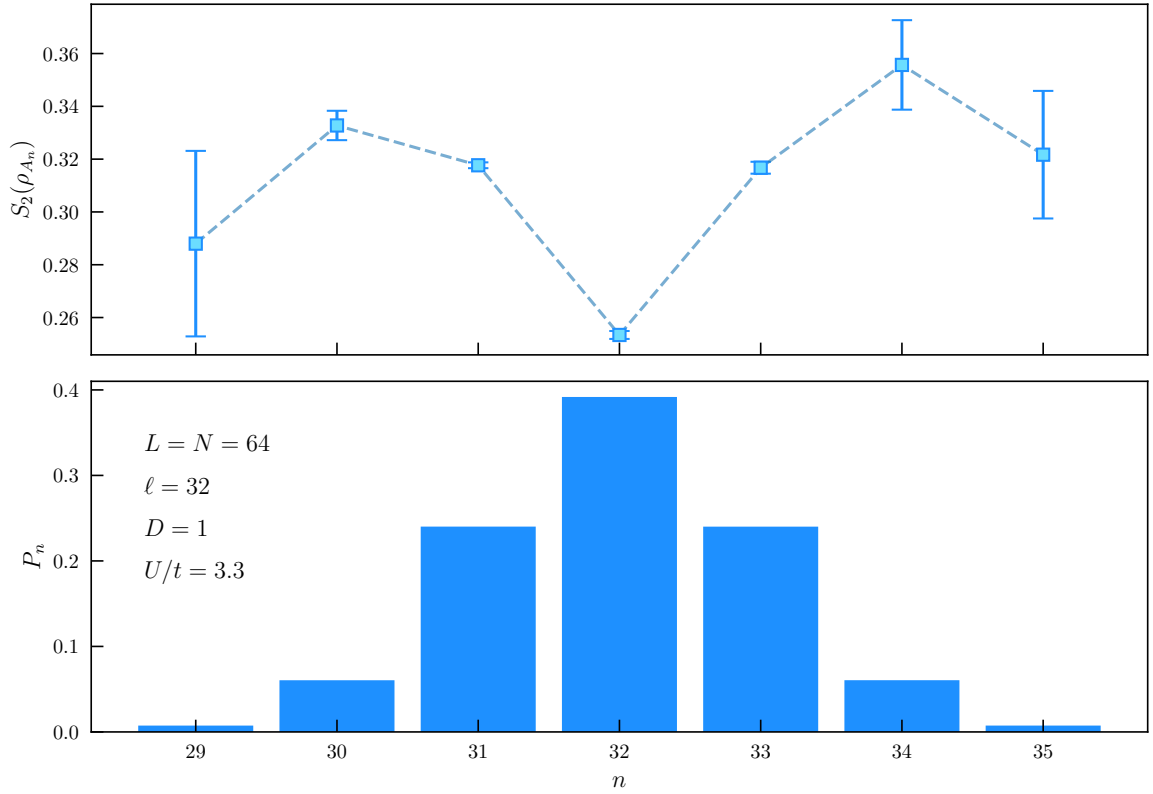


**Figure 3.11:** Symmetry-resolved Rényi entanglement entropies as a function of local particle number sector,  $n$ . The system is a one-dimensional lattice of  $N = 64$  bosons at unit-filling under an equal spatial bipartition  $\ell = 32$  near the critical interaction strength  $U/t = 3.3$ . The bottom panel shows the local particle number distribution,  $P_n$ , for this system.



### 3.10 Conclusion

In this chapter, we have introduced a ground state lattice Path Integral quantum Monte Carlo algorithm to compute the entanglement properties of interacting bosons at zero temperature. The algorithm was further expanded to allow for the calculation of the full, operationally accessible, and symmetry resolved spatial Rényi entanglement entropies where we again provided benchmarks against exact results across the phase diagram of the 1D Bose-Hubbard model. As has been previously reported, we observe that entanglement is sensitive to the quantum phase transition between the insulating and superfluid phases. To highlight the  $O(L^D)$  performance of the quantum Monte Carlo implementation for a  $D$ -dimensional lattice of linear dimension  $L$  we reported new results of spatial entanglement for a  $D = 1$  chain of  $L = 256$  sites at unit-filling. Moving beyond  $D = 1$ , we also demonstrated the entanglement scaling with boundary size for a  $D = 2$  system of  $M = 32 \times 32 = 1024$  lattice sites at unit-filling, with square subregions that ranged from as small as  $\ell^D = 1 \times 1$  to  $\ell^D = 20 \times 20$ . These results are consistent with the entanglement boundary law,  $S_2 \sim \ell$ . Finally, by utilizing the superselection rule corresponding to fixed total particle number, we computed the accessible entanglement for a  $D = 1$  Bose-Hubbard chain, as well as highlighting its value for a few symmetry resolved subsectors corresponding to  $n$  particles in the subsystem near the peak of the particle number distribution. While we have only studied these quantities in small systems, they demonstrate proof-of-principle calculations that can be straightforwardly extended to uncover the finite size scaling of this experimentally important entanglement measure. Our implementation, dubbed PIGSFLI, has been released as open source [80].

Further development of this algorithm can be pursued in future work, including incorporating optimizations such as the “ratio method” [8, 12] that have been previously utilized to improve sampling statistics in larger systems by building up the entanglement from a ratio of estimators for smaller spatial subregions. The addition of different lattice connectivities or moving to extended range Bose-Hubbard models

(both hopping and interactions) presents no fundamental algorithmic challenge and will allow for the measurement of entanglement in the ground states of a large class of interacting lattice Hamiltonians. Moving to higher order Rényi entropies with  $\alpha > 2$  is also possible by including additional replicas and the updates required to insert and remove **SWAP** kinks between them. Finally, it may also be possible to extend the algorithm to study entanglement measures more suitable for mixed states, such as the negativity.

## Chapter 4

# Finite Size Scaling of Entanglement in the $1D$ Bose-Hubbard Model

In this chapter, we apply our new lattice PIGS algorithm, PIGSFLI, to investigate the entanglement scaling with subsystem size in the one-dimensional Bose-Hubbard model. We derive scaling forms with subsystem size for the symmetry-resolved and accessible entanglement entropies in the Bose-Hubbard model for itinerant bosons [23]. PIGSFLI simulations [158] will allow for the numerical confirmation of the derived scaling forms in systems of up to  $N = 64$  bosons at unit filling both near the quantum critical point and in the superfluid phase, where weak interactions allowing large particle number fluctuations causing DMRG to be prone to large errors in the accessible and symmetry-resolved entanglement [41]. Additionally, numerical estimates for the central charge underlying the conformal field theory (CFT) and for the Luttinger parameter are extracted and shown to agree with the predictions from their underlying theories.

## 4.1 Entanglement Measures

The entanglement between a partition of a system,  $A$ , and its complement,  $B$ , can be computed via the Rényi entanglement entropy:

$$S_\alpha(\rho_A) = \frac{1}{1-\alpha} \ln \text{Tr} \rho_A^\alpha. \quad (4.1)$$

For a pure state,  $|\Psi\rangle$ , the reduced density matrix of subsystem,  $\rho_A$ , is obtained by tracing out the degrees of freedom of the complementary subregion from the full density matrix,  $\rho_A = \text{Tr}_B |\Psi\rangle \langle\Psi|$ . In the limit  $\alpha \rightarrow 1$ , the Rényi EE becomes the von Neumann entropy:  $S_1 = -\text{Tr}(\rho_A \ln \rho_A)$ , a quantum information theory equivalent of the Shannon entropy. The second Rényi EE,  $S_2 = -\ln \text{Tr} \rho_A^2$ , has garnered much interest since the purity,  $\text{Tr} \rho_A^2$ , can be rewritten as a quantum expectation value of a local  $\text{SWAP}_A$  operator [8] that is tractable in quantum Monte Carlo (QMC) [9, 9–11, 158] and even experimentally [18–20].

Conformal field theory (CFT) predicts an asymptotic scaling form for the spatial Rényi entanglement entropy in an infinite  $1d$  system with subregion  $A$  comprised of  $\ell$  sites that is logarithmic in subsystem size, with non-universal  $\mathcal{O}(1)$  corrections [73]:

$$S_{\alpha|1D \text{ CFT}} = \frac{c}{6} \left(1 + \frac{1}{\alpha}\right) \ln \frac{\ell}{a_0} + c_\alpha, \quad (4.2)$$

where  $c$  is the central charge underlying the CFT,  $a_0$  is a short-distance cutoff, and  $c_\alpha$  is a non-universal constant. If the system is subject to periodic boundary conditions, Eq. (4.2) is then rewritten in terms of a cord length,  $D(\ell) = L/\pi \sin(\pi\ell/L)$ , where  $L$  is the total system size, by replacing  $\ell \rightarrow D(\ell)$  to account for distances measured around a ring.

Particle number superselection rules restrict the amount of entanglement operationally accessible as a resource for quantum information processing [21, 22]. The quantification of this accessible entanglement was originally introduced as an average of von Neumann entropies over sectors of fixed local particle number in the subsystem:

$S_1^{\text{acc}}(\rho_A) = \sum_n P_n S_1(\rho_{A_n})$  [21] and has since been generalized in terms of Rényi EE's [22]:

$$S_\alpha^{\text{acc}}(\rho_A) = \frac{\alpha}{1-\alpha} \ln \left[ \sum_n P_n e^{\frac{1-\alpha}{\alpha} S_\alpha(\rho_{A_n})} \right]. \quad (4.3)$$

The quantity  $S_\alpha(\rho_{A_n})$  is the symmetry-resolved entanglement for fixed particle number sector  $n$  and it is obtained as a Rényi EE, Eq. (4.1), for projections of the reduced density matrix onto the subspace of fixed  $n$ :

$$\rho_{A_n} = \frac{\Pi_n \rho_A \Pi_n}{P_n}, \quad (4.4)$$

where  $\Pi_n$  is a projection operator onto the subspace of fixed  $n$  and  $P_n = \text{Tr} \rho_{A_n}$  gives the probability of subsector  $n$ . The quantification of the symmetry-resolved and accessible entanglement entropies is an active field of research [22, 41, 42, 78, 98, 99, 113–145]. This quantity is important as its average over symmetry-resolved sectors, the accessible entanglement, sets an upper bound on the amount of entanglement that can be transferred via LOCC from a quantum many-body system to a qubit register [99]. With PIGSFLI, we now have the capability to compute the symmetry-resolved EE in any regime of the phase diagram of interacting bosonic lattices.

## 4.2 Bose-Hubbard Model

The Bose-Hubbard model for itinerant bosons on a lattice [23] is:

$$H = -t \sum_{\langle i,j \rangle} b_i^\dagger b_j + \frac{U}{2} \sum_i n_i(n_i - 1) - \mu \sum_i n_i, \quad (4.5)$$

where  $t$  is the tunneling between neighboring lattice sites  $\langle i, j \rangle$ ,  $U > 0$  is a repulsive interaction potential,  $\mu$  is the chemical potential, and  $b_i^\dagger (b_i)$  are bosonic creation(annihilation) operators on site  $i$ , satisfying the commutation relation:  $[b_i, b_j^\dagger] = \delta_{i,j}$ , with  $n_i = b_i^\dagger b_i$  the local number operator.

This model exhibits a Berezinskii–Kosterlitz–Thouless (BKT) quantum phase transition from a superfluid phase, where particle interactions are weak, into a Mott insulator, where strong repulsive interactions cause the bosons to become highly localized, with the system tending to one particle on each site for the case of unit filling and  $U/t \rightarrow \infty$ . The exact location of the quantum critical point is not known, but it has been approximated with a diverse array of methods [24–39], with recent estimates suggesting that  $(U/t)_c \gtrsim 3.3$ . In this chapter, the subsystem scaling of the symmetry-resolved entanglement is numerically confirmed via our PIGS algorithm [158] in systems up to  $N = 64$  bosons at unit filling ( $L = N$ ), much larger than what is possible with exact diagonalization (ED), at interaction strengths of  $U/t = 3.3$ , near the superfluid-insulating critical point, and at  $U/t = 2.0$ , inside the superfluid phase, where the accessible entanglement can be prone to large errors using DMRG [41], since the maximum on-site number of particles needs to be restricted but in this phase weak interactions allow large particle number fluctuations.

### 4.3 Scaling of operationally accessible entanglement

For  $1d$  systems described by Tomonaga Luttinger Liquid (TLL) theory [4], such as the superfluid phase of the Bose-Hubbard model, the amount of non-accessible entanglement,  $\Delta S_\alpha = S_\alpha - S_\alpha^{\text{acc}}$ , can be related to the local particle number variance or bipartite fluctuations,  $\sigma^2$  [42]. Moreover, in the limit  $\ell \gg 1$ , bipartite fluctuations scale with subsystem size as [39] :

$$\sigma^2 \equiv \langle n^2 \rangle - \langle n \rangle^2 = \frac{K}{\pi^2} \ln \frac{D(\ell)}{a_0}, \quad (4.6)$$

where  $K$  is the Luttinger parameter and, due to periodic boundary conditions,  $\ell \rightarrow D(\ell)$  is taken to account for distances measured around a ring, where  $D(\ell) = L/\pi \sin(\pi\ell/L)$  is the subsystem cordlength. The difference between full and accessible

entanglement entropies, referred to here as non-accessible EE, has been previously seen to be related to bipartite fluctuations [42]:

$$\Delta S_\alpha \equiv S_\alpha - S_\alpha^{\text{acc}} = \frac{1}{2} \ln \sigma^2 + \frac{1}{2} \ln [2\pi\alpha^{1/(\alpha-1)}]. \quad (4.7)$$

Combining Eq. (4.6) and Eq. (4.7) for  $\alpha = 2$ , a scaling form for the non-accessible second Rényi entanglement entropy is obtained:

$$\Delta S_2(\ell) = S_2(\ell) - S_2^{\text{acc}}(\ell) = \frac{1}{2} \left[ \ln \ln \frac{D(\ell)}{a_0} + \ln K + \ln \frac{4}{\pi} \right]. \quad (4.8)$$

The scaling with subsystem size of the first term,  $S_2(\ell)$ , which is the full second Rényi EE is obtained from its CFT prediction, Eq. (4.2), by taking  $\alpha = 2$ :

$$S_{2|1D \text{ CFT}}(\ell) = \frac{c}{4} \ln D(\ell) + \tilde{c}_2, \quad (4.9)$$

where the short-distance cutoff has been absorbed into the additive constant,  $\tilde{c}_2$ .

Solving Eq. (4.8) for  $S_2^{\text{acc}}(\ell)$ , the subsystem size scaling of the accessible entanglement then becomes:

$$S_2^{\text{acc}}(\ell) = \frac{c}{4} \ln D(\ell) - \frac{1}{2} \ln \ln \frac{D(\ell)}{a_0} + c_2^{\text{acc}}, \quad (4.10)$$

where additive constants have been absorbed into  $c_2^{\text{acc}}$ . Eq. (4.10) constitutes a new result that to our knowledge has not been presented before in the literature.

In Fig. 4.1, accessible entanglement results as a function of cordlength obtained by performing simulations using PIGSFLI are shown. The data is fitted to Eq. (4.10), excluding smaller subsystem sizes to minimize finite size effects, good agreement is seen for both interaction strengths.

Due to the equivalence between the superfluid and Tomonaga Luttinger Liquid, the central charge of the CFT is expected to be  $c = 1$  [4, 75], a result obtained with PIGSFLI, within error bars. The larger values of  $S_2^{\text{acc}}$  for  $U/t = 3.3$ , compared

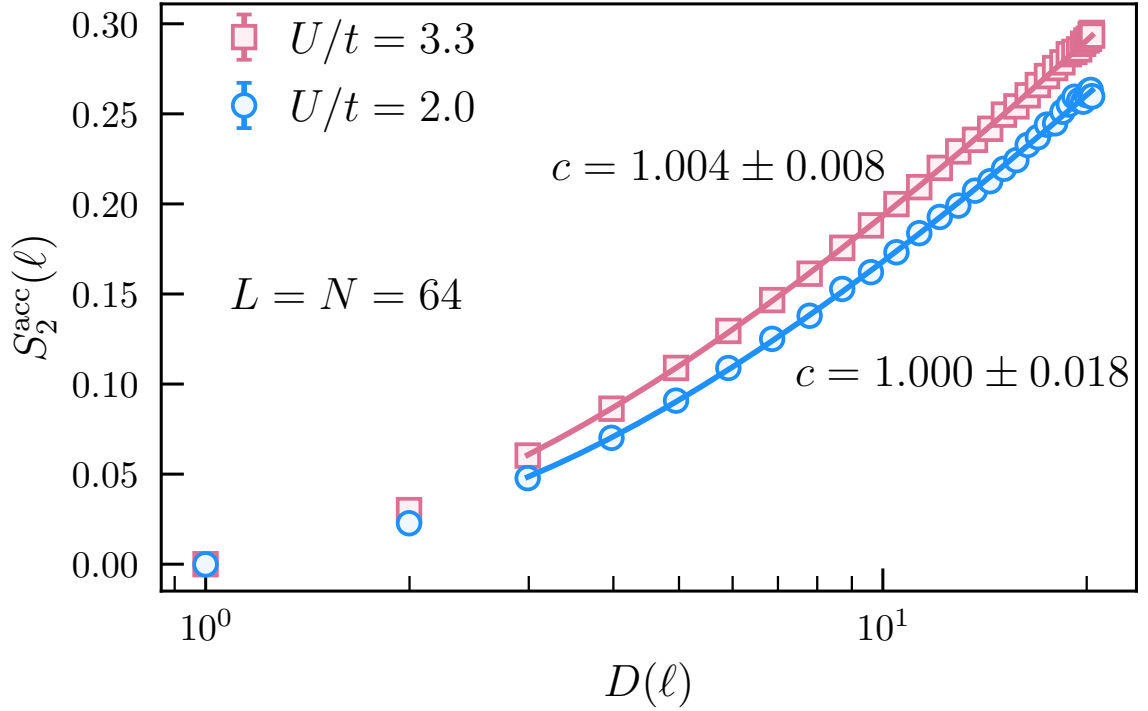


**Figure 4.1:** Accessible entanglement scaling with subsystem cordlength. The system consists of  $L = 64$  sites at unit filling with interaction strengths  $U/t = 2.0$ , in the superfluid phase, and  $U/t = 3.3$ , near the superfluid-insulating quantum critical point. The data points were obtained from PIMC and are fitted to Eq. (4.10), shown as a solid line. Fit parameters are shown as annotations, with the central charge agreeing with the CFT prediction,  $c = 1$ .



to  $U/t = 2.0$ , are reflective of the previously observed result that the accessible entanglement is maximal near the superfluid-insulating phase transition [41]. The Monte Carlo estimates have been obtained by averaging over many seeds and using the jackknife method for error bar estimation.

In the next section, we derive this symmetry-resolved scaling, but from relationships between entanglement entropies and bipartite fluctuations.

## 4.4 Scaling of symmetry-resolved entanglement

Due to the block diagonal structure of  $\rho_A$ , the purity of a reduced density matrix projected onto the subspace of fixed local particle number  $n$  can be written:

$$\mathrm{Tr} \rho_{A_n}^2 = \frac{\mathrm{Tr}(\Pi_n \rho_A^2 \Pi_n)}{P_n^2}, \quad (4.11)$$

where  $\Pi_n$  is a projection operator onto the subspace of fixed local particle number  $n$  and  $P_n$  is the probability of  $n$  particles in the subsystem. The negative of the natural logarithm of this quantity can be identified as the symmetry-resolved second Rényi entanglement entropy for particle sector  $n$ :

$$s_2(n) = -\ln \mathrm{Tr} \rho_{A_n}^2 = -\ln \left[ \frac{\mathrm{Tr}(\Pi_n \rho_A^2 \Pi_n)}{P_n^2} \right], \quad (4.12)$$

where we use the short-hand notation  $S_2(\rho_{A_n}) \equiv s_2(n)$ . The local particle number distribution,  $P_n$ , in critical  $1d$  systems described by Luttinger liquid theory (or, more generally, for CFT's with conserved  $U(1)$  current), such as the superfluid phase of the BH model, is Gaussian [98] with mean  $\langle n \rangle$  and variance  $\sigma^2$ . In Ref [42], it was shown that the trace in the numerator of Eq. (4.12) can be related to an auxiliary local particle number distribution  $P_{n,\alpha}$ , defined:

$$P_{n,\alpha} = \frac{\mathrm{Tr}(\Pi_n \rho_A^\alpha \Pi_n)}{\mathrm{Tr} \rho_A^\alpha}, \quad (4.13)$$

that is also Gaussian with the same mean,  $\langle n \rangle$ , but modified variance  $\sigma_\alpha^2 = \sigma^2/\alpha$  [42]. Solving Eq. (4.13) for  $\text{Tr}(\Pi_n \rho_A^\alpha \Pi_n)$ , it is seen that:

$$\text{Tr}(\Pi_n \rho_A^\alpha \Pi_n) = P_{n,\alpha} \text{Tr} \rho_A^\alpha. \quad (4.14)$$

Substituting this result into Eq. (4.12) with  $\alpha = 2$ , the second Rényi symmetry-resolved EE can be rewritten in terms of  $P_n, P_{n,2}$ , and  $\text{Tr} \rho_A^2$ :

$$s_2(n) = -\ln \left[ \frac{P_{n,2}}{P_n^2} \text{Tr} \rho_A^2 \right]. \quad (4.15)$$

The trace inside the logarithm can be computed by recalling that the second Rényi EE is  $S_2 = -\ln \text{Tr} \rho_A^2$  and thus  $\text{Tr} \rho_A^2 = e^{-S_2}$ . Substituting this result into Eq. (4.15), the symmetry-resolved EE can be written in terms of the full second Rényi EE:

$$s_2(n) = S_2 - \ln \left[ \frac{P_{n,2}}{P_n^2} \right]. \quad (4.16)$$

The second term in Eq. (4.16) can be found to scale with system size by first expressing the distributions  $P_n$  and  $P_{n,2}$  explicitly in Gaussian form:

$$P_n = \frac{1}{\sqrt{2\pi\sigma^2}} e^{-\frac{(n-\langle n \rangle)^2}{2\sigma^2}}, \quad (4.17)$$

and

$$P_{n,2} = \frac{1}{\sqrt{2\pi\sigma_2^2}} e^{-\frac{(n-\langle n \rangle)^2}{2\sigma_2^2}}. \quad (4.18)$$

The ratio arising in the logarithm of Eq. (4.16) then becomes a function of bipartite fluctuations:

$$\frac{P_{n,2}}{P_n^2} = \sqrt{4\pi\sigma^2}. \quad (4.19)$$

Substituting the scaling forms for the bipartite fluctuations, Eq. (4.6), and second Rényi EE, Eq. (4.9), into Eq. (4.16), the subsystem scaling of the symmetry-resolved

entanglement is then given by:

$$s_2(\ell, n) = \frac{c}{4} \ln D(\ell) - \frac{1}{2} \ln \ln \frac{D(\ell)}{a_0} + c_2^{\text{SRE}}, \quad (4.20)$$

where additive constants have been absorbed into  $c_2^{\text{SRE}}$ . The symmetry-resolved entanglement scaling with subsystem size in systems with Gaussian local particle number distributions is then independent of particle number sector, a property previously referred to as *entropy equipartition* [78, 79]. Comparing Eq. (4.10) and Eq. (4.20), we arrive to the surprising result that the accessible and symmetry-resolved entanglement possess identical leading and sub-leading scaling forms, up to  $\mathcal{O}(1)$  corrections.

Fig. 4.2 shows lattice PIMC results for the scaling with cordlength of the symmetry-resolved entanglement for the sector where the local particle number probability distribution,  $P_n$ , is maximal,  $n_{\text{max}}$ , and adjacent sector,  $n_{\text{max}} - 1$ . The system consists of 64 particles at unit filling, for interaction strengths  $U/t = 3.3$  and  $U/t = 2.0$ , near the quantum critical point and in the superfluid phase, respectively. The Monte Carlo data points and fit show good agreement, the scaling is seen to be valid for both local particle number sectors, and the central charge obtained from fitting gives an estimate close to the expected  $c = 1$ .

The symmetry-resolved and accessible entanglement subsystem scaling forms have allowed for the estimation of the central charge underlying the CFT in the finite sized systems shown. In the next section, we show how the Luttinger parameter  $K$  can be estimated from a relation obtained from the scaling form of the difference  $\Delta S_2 = S_2 - S_2^{\text{acc}}$ .

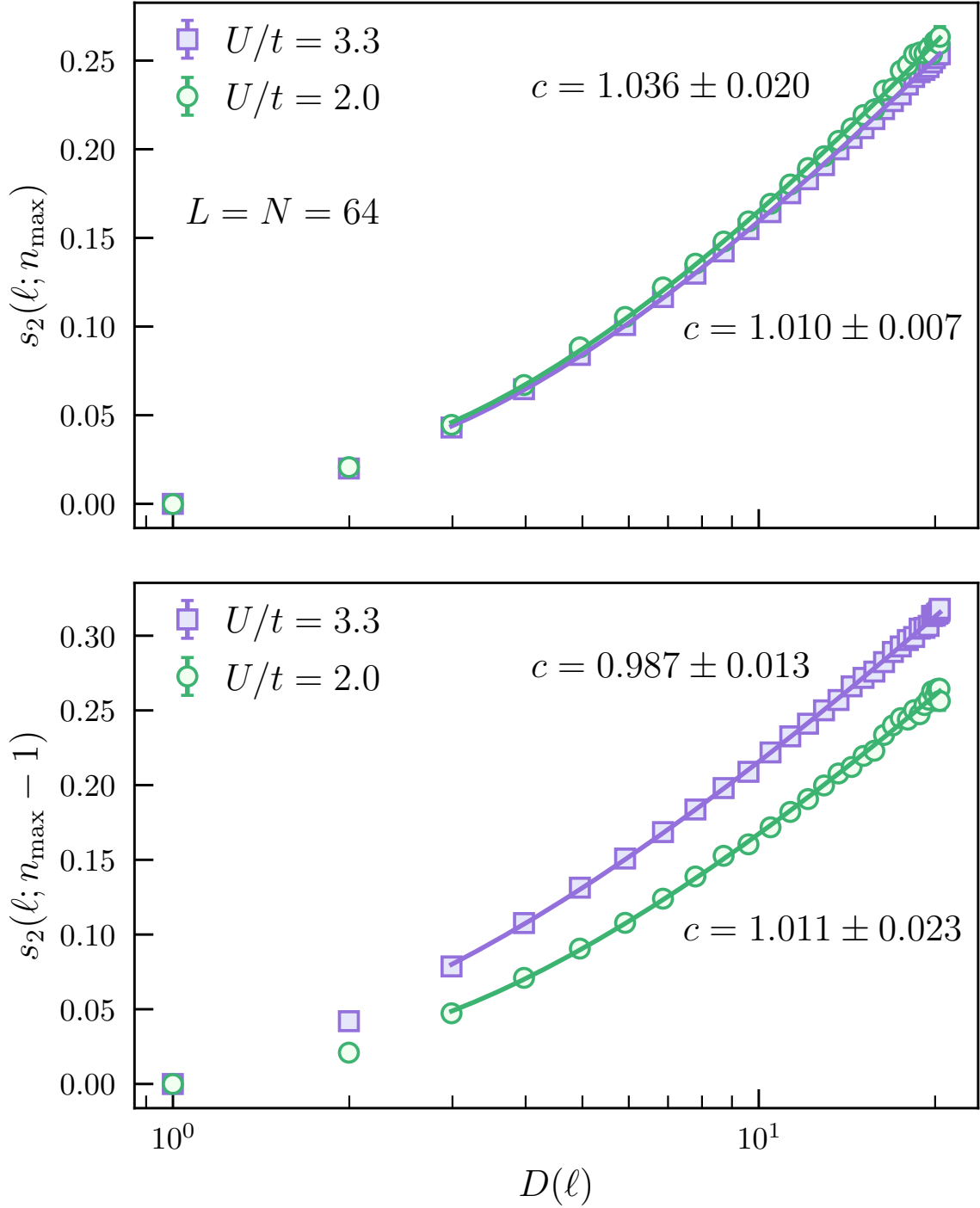


**Figure 4.2:** Scaling of the symmetry-resolved entanglement with subsystem scaling. The results shown correspond to the local particle number sector where the probability distribution,  $P_n$ , is maximal,  $n_{\max}$ , and adjacent sector,  $n_{\max} - 1$ . Monte Carlo data points are fitted to Eq. (4.20) and the corresponding fit parameters are shown as annotations.

## 4.5 Luttinger parameter extraction from non-accessible entanglement

In the derivation that led to the accessible entanglement scaling, Eq. (4.10), the scaling for the difference,  $\Delta S_2$ , the non-accessible entanglement, was obtained in Eq. (4.8). Doubling this scaling then taking its exponential, the following expression is obtained:

$$e^{2\Delta S_2(\ell)} = \frac{4K}{\pi} \ln D(\ell) + c_2^\Delta. \quad (4.21)$$

With this result, the Luttinger Parameter can be extracted by performing a simple linear fit in  $\ln D(\ell)$ . Moreover, plotting as a line provides an easier way of appreciating the effectiveness of the fit across its domain. Fig. 4.3 shows PIMC results for  $e^{2\Delta S_2(\ell)}$ , with the data fitted to Eq. (4.21). The Tomonaga-Luttinger parameter obtained from this fit is  $K \approx 2.1$ , close to but slightly above the Luttinger Liquid theory predicted result at the superfluid-insulating critical point,  $K_c = 2$  [4]. This result suggests that to get closer to the critical interaction strength, we need to slightly increase  $U/t = 3.3$ , since the Luttinger parameter has been previously seen to decrease monotonically as a function of  $U/t$  in the Bose-Hubbard model [39]. A more accurate determination of this quantum critical point can be a future research avenue. This method showcases a supplementary approach for the estimation of  $K$  to those that depend on the calculation of the correlation function and bipartite fluctuations [39].

## 4.6 Conclusion

In this chapter, we have found scaling forms for the accessible and symmetry-resolved entanglement entropies in  $1d$  systems with Gaussian local particle number distribution. The scaling of the symmetry-resolved entanglement was seen to be independent of local particle number. Additionally, both the accessible and the symmetry-resolved entanglement were seen to possess identical subsystem scaling

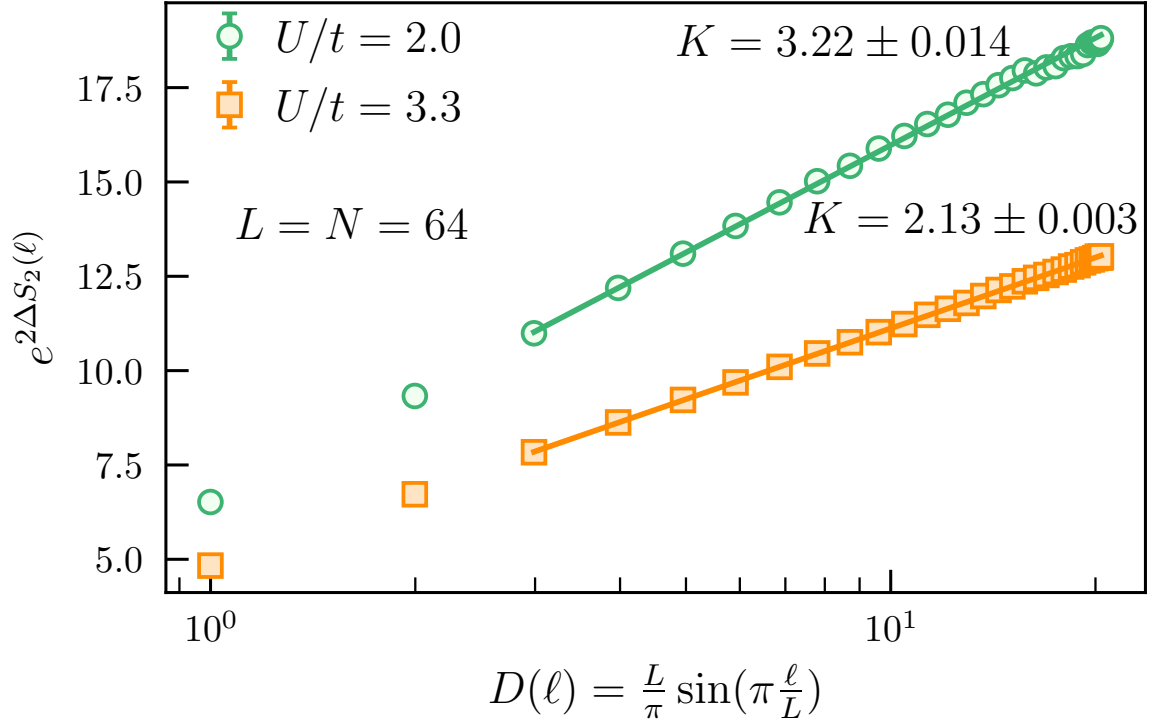


**Figure 4.3:** Extraction of Luttinger Parameter,  $K$ , via fit to  $e^{2\Delta S_2(\ell)}$ . The scaling form obtained for the difference  $\Delta S_2$  is doubled and then exponentiated to obtain a linear relation in  $D(\ell)$  from which the slope is directly proportional to  $K$ . Near the critical interaction strength, Renormalization Group theory predicts that  $K_c = 2$  [4], with its value increasing deeper in the superfluid phase, at lower interaction strengths.

forms, up to  $\mathcal{O}(1)$  corrections. These scaling forms were numerically confirmed in one dimensional Bose-Hubbard lattices of 64 particles at unit filling via lattice PIGS simulations near the superfluid-insulating phase transition and deep in the superfluid phase. The central charge underlying the CFT was obtained to excellent agreement with the expected result,  $c = 1$  for the superfluid phase and near the phase transition. Moreover, a scaling form for the difference  $\Delta S_2$ , the amount of non-accessible entanglement, was obtained. From this, a linear form in  $\ln D(\ell)$  was derived that allowed for Luttinger parameter estimation from a fit to its slope. Near the quantum critical point, we obtained  $K \approx 2.1$ , close to the TLL prediction of 2.0, suggesting that the interaction strength  $U/t = 3.3$  is near, albeit slightly lower than the actual critical point. In the superfluid phase, the extracted  $K$  was larger, agreeing with TLL theory, which predicts that this value increases with decreasing interaction strength.

Some avenues of future exploration that open up based on the results reported here are to investigate the Luttinger parameter across a range of interaction strengths in thermodynamic limit, and obtaining scaling forms in two dimensional lattices, for which the new lattice PIGS algorithm used here has been shown to be a viable tool for numerical exploration.

# Chapter 5

## Improving autocorrelation times via direct sampling of the truncated exponential distribution

### 5.1 Introduction

Sequential samples obtained in the random walk of a Markov Chain Monte Carlo (MCMC) simulation generally exhibit statistical correlations. The quality of a statistical estimate is directly related to the number of effectively uncorrelated samples obtained. A key challenge in the development of MCMC methods is therefore the reduction of computational time required to generate well-decorrelated samples.

One of the most ubiquitous MCMC methods is the Metropolis Algorithm [54, 159–161], where samples are obtained from a probability distribution that is often non-trivial to sample. In this algorithm, the principle of detailed balance leads to a non-negative acceptance ratio,  $R$ , for determining if randomly proposed configurations are accepted or rejected. Proposed configurations are only kept when this acceptance ratio is larger than a random number drawn from the uniform distribution,  $r \sim \mathcal{U}(0, 1)$ , such that  $r < R$ , and rejected otherwise. In most applications it is common



to encounter cases in which the acceptance ratio is small, leading to an inefficient Markov Chain as most proposed configurations are rejected. By carefully choosing the underlying probability distribution from which random variates in a Monte Carlo update are sampled, the acceptance ratio can be increased and even become unity so that every new configuration is accepted, thus improving the dynamics of the random walk and decreasing the correlation between subsequent samples.

In our recently developed Path Integral Monte Carlo (PIMC) algorithm [1], the acceptance ratio of most updates, depends on drawing random variates from a one or two dimensional truncated exponential distribution – an exponential distribution restricted to a finite domain. In this chapter, we describe how to directly sample two random variates from a two dimensional truncated exponential distribution, and apply this sampling strategy in PIMC. The resulting method leads to a reduction of autocorrelation times and therefore faster convergence of statistical averages to their exact values.

The chapter is organized as follows: In Section 5.2 we review how to sample variates from a one dimensional probability distribution by inverting the cumulative distribution function (CDF) of a probability density function (PDF). We will do this in the context of the one dimensional truncated exponential distribution. In Section 5.3, this method is then generalized to the non-trivial case of directly sampling two random variates from a two dimensional truncated exponential distribution. The direct sampling of variates from both one and two dimensional truncated exponential distributions is then applied to the PIGSFLI algorithm for the simulation of bosonic lattices at zero temperature and it is shown that direct sampling results in decreased autocorrelation times for the kinetic and potential ground state energies at no performance cost.

## 5.2 Direct sampling of 1D truncated exponential distribution

The one dimensional (1D) truncated exponential distribution is defined as:

$$P_1(x) = \frac{1}{\mathcal{Z}} e^{-c(x-a)} = \frac{ce^{-c(x-a)}}{1 - e^{-c(b-a)}}, \quad (5.1)$$

where  $a$  and  $b$  are the lower and upper bounds of the finite domain, respectively,  $c$  is a scale parameter, and  $x$  is a random variable in the truncation interval satisfying  $a \leq x \leq b$ . The factor  $\mathcal{Z}$  has been chosen to ensure that the distribution is normalized:  $\int_a^b dx P_1(x) = 1$ . The cumulative distribution function (CDF) of  $P_1(x)$  is,

$$F_1(x) \equiv \int_a^x dx' P_1(x') = \frac{1 - e^{-c(x-a)}}{c\mathcal{Z}}. \quad (5.2)$$

The inverse transform sampling method inverts the functional dependence  $y = F_1(x)$  to obtain samples from the target distribution  $x \sim P_1(x)$  of Eq. (5.1). The first step is to sample a random variable  $y$  uniformly between 0 and 1. We denote this random variable  $y \sim U(0, 1)$ . Then  $x = F_1^{-1}(y)$  yields a random variable with the desired target distribution,  $x \sim P_1(x)$ . Inverting the CDF in Eq. (5.2) we find:

$$x(y) = a - \frac{\ln(1 - c\mathcal{Z}y)}{c}. \quad (5.3)$$

When the CDF cannot be analytically inverted, a common practical approach attributed to von Neumann is rejection sampling [162, 163], which allows for the brute force sampling of  $P_1(x)$  on a finite domain with  $P_{1,\max} \equiv \max_{a \leq x \leq b} P_1(x)$  through the sequential comparison of two independently sampled random numbers.

### Rejection Sampling

1. Sample a random number from the uniform distribution  $x \sim U(a, b)$ .
2. Sample independently another random number from the uniform distribution  $\chi \sim U(0, P_{1,\max})$ .
3. If  $\chi < P_1(x)$  then accept  $x$ . Otherwise, reject the proposal and return to step 1.

The value  $x$  returned by this procedure will be a good sample from the distribution  $P_1$ . Note, however, that if  $P_1$  deviates strongly from  $U(a, b)$  then there are likely to be many rejections before a good sample is returned.

While rejection sampling is not necessary here due to the existence of the inverse, to setup our analysis of the  $2D$  case, we compare direct and rejection sampling by generating a histogram of random samples  $x \sim P_1$  using both methods. The results are shown in Fig. 5.1 for  $8 \times 10^5$  samples. Both histograms agree with the expected result in Eq. (5.1), but fluctuations are larger for the rejection sampling case.

This can be attributed to the large number of good samples in the direct sampling dataset, since random variates obtained from Eq. (5.1) are always accepted. In contrast, a significant fraction of iterations for the rejection sampling method did not lead to a good sample.

For a one dimensional probability distribution, such as  $P_1(x)$ , a Kolmogorov-Smirnov (KS) test can be used to quantify how well the random variate dataset follows the target distribution. Fig. 5.2 shows the KS-distance or KS-statistic, which measures the maximum difference between empirical and theoretical CDFs, as a function of the number of samples in the dataset. For the direct sampling dataset, the KS-distance decays much faster than for the rejection sampling dataset. This is expected, because the rejection sampling dataset contains fewer statistical samples from Eq. (5.1).

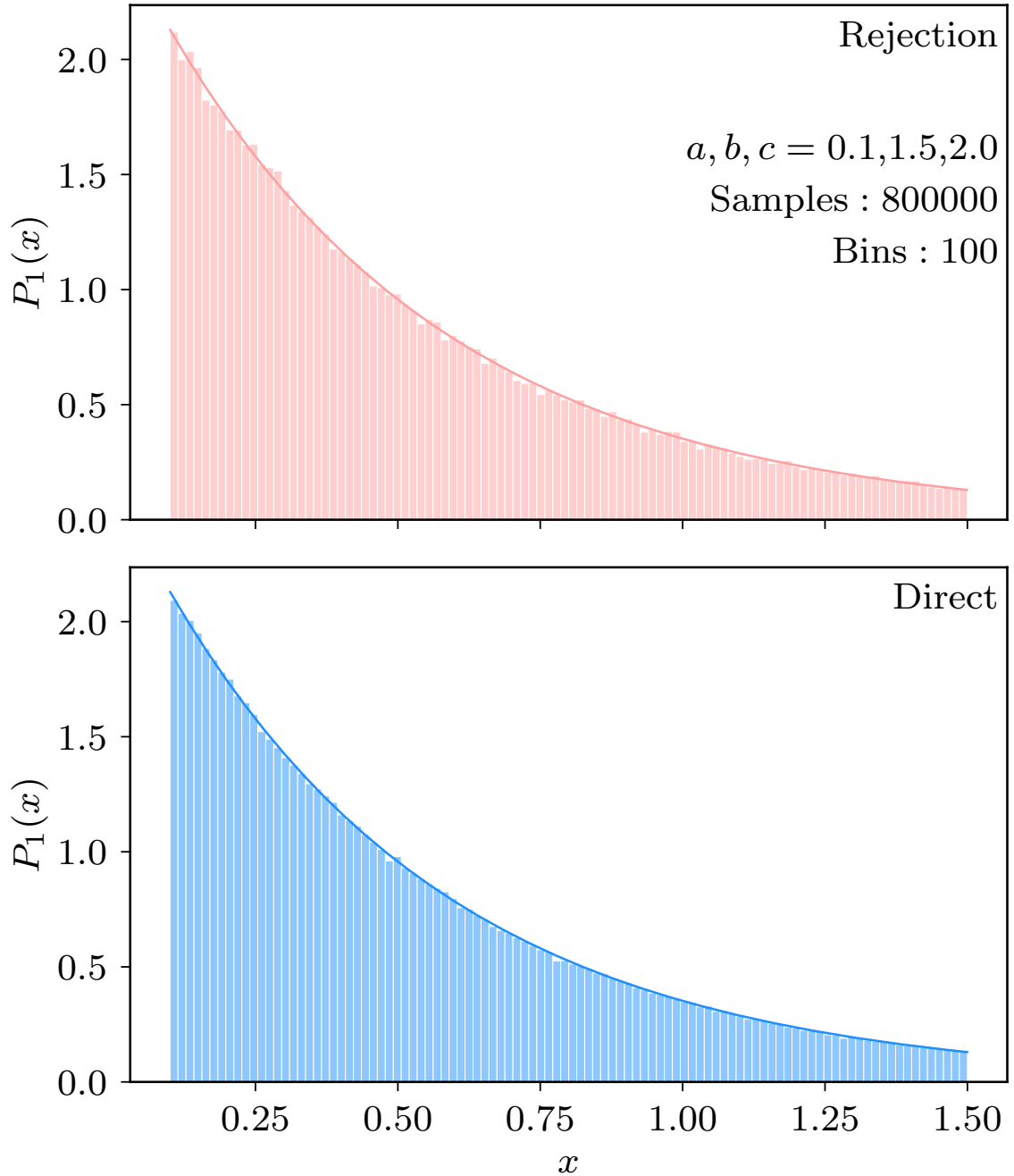


**Figure 5.1:** One dimensional truncated exponential distribution Eq. (5.1) generated via rejection sampling (top) and direct sampling (bottom). For the number of samples shown (800,000), both methods successfully generate the desired one dimensional truncated exponential distribution of the random variate  $x$ . The direct sampling data is closer to the exact distribution (solid curve) because it includes more good samples.

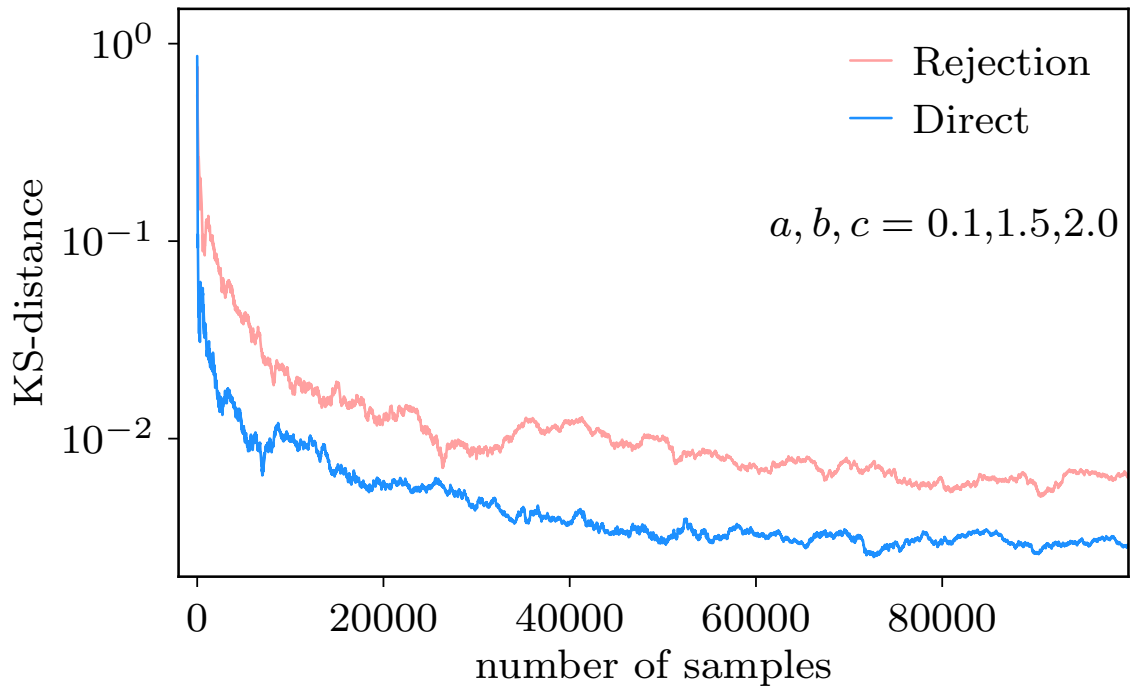


**Figure 5.2:** Kolmogorov-Smirnov (KS) test results. The KS-distance is plotted as a function of number of samples for two sampling methods. The KS-distance is smaller for the direct sampling dataset, which indicates that it better estimates the true one dimensional truncated exponential distribution, Eq. (5.1).

Having reviewed the standard methods of direct inversion and rejection sampling for the  $1D$  truncated exponential distribution, we now generalize to the  $2D$  case which is relevant for Path Integral quantum Monte Carlo simulations.

### 5.3 Direct sampling of $2D$ truncated exponential distribution

The probability distribution Eq. (5.1) can be generalized to two random variables  $x_1, x_2$  as:

$$P_2(x_1, x_2) = \frac{1}{\mathcal{Z}_J} e^{-c(x_2 - x_1)}, \quad (5.4)$$

where  $a \leq x_1 < x_2 \leq b$  and the distribution is normalized by:

$$\mathcal{Z}_J = \frac{e^{-c(b-a)} - ac + bc - 1}{c^2}. \quad (5.5)$$

The random variables  $x_1$  and  $x_2$  can be sampled sequentially by decomposing Eq. (5.4) into a product of marginal and conditional probabilities

$$P_2(x_1, x_2) = P_2(x_1)P_2(x_2|x_1), \quad (5.6)$$

where

$$P_2(x_1) = \int_{x_1}^b dx_2 P_2(x_1, x_2) = \frac{1 - e^{-c(b-x_1)}}{c\mathcal{Z}_J} \quad (5.7)$$

and  $P_2(x_2|x_1)$  is a one dimensional truncated exponential distribution in the variable  $x_2 \in [x_1, b]$ .

The CDF of the marginalized distribution is

$$\begin{aligned} F_2(x_1) &= \int_a^{x_1} dx'_1 P_2(x'_1) \\ &= \frac{1}{c^2 \mathcal{Z}_J} [e^{-c(b-a)} - e^{-c(b-x_1)} - c(a - x_1)]. \end{aligned} \quad (5.8)$$

Denote  $y = F_2(x_1)$ . To generate samples from the marginalized distribution  $x_1 \sim P_2(x_1)$ , one can sample  $y \sim U(0, 1)$  uniformly and then calculate  $x_1$  by inverting  $F_2$ :

$$x_1 = F_2^{-1}(y). \quad (5.9)$$

An analytic solution for  $x_1$  is possible in terms of the Lambert (product log) functions [164], which are defined to invert the functional dependence  $f(\alpha) = \alpha e^\alpha$ . Since this map is not injective, its inverse

$$W_k(\alpha e^\alpha) = \alpha, \quad (5.10)$$

has multiple solution branches  $k$ . When  $\alpha$  is real there are two solution branches; these are conventionally labeled  $k = 0$  for  $\alpha \geq -1$ , and  $k = -1$  for  $\alpha \leq -1$ .

Now we will perform a series of algebraic manipulations on Eq. (5.9). Begin by defining  $B = -e^{-cb}$ , and transform the dependent variable  $y$  to a new one,

$$u = yc^2 Z_J + Be^{ca} + ca. \quad (5.11)$$

Referring to Eq. (5.8), this yields the simplified constraint equation,

$$u = Be^{cx_1} + cx_1, \quad (5.12)$$

or equivalently,

$$(u - cx_1)e^{(u-cx_1)} = Be^u. \quad (5.13)$$

Next, apply  $W_k$  to both sides and use Eq. (5.10) with  $\alpha = u - cx_1$ . The result is,

$$x_1 = \frac{1}{c} [u - W_k(Be^u)]. \quad (5.14)$$

Using Eq. (5.12), we may write  $\alpha = -\exp[-c(b - x_1)]$ . Since  $b - x_1 > 0$ , the condition  $\alpha \geq -1$  coincides with  $c \geq 0$ . It follows that we should select:

$$k = 0 \text{ if } c \geq 0, \quad \text{or} \quad k = -1 \text{ if } c \leq 0. \quad (5.15)$$

Substitution of Eq. (5.11) into the right of Eq. (5.14) then gives our final closed form solution for  $x_1(y)$ . Note that the limit  $c \rightarrow 0$  is a removable singularity, for which  $x_1 \rightarrow b - (b - a)\sqrt{1 - y}$ .

Our final procedure for sampling both  $(x_1, x_2)$  from the joint distribution  $P_2(x_1, x_2)$  can now be summarized as follows. Begin by generating a uniform random sample  $y \sim U(0, 1)$ . Next, use the analytical solution of Eq. (5.14) with Eq. (5.11) to generate a sample  $x_1 \sim P_2(x_1)$ , where  $x_2$  has been marginalized out. Here, one may use an existing numerical subroutine to efficiently evaluate the Lambert function,  $W_0$  or  $W_{-1}$  [165]. With  $x_1$  fixed, the second random variate,  $x_2 \sim P_2(x_2|x_1)$ , can be directly sampled from the one dimensional truncated exponential distribution, Eq. (5.1), with the lower bound set to  $a \rightarrow x_1$  and keeping the upper bound as  $b$ .

Fig. 5.3 shows results for samples drawn from the two dimensional probability distribution  $P_2(x_1, x_2)$ , Eq. (5.4), for a fixed set of parameters  $a, b$ , and  $c$ . The leftmost heatmap shows the exact probability distribution  $P_2(x_1, x_2)$  for comparison with the results obtained from rejection and direct sampling for  $8 \times 10^5$  random samples of  $x_1$  and  $x_2$  each. For a dataset of this size, both methods sample the exact distribution well. Looking at the relative error heatmaps corresponding to each sampling method, most regions are within 10% of the exact distribution, with some areas in the top left having larger error due to the low sampling probability of this region.

Due to the similarity between the rejection and direct sampling results in Fig. 5.3, it is not straightforward to determine directly which method is more efficient in reproducing the two dimensional truncated exponential distribution, Eq. (5.4). Kolmogorov-Smirnov tests in higher dimensions have been proposed [166, 167], but



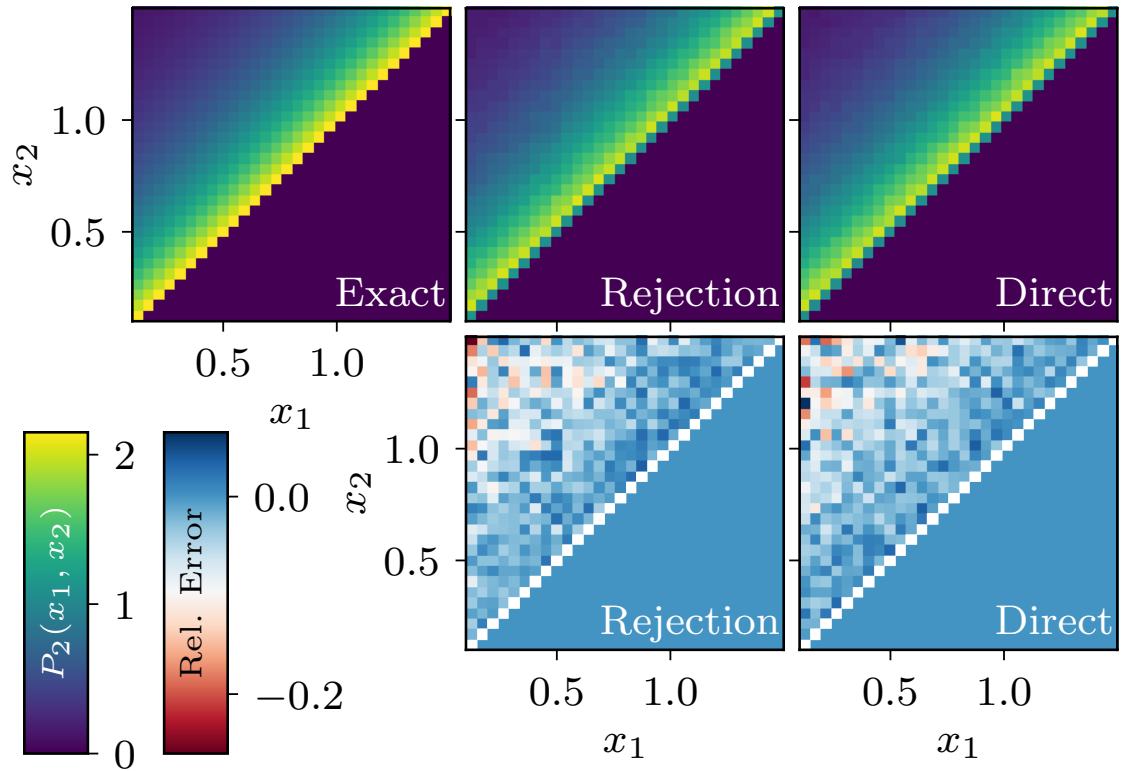


**Figure 5.3:** Two dimensional truncated exponential distributions, Eq. (5.4), generated via rejection and direct sampling. The heatmaps on the top row show the exact, rejection sampled, and directly sampled distributions for parameters  $a = 0.1$ ,  $b = 1.5$  and  $c = 2.0$ , with the relative error of each method compared to the exact shown in the bottom row.  $8 \times 10^5$  samples of  $x_1$  and  $x_2$  each were used.

technical issues make them highly non-trivial to implement, so we opt to compute running averages for the three quantities  $\langle x_1 \rangle$ ,  $\langle x_2 \rangle$ , and  $\langle x_1 x_2 \rangle$  as a function of number of samples, with the results shown in Fig. 5.4. For all three quantities, the running average of the samples obtained via direct sampling converges faster to the exact values (obtained using Eq. (5.4), denoted by the horizontal line), than the rejection sampling dataset.

In the next section, we show how sampling random variates from truncated exponential distributions, in both one and two dimensions, can improve the efficiency of some Quantum Monte Carlo simulations by reducing autocorrelation times between the samples.

## 5.4 Application: Lattice Path Integral Quantum Monte Carlo

Markov chain Monte Carlo applications based on the Metropolis-Hastings algorithms create a Markov chain from configurations drawn according to a probability density function  $\pi(\nu) = W(\nu)/\mathcal{Z}$ , where  $\nu$  denotes a configuration defined by the problem space. Stochastic transition probabilities  $T(\nu \rightarrow \nu')$  from a configuration  $\nu$  to a new configuration  $\nu'$  should be independent of the history of the random walk. This is achieved via an ergodic set of Monte Carlo updates that satisfy the principle of detailed balance:  $\pi(\nu)T(\nu \rightarrow \nu') = \pi(\nu')T(\nu' \rightarrow \nu)$ . Transition probabilities can be factored into a product of a selection probability  $P(\nu \rightarrow \nu')$  and an acceptance probability  $A(\nu \rightarrow \nu')$ . From the principle of detailed balance, the acceptance ratio of a general Monte Carlo update can be expressed as:

$$\frac{A(\nu \rightarrow \nu')}{A(\nu' \rightarrow \nu)} = \frac{W(\nu')P(\nu' \rightarrow \nu)}{W(\nu)P(\nu \rightarrow \nu')} \equiv R. \quad (5.16)$$

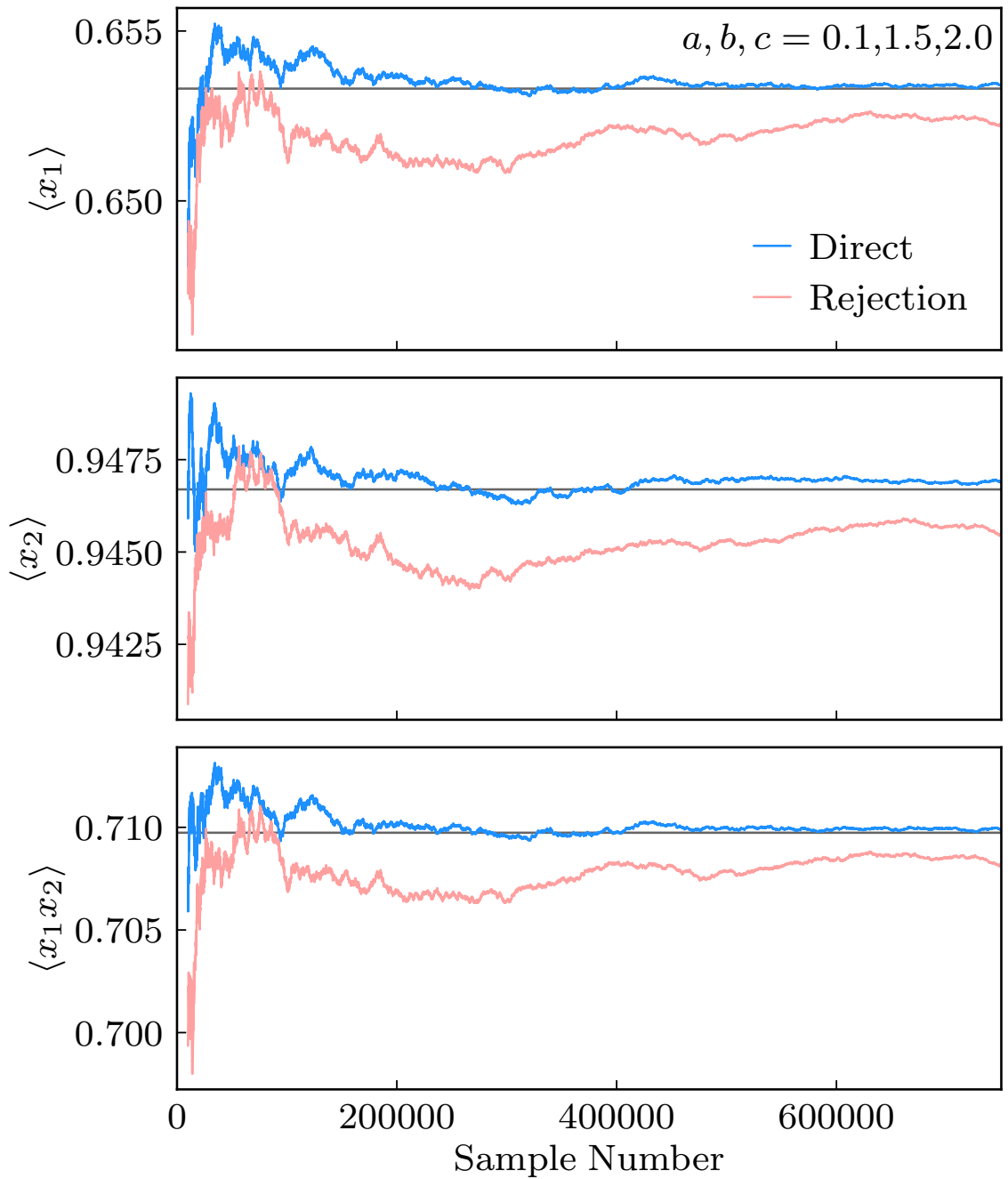


**Figure 5.4:** Cumulative average of  $\langle x_1 \rangle$ ,  $\langle x_2 \rangle$ , and  $\langle x_1 x_2 \rangle$  as a function of number of samples. The values of  $x_1$  and  $x_2$  have been sampled from the two dimensional truncated exponential distribution, Eq. (5.4), via rejection sampling and direct sampling. For all three averages, the dataset obtained via direct sampling converges faster to the exact result (horizontal line).

The  $M$  configurations generated via the MCMC process can be utilized to approximate expectation values of observables:

$$\langle O \rangle = \sum_{\nu} O(\nu) \pi(\nu) \simeq \frac{1}{M} \sum_{i=1}^M O_i, \quad (5.17)$$

where  $O_i = O(\nu_i)$ . In practice, random samples  $\nu \sim \pi(\nu)$  making up the finite Markov chain  $\{\nu_1, \dots, \nu_M\}$  may not be independent, leading to correlations in  $O_i$  and  $O_j$ , i.e.  $\langle O_i O_j \rangle \neq \langle O_i \rangle \langle O_j \rangle$ . This can be quantified for observable  $O$  via the integrated autocorrelation time  $\mathcal{T}_O$ :

$$\mathcal{T}_O = 1 + 2 \sum_{\tau=1}^M \frac{\mathcal{C}_O(\tau)}{\mathcal{C}_O(0)}, \quad (5.18)$$

where the autocorrelation function is defined to be

$$\mathcal{C}_O(\tau) = \frac{1}{M - \tau} \sum_{i=1}^{M-\tau} (O_i - \langle O \rangle)(O_{i+\tau} - \langle O \rangle). \quad (5.19)$$

Thus, truly independent measurements can only be performed for samples separated by  $\mathcal{T}_O$  MCMC steps, and any algorithmic improvement leading to a reduction in  $\mathcal{T}_O$  will improve the overall efficiency of a simulation.

In Chapters 2 and 3, we introduced a path integral Monte Carlo algorithm for the simulation of bosonic lattice models at zero temperature ( $T = 0$ ), inspired by the finite temperature PIMC Worm Algorithm [57]. We direct the reader to these for complete details of the algorithm which can be used to evaluate ground state expectation values:

$$\langle O \rangle \equiv \frac{\langle \Psi | O | \Psi \rangle}{\langle \Psi | \Psi \rangle} \quad (5.20)$$

by projection of a trial state  $|\Psi_T\rangle$ , with a large power of the density operator:  $|\Psi\rangle = \lim_{\beta \rightarrow \infty} e^{-\beta H} |\Psi_T\rangle$ , where  $H$  is the system Hamiltonian, and  $\beta$  is the projection length.

Using the path integral formulation of quantum mechanics, the target configuration space can be represented as a set of paths, known as worldlines, that propagate in imaginary time (characterized by  $\beta$ ) and space. An example configuration of

worldlines for a Bose-Hubbard lattice in one dimension with  $N = 2$  bosons on  $L = 4$  sites is shown in Fig. 5.5. The vertical direction represents imaginary time and the lattice sites span the horizontal direction. In this diagram, line widths are proportional to number of particles on a site, with dotted lines representing an empty site. The set of imaginary times  $\{\tau_i\}$  labeled on the left side of the figure correspond to times at which the Fock state  $(|n_1, n_2, n_3, n_4\rangle)$  has changed (right side), where  $n_j$  counts the number of particles on site  $j$ . Local changes in occupation can occur via either kinks representing particle hops between adjacent sites, or via the insertion or deletion of a special type of truncated worldline known as a worm [58, 61, 89, 92]. Formally, the worm tail and head represent bosonic creation and annihilation operators, respectively. The entire configuration space can be sampled by performing updates on the worm.

The acceptance ratio for the insertion of a worm into the worldline configuration has the form:

$$R = \text{const} \times \frac{1}{P(\tau_h, \tau_t)} \times e^{-c(\tau_h - \tau_t)} \quad (a \leq \tau_t < \tau_h \leq b), \quad (5.21)$$

where  $\tau_t$  and  $\tau_h$  denote the imaginary times of the worm tail and head, respectively, and are randomly sampled from a joint probability distribution,  $P(\tau_h, \tau_t)$ . By choosing this distribution to be the two dimensional truncated exponential distribution, Eq. (5.4), the exponential factor in Eq. (5.21) cancels, leaving just a constant factor as the acceptance ratio:

$$R = \text{const} \times \frac{1}{e^{-c(\tau_h - \tau_t)}} \times e^{-c(\tau_h - \tau_t)} = \text{const}, \quad (5.22)$$

where the normalization constant of the two dimensional truncated exponential from which  $\tau_t, \tau_h$  are drawn has been absorbed into const. We expect that this constant acceptance ratio can be further optimized by implementing a pre-equilibration stage that tunes simulation parameters via iterative methods, similarly to approaches for

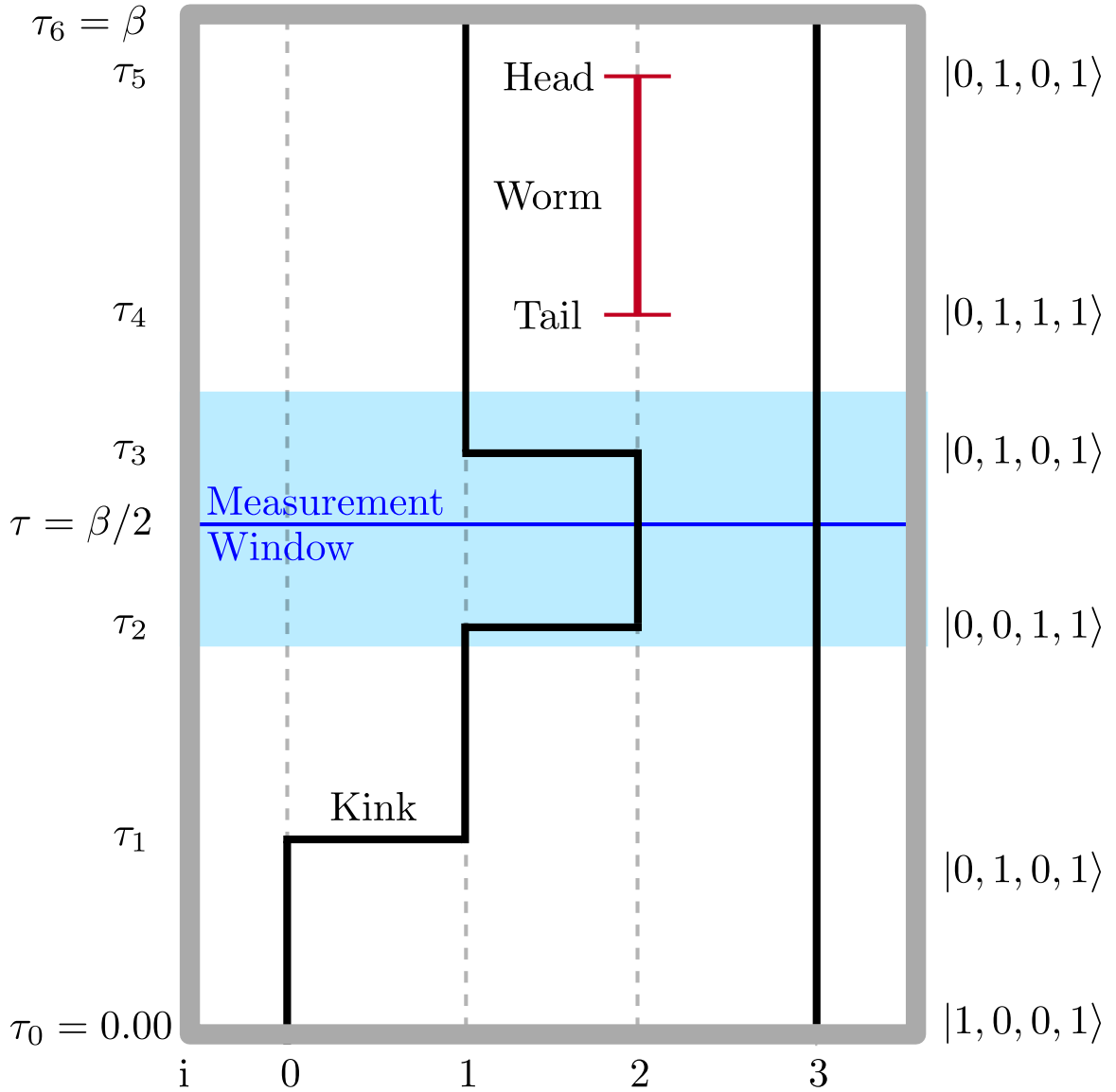


**Figure 5.5:** Example of a worldline configuration in Path Integral Monte Carlo for 2 particles on 4 lattice sites. The paths propagate in the direction of imaginary time (vertical) and space (horizontal). Three kinks are shown at imaginary times  $\tau_1, \tau_2, \tau_3$  and occur due to a particle hopping between adjacent sites. More configurations can be sampled by performing updates on the worm shown with tail at  $\tau_4$  and head at  $\tau_5$ . Some estimators, like the kinetic energy, involve averaging a quantity, such as the number of kinks, over a window of user defined width centered around  $\tau = \beta/2$ .

the tuning of the chemical potential,  $\mu$ , to set the average number of particles [101, 168]. The acceptance ratios of the rest of the updates, which are related to either insertions and deletions of kinks or shifting worm ends in the imaginary direction, can also be reduced to a constant by sampling imaginary times from the one dimensional truncated exponential distribution, Eq. (5.1). For updates that shift worm ends in the imaginary time direction, sampling from this distribution actually leads to perfect direct sampling [1, 57] ( $R = 1$ ).

In the discussion that follows, results for which imaginary times have been sampled from a truncated exponential distribution, such that the acceptance ratios take the form of Eq. (5.22), will be referred to as *direct* sampling. The conventional *rejection* scheme instead involves sampling each of the imaginary times from a rescaled uniform distribution,  $\tau \sim U(a, b)$ , where  $a, b$  are the lower and upper bounds of the interval. Thus, the joint probability distribution for this case is  $P(\tau_h, \tau_t) = 1/(b-a)^2$ . However, both schemes still involve a Metropolis sampling step in which updates will be accepted by comparing if a random number,  $r \sim U(0, 1)$ , satisfies  $r < R$ , and rejected otherwise. Formally, the sampled distribution is the same using both schemes, up to a pre-factor.

We benchmark the proposed direct sampling approach on a ground state quantum Monte Carlo simulation of the Bose-Hubbard model for itinerant bosons on a lattice [23]:

$$H = -t \sum_{\langle i,j \rangle} b_i^\dagger b_j + \frac{U}{2} \sum_i n_i(n_i - 1) - \mu \sum_i n_i, \quad (5.23)$$

where  $t$  is the tunneling between neighboring lattice sites  $\langle i, j \rangle$ ,  $U > 0$  is a repulsive interaction potential,  $\mu$  is the chemical potential, and  $b_i^\dagger(b_i)$  are bosonic creation(annihilation) operators on site  $i$ , satisfying the commutation relation:  $[b_i, b_j^\dagger] = \delta_{i,j}$ , with  $n_i = b_i^\dagger b_i$  the local number operator. Simulations were performed in the canonical ensemble, in which  $\mu$  is a simulation parameter. This model exhibits a quantum phase transition from a superfluid, at low interactions, to a Mott insulator, at strong repulsive interactions, where bosons become highly localized. The accurate

determination of the quantum critical point has motivated much research [24–39] and, below, we report on simulations at a fixed interaction strength of  $U/t = 3.3$ , which is representative of the quantum critical regime where both spatial and temporal correlation lengths diverge, causing the well known problem of critical slowing down [169] where correlations between MCMC samples can be large.

The kinetic energy estimator is non-diagonal in the Fock basis and is determined from the average number of kinks in the measurement window of Fig. 5.5 [1]:

$$\langle K \rangle = -\frac{\langle N_{\text{kinks}} \rangle}{\Delta\beta} \quad (5.24)$$

where  $\Delta\beta$  is the window width. The potential energy estimator is diagonal in the Fock basis and is obtained by measuring

$$\langle V \rangle = \frac{U}{2} \sum_i \langle n_i(n_i - 1) \rangle \quad (5.25)$$

at imaginary time  $\tau = \beta/2$ .

To understand the role of direct vs. rejection sampling in our quantum Monte Carlo algorithm, we performed simulations of the one dimensional Bose-Hubbard model at unit-filling,  $L = N$ , with  $L$  the number of sites and  $N$  the number of particles, for different values of  $L$  and computed the integrated autocorrelation time in Eq. (5.18) using both sampling methods at  $U/t = 3.3$ , near the superfluid-insulating critical point. The results are shown in Fig. 5.6 where the autocorrelation times were computed using the emcee Python library [170], which is based on the methods described in Refs. [171, 172]. For system sizes up to  $L = 2^6 = 64$ , the autocorrelation time for both the kinetic and potential energy was lower for the case in which imaginary times were directly sampled from truncated exponential distributions when performing worm updates. The insets show the ratio of autocorrelation times sampling from truncated exponential distributions (direct) over autocorrelation times sampling from uniform distributions (rejection),  $\mathcal{T}^D/\mathcal{T}^R$ , as a function of system size.



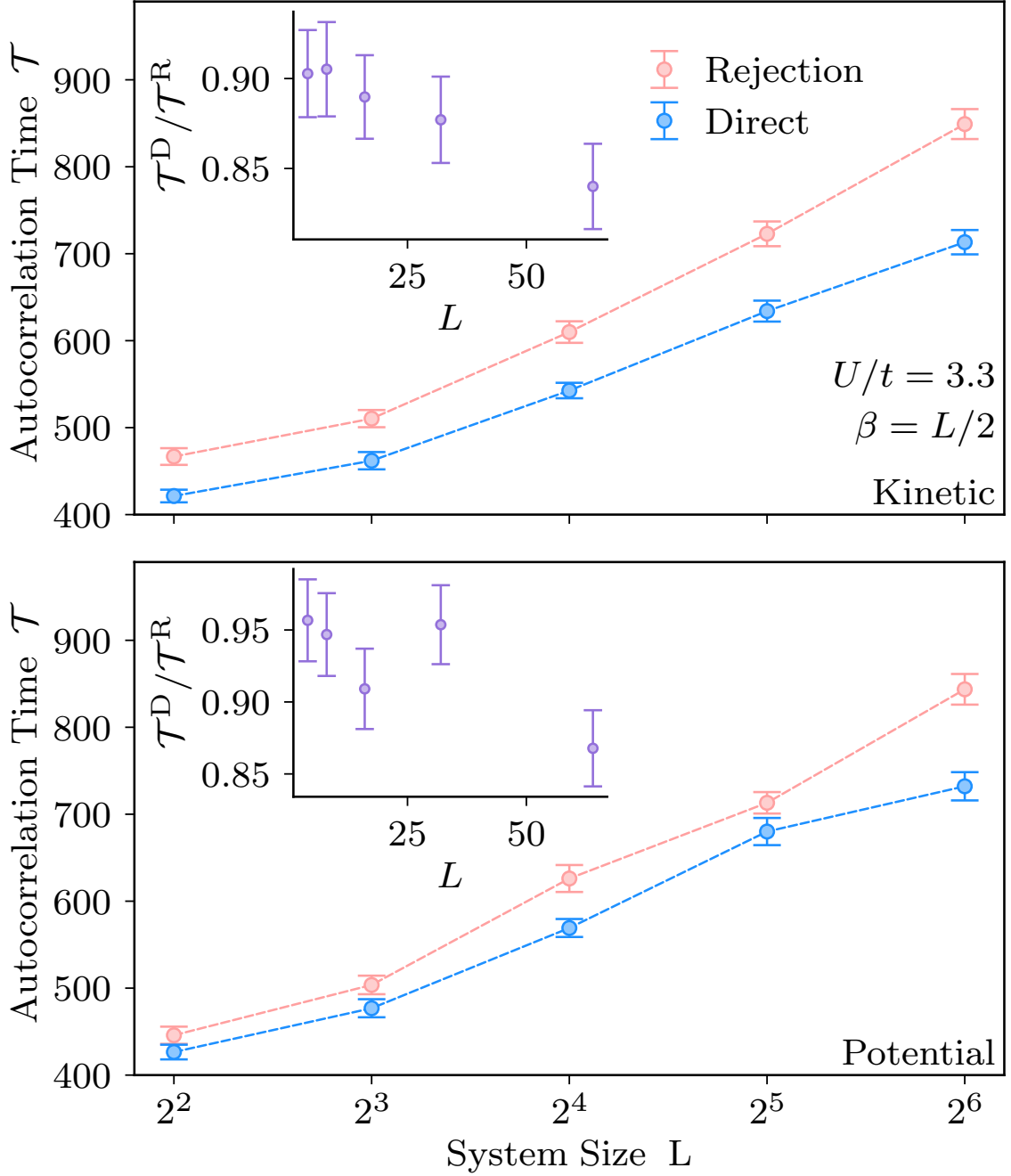


**Figure 5.6:** Integrated autocorrelation times for the ground state kinetic (top) and potential (bottom) energy estimators of the one dimensional Bose-Hubbard model obtained via path integral Monte Carlo as a function of system size,  $L$  at unit filling:  $L = N$ . Lower is better. The insets show the ratio of autocorrelation times obtained by sampling using direct and rejection (uniform distribution) methods for the one and two dimensional truncated exponential distributions.

A ratio less than unity indicates a decrease in correlations amongst samples, and improvements of  $\sim 15\%$  are observed for the largest system sizes studied.

Direct sampling has a larger effect on the autocorrelation time of the kinetic energy estimator as the simulation dynamics of the average number of kinks is directly related to improved worm dynamics in the simulation (see Fig. 5.5). Error bars represent the standard error of the mean autocorrelation time computed from 80 independent simulations.

Since the lattice ground state PIMC algorithm described in Ref. [1] is a projection algorithm, it is subject to a systematic error that decreases with increasing projection length,  $\beta$ . Due to this, reliable estimates of observables are obtained by performing simulations for various values of  $\beta$ , and extrapolating the exact value, within error bars, from an exponential fit in  $\beta$  plus an additive constant:  $\langle O(\beta) \rangle = C_1 e^{-\beta C_2} + \langle O \rangle$ , where  $C_1, C_2$ , and  $\langle O \rangle$  are fitting parameters. Thus, to understand the role of direct sampling on the  $\beta$  extrapolation, we plot  $\beta$  dependent autocorrelation times for the kinetic and potential energies for a fixed system size  $L = 12$  and  $U/t = 3.3$  in Fig. 5.7. The autocorrelation times are once again seen to improve by sampling imaginary times directly from truncated exponential distributions, with the insets showing time reductions of approximately 20% for the largest  $\beta$  values.

The above results demonstrate that sampling directly from truncated exponential distributions results in decreased autocorrelation times for estimators in the algorithm presented in [1]. However, for our implementation of the algorithm, it was also seen that wall clock times in the direct sampling of truncated exponential distributions were no slower than the original version, where imaginary times were sampled from uniform distributions. In other words, the direct sampling scheme can be implemented without impacting practical run times. For a system of  $L = N = 12$  bosons at  $U/t = 3.3$  and  $\beta = 16$ , we performed 10 simulations, each starting from different random seeds, and observe that the fraction of wall clock times using both sampling schemes was  $t^D/t^R = 1.02 + / - 0.01$ . The fraction of wall times for each seed, for the direct over rejection methods,  $t^D/t^R$ , are shown in Fig. 5.8. The new sampling

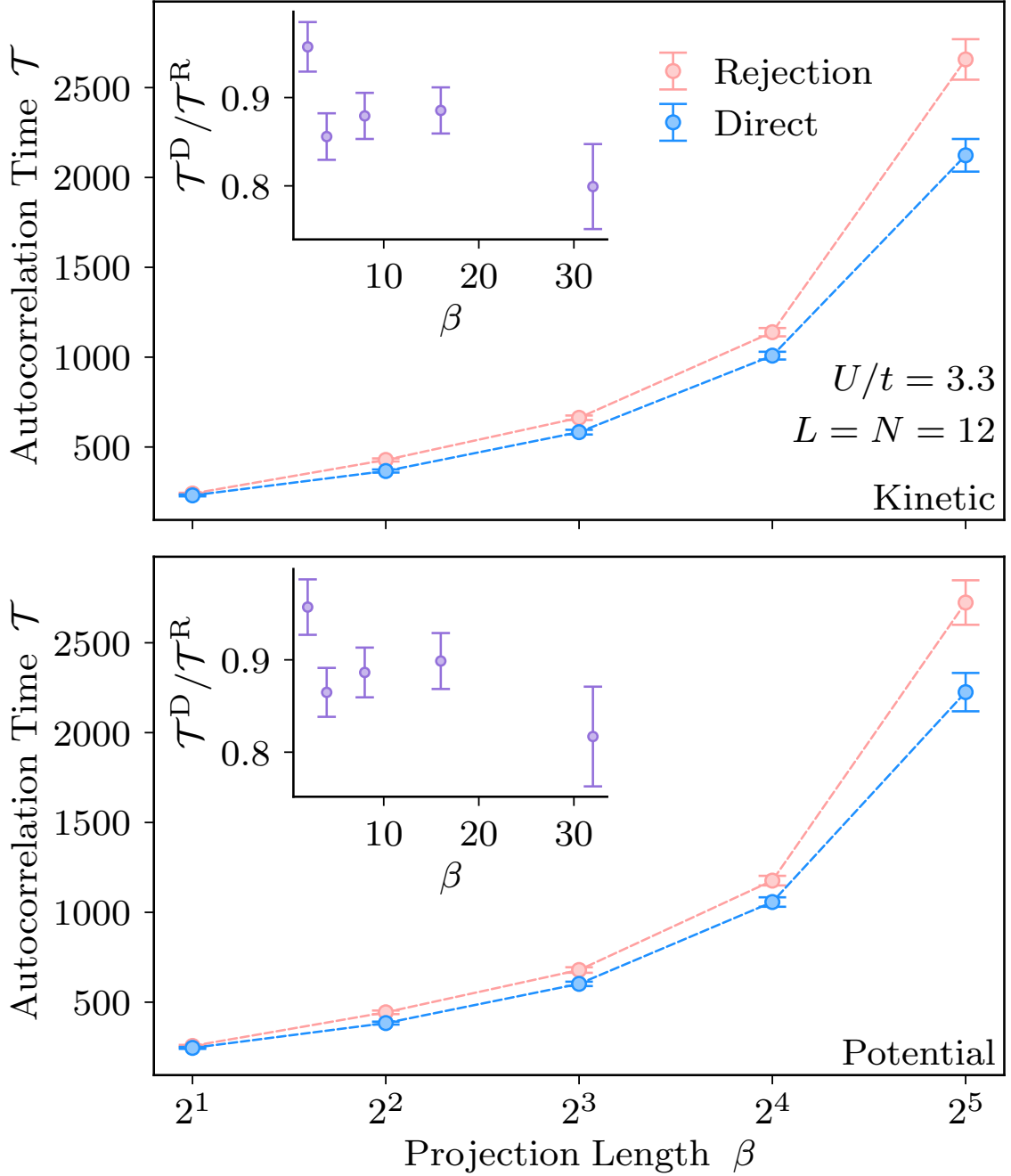


**Figure 5.7:** Autocorrelation times for the ground state kinetic (top) and potential (bottom) energy estimators of the one dimensional Bose-Hubbard Model obtained via Path Integral Monte Carlo as a function of projection length,  $\beta$ . Lower is better. The insets show the ratio of autocorrelation times obtained by sampling using direct and rejection (uniform distribution) methods for the one and two dimensional truncated exponential distributions.

scheme has thus successfully reduced autocorrelation times without slower wall times, resulting in an effective speedup of the quantum Monte Carlo application discussed.

All code, scripts and data needed to confirm the results presented in this section are available in open source repositories [80, 82, 84].

## 5.5 Conclusions

In this chapter, we have shown how to directly obtain random variates from two dimensional truncated exponential distributions via a two step inverse sampling method. The dataset of random variates obtained directly from truncated exponential distributions, in both one and two dimensions, better reproduced the target distribution for a finite number of samples. Direct sampling of the truncated exponential distribution was then applied to lattice path integral Monte Carlo, where this distribution appears in the acceptance probability of *worm* updates and enabled the efficient sampling of the imaginary time worldline configuration space. The direct sampling approach leads to reduced integrated autocorrelation times for the kinetic and potential energy estimators, while keeping the simulation wall times practically the same between both sampling schemes. For the system sizes considered, overall efficiency gains of 15% are identified.

Future avenues for research include implementing iterative methods to optimize non-physical algorithmic parameters that appear in the now constant worm update acceptance ratio to further improve dynamics and approach the ideal sampling limit.

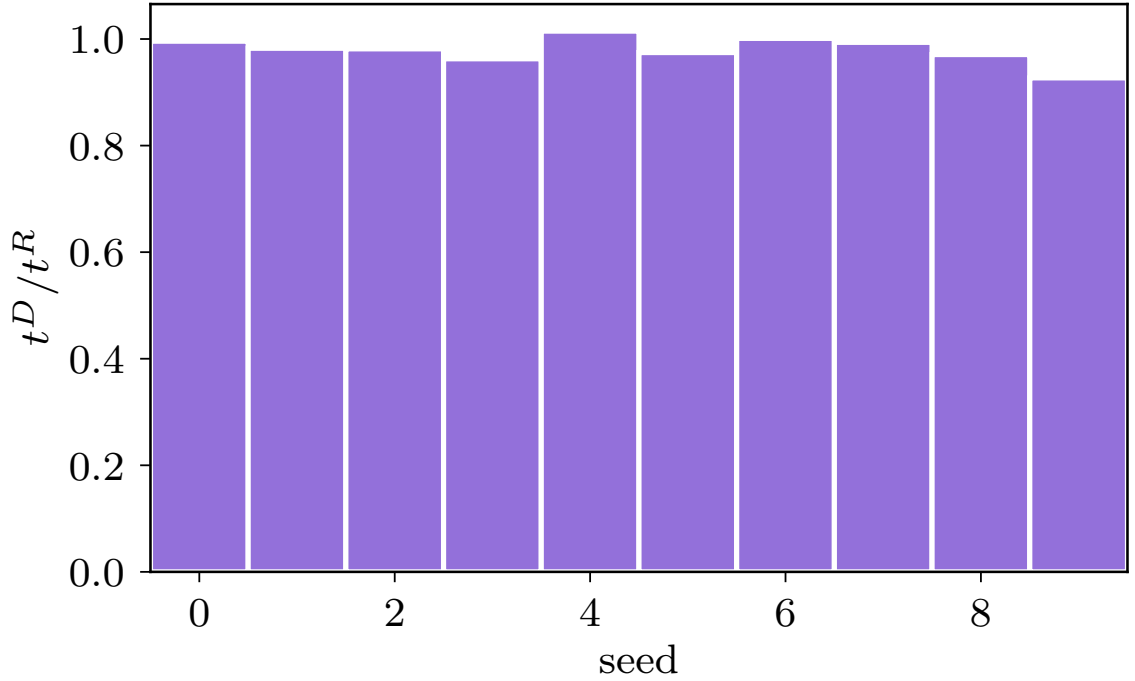


**Figure 5.8:** Wall clock times for path integral Monte Carlo simulations for a 1D Bose-Hubbard lattice of size  $L = N = 12$  at  $U/t = 3.3$  using rejection (R) and direct (D) sampling of the truncated exponential distribution. Results are shown for 10 independent runs for each method starting from different random seeds and  $10^6$  samples of the kinetic and potential energies were collected. The wall times did not change significantly when using different sampling schemes, with an average ratio of wall times  $t^D/t^R = 1.02 + / - 0.01$ .

# Chapter 6

## Discussion and Future Work

In this thesis, a novel lattice Path Integral Monte Carlo algorithm that is sign problem free for bosonic models at zero temperature has been introduced.

After introducing some of the inspiration that led us to pursue this research project in chapter 1, we developed the path-integral formalism underlying our PIGSFLI algorithm in chapter 2. Our derivation of the propagator and configurational weights in the path-integral formalism differed from existing, finite temperature derivations, in that at  $T = 0$ , the imaginary time direction is not subject to periodic boundary conditions, where worldlines wrap around a toroidal topology. Instead, our worldlines wrap around the surface of an infinitely-long  $\beta$ -cylinder. Due to the breaking of imaginary time translational invariance, it was seen that additional Monte Carlo updates had to be added to satisfy ergodicity. These updates consisted in inserting and deleting worm ends (i.e, bosonic creation or annihilation operators) near the ends of the  $\beta$ -cylinder, at  $\tau = 0$  and  $\tau = \beta$ . Implementing these new  $T = 0$  updates, alongside the original set of  $T > 0$  updates, was enough to satisfy ergodicity in our algorithm such that conventional estimators, such as the kinetic and potential ground state energies, can be sampled. We performed benchmarks of both of these quantities, where PIMC estimates were compared to exact diagonalization values (ED), resulting in relative errors of  $10^{-2}$  at worst, and as small as  $10^{-4}$ . These errors can be made

arbitrarily small by a combination of increasing the simulation time, increasing the projection length,  $\beta$ , and by choosing better trial wavefunctions.

After a successful implementation of PIGSFLI in single-replica spaces, we extended the algorithm to work in a replicated configuration space consisting of two copies of the system. The idea of this extension was to compute Rényi entanglement entropies. We derived path-integral estimators for the: 1) second Rényi entanglement entropy, 2) accessible entanglement, and 3) symmetry-resolved entanglement entropies. These three quantities were benchmarked by comparing with exact values from ED and excellent agreement was seen at interaction strengths representative of the superfluid phase, near the quantum critical point, and in the Mott insulating phase. For all estimators, it was seen that converging to the exact result in the superfluid phase required simulations at large values of the projection length,  $\beta$ , due to this phase being gapless. On the other hand, the Mott insulating phase only needed small  $\beta$  values for the estimators to converge to their exact value, since the energy gap allows for faster projection of the exact ground state when acting with a power of the density operator on the trial state.

Access to large system sizes also allowed us to generate a set of results that have never been seen before. For a  $1d$  Bose-Hubbard system of  $L = 256$  particles at unit filling and under an equal spatial bipartition,  $\ell = L/2$ , we were able to explore the second Rényi EE as a function of interaction strength,  $U/t$ , across all phases of the Bose-Hubbard model. The results were similar to those obtained previously in an experiment [18] with optical lattices of  $L = 4$  Rb<sup>87</sup> atoms, where the entanglement vanished in the insulating phase due to the state being a product state, and increased as we move across the transition into the highly non-localized superfluid phase. We were also able to apply PIGSFLI to simulate a large system in  $2d$ . For a square lattice of  $32 \times 32 = 1024$  sites at unit filling, with an embedded square subregion of varying linear size  $\ell$ , and near criticality, we saw that the entanglement followed a boundary law and that sub-leading logarithmic corrections can be investigated to potentially obtain universal quantities, such as Goldstone modes. Nevertheless, due

to the contribution of sharp corners to the sub-leading logarithmic correction, the number of Goldstone modes could not be accurately determined for this geometry and system size. This can be a future avenue of study and the code admits other types of subregion geometry, such as a strip geometry, for which there are no corner effects and for which these universal numbers can be more accurately studied.

For a one dimensional system of  $L = 64$  bosons at unit filling near the critical point, we were able to use PIGSFLI to compute the symmetry-resolved entanglement as a function of local particle number sector. We saw that near criticality, the symmetry-resolved entanglement of the particle number sector where the underlying probability distribution is maximal, is not itself the maximal entanglement sector. This was explained by the onset of Mott insulating behavior, where the entanglement for the maximal sector vanishes, whereas the adjacent sectors (i.e,  $n_{\max} \pm 1$ ) have entanglement of  $\ln 2$ . This result was derived from analyzing the form of the ground state at large interaction strengths in these two sectors in terms of holon-doublon quasiparticle interactions across subregion boundaries.

After successfully extending the PIGSFLI algorithm to a two replica space where entanglement entropies can be estimated, in chapter 4 we developed and numerically confirmed subsystem scaling forms for the accessible and symmetry-resolved entanglement entropies in the  $1d$  Bose-Hubbard model. These scaling forms were obtained from previously known relationships between entanglement entropies and bipartite fluctuations of local particle number in a subregion. It was seen that the accessible entanglement and symmetry-resolved entanglement possess the same subsystem scaling ;  $S_2^{\text{acc}} \sim s_2(n) \sim c/4 \ln(D(\ell)) - 1/2 \ln \ln(D(\ell)/a_0)$ , up to  $\mathcal{O}(1)$  corrections. These scaling forms were numerically confirmed using PIGSFLI, for  $1d$  systems with Gaussian local particle number distribution, by calculating each entanglement measure as a function of the cordlength of the subsystem size. For a system of 64 bosons at unit filling both in the superfluid phase and near the superfluid-phase transition, the Monte Carlo data followed the scaling predictions. Using the obtained scaling forms, we were able to obtain physical quantities such as the central



charge underlying the CFT and the Luttinger parameter. For the symmetry-resolved entanglement entropy, it was seen that the subsystem scaling is independent of local particle number sector, a property known as *entropy equipartition* [78].

In chapter 5, a method for the direct sampling of two dimension truncated exponential distributions was introduced. By implementing this direct sampling into PIGSFLI, autocorrelations were reduced. The inspiration for this project came from the fact that the acceptance ratios of most Monte Carlo updates in our algorithm contained an exponential factor in one or two random imaginary times that could be cancelled by sampling these random variates instead from either  $1d$  or  $2d$  truncated exponential distributions. The new sampling resulted in acceptance ratios that now depended only on a constant that can be tuned in a pre-equilibration stage of the simulation, and could even be unity in some updates, resulting in perfect direct sampling. Although direct sampling of the  $1d$  truncated exponential distribution has been implemented previously in finite temperature lattice PIMC, our method to sample the  $2d$  case represents a new contribution to the method. The new sampling scheme resulted in a less correlated dataset, for which convergence of ground state energies to their exact values now required fewer samples than with rejection sampling. Our method did not affect the actual wall clock run time compared to the original, and thus an effective speed up was obtained of up to 20/% for the systems shown, a noticeable improvement for simulations that commonly run for days or even weeks. This project illustrates the importance of continuing algorithmic development so PIGSFLI can be employed for the simulation of larger systems and the measurement of estimators with higher statistical uncertainty, such as the accessible entanglement entropy.

Throughout this thesis, we have thus developed the theoretical framework and the computational implementation of lattice Path Integral Monte Carlo at  $T = 0$ . It was shown how this algorithm can be used to compute conventional estimators and also entanglement estimators in a replicated configuration space. This tool allowed us to numerically confirm new subsystem scaling forms for the accessible

and symmetry-resolved entanglement entropies. And finally, by implementing a new direct sampling method for the  $2d$  truncated exponential distribution, we showed how algorithmic development will be an essential element throughout the development cycle of the PIGSFLI algorithm for the simulation of even more complicated systems and estimators.

## 6.1 Future Work

In this section, we discuss some future avenues of research that we would like to pursue with the PIGSFLI algorithm.

### 6.1.1 Luttinger Parameter Estimation

The fluctuations in local particle number,  $n$ , in a subregion of a bipartite  $1d$  system, scale with subsystem size,  $\ell$ , as:

$$F(\ell) \equiv \langle n \rangle^2 - \langle n^2 \rangle \simeq \frac{K}{\pi^2} \ln \left( \frac{\ell}{a_0} \right), \quad (6.1)$$

where  $K$  is the Luttinger parameter and  $a_0$  is a short-distance cutoff. For systems with periodic boundary conditions,  $\ell$  is replaced by the cordlength,  $D(\ell) = L/\pi \sin(\pi\ell/L)$ , by replacing  $\ell \rightarrow D(\ell)$  to account for distances measured around a ring. These bipartite fluctuations are computationally inexpensive to obtain with various algorithms, such as DMRG and our own lattice PIGS. This has led to this quantity being used for accurate estimations of the Luttinger parameter and quantum critical points [39], and they have even been shown to be equivalent to an entanglement measure [76, 77]. Previous numerical studies of bipartite fluctuations rely on their computations via DMRG, for which  $1d$  Bose-Hubbard lattices of up to  $L = 512$  sites have been studied, for the case of open boundary conditions [39]. Our PIGSFLI algorithm can simulate these system sizes, with the added benefit that it can operate in not only the insulating phase, but also deep into the superfluid phase,

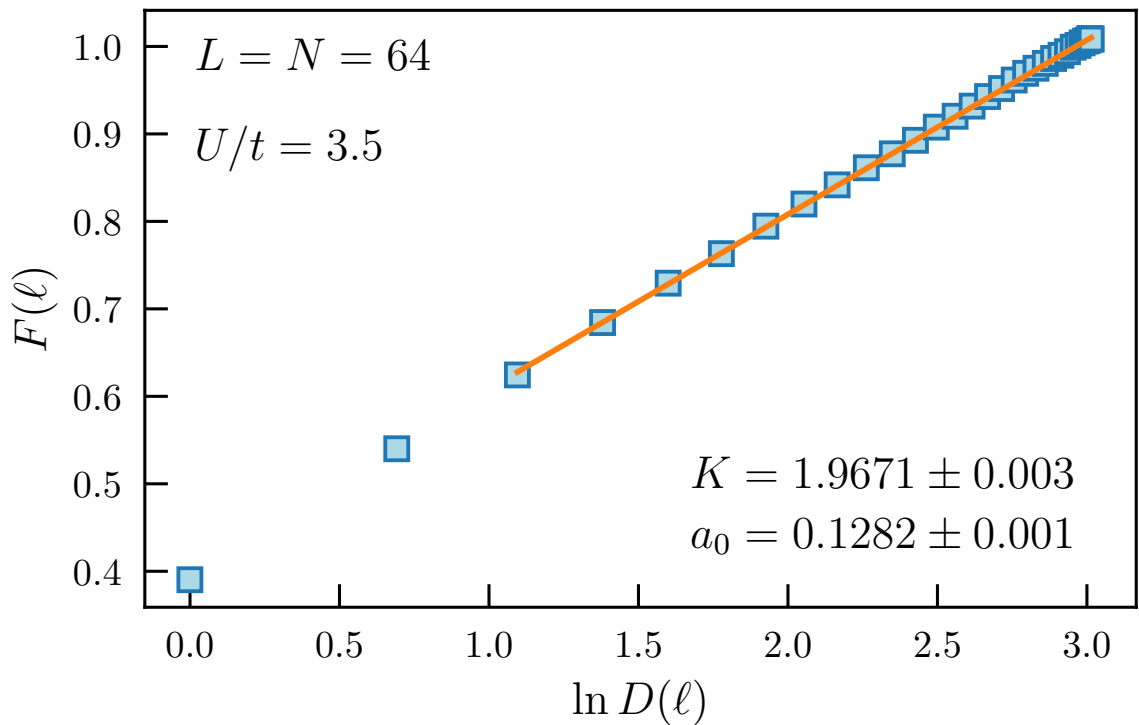
where large DMRG errors might occur due to weak interactions allowing large particle number fluctuations, and with a periodic boundary, for which DMRG also has higher error in large systems.

Fig. 6.1 shows the bipartite fluctuation scaling with cordlength in a subregion of a  $1d$  Bose-Hubbard chain of  $L = 64$  sites at unit filling with periodic boundary conditions at an interaction strength of  $U/t = 3.5$ . The data was obtained using PIGSFLI and has been fitted to Eq. (6.1), showing excellent agreement. The first two system sizes have been excluded from the fit in order to minimize finite size contributions. These finite size corrections are in and of itself a future avenue of research and have been previously computed for other  $1d$  models [76].

Note that the Luttinger parameter obtained for the system in Fig. 6.1,  $K = 1.967(3)$ , is slightly below the critical value expected from Luttinger Liquid theory,  $K_c = 2$ . This suggests that, up to finite size effects, the critical interaction strength is located at a value close to, albeit slightly lower than  $U/t = 3.5$ . In chapter 4, a value of  $U/t = 3.3$  was considered to be close enough to the superfluid-insulating transition, but the Luttinger parameter extracted in this case was  $K \approx 2.1$ . This suggests that the critical interaction strength should be at a larger value. With PIGSFLI, we plan to compute  $K$  from bipartite fluctuations in large systems to obtain a more accurate estimate of the superfluid-insulating transition.

### 6.1.2 Symmetry-resolved entanglement interaction dependence

In this thesis, we have studied the symmetry-resolved entanglement at fixed values of the interaction strength, representative of the superfluid phase, near the phase transition, and in the insulating phase. We have obtained functional forms for scaling with subsystem size and confirmed them numerically. Nevertheless, a study of the symmetry-resolved entanglement entropy as a function of interaction strength has not been performed yet. The PIGSFLI algorithm opens the door for the investigation of



**Figure 6.1:** Scaling of bipartite fluctuations with the log of the cordlength for a  $1d$  Bose-Hubbard chain of 64 bosons at unit filling, subject to periodic boundary conditions, and at interaction strength  $U/t = 3.5$ , near the phase transition. The extracted Luttinger parameter is close to the prediction from Luttinger Liquid theory near the critical point,  $K_c = 2$ . Finite size scaling analyses can be performed to extract a more accurate location of the superfluid-insulating phase transition.

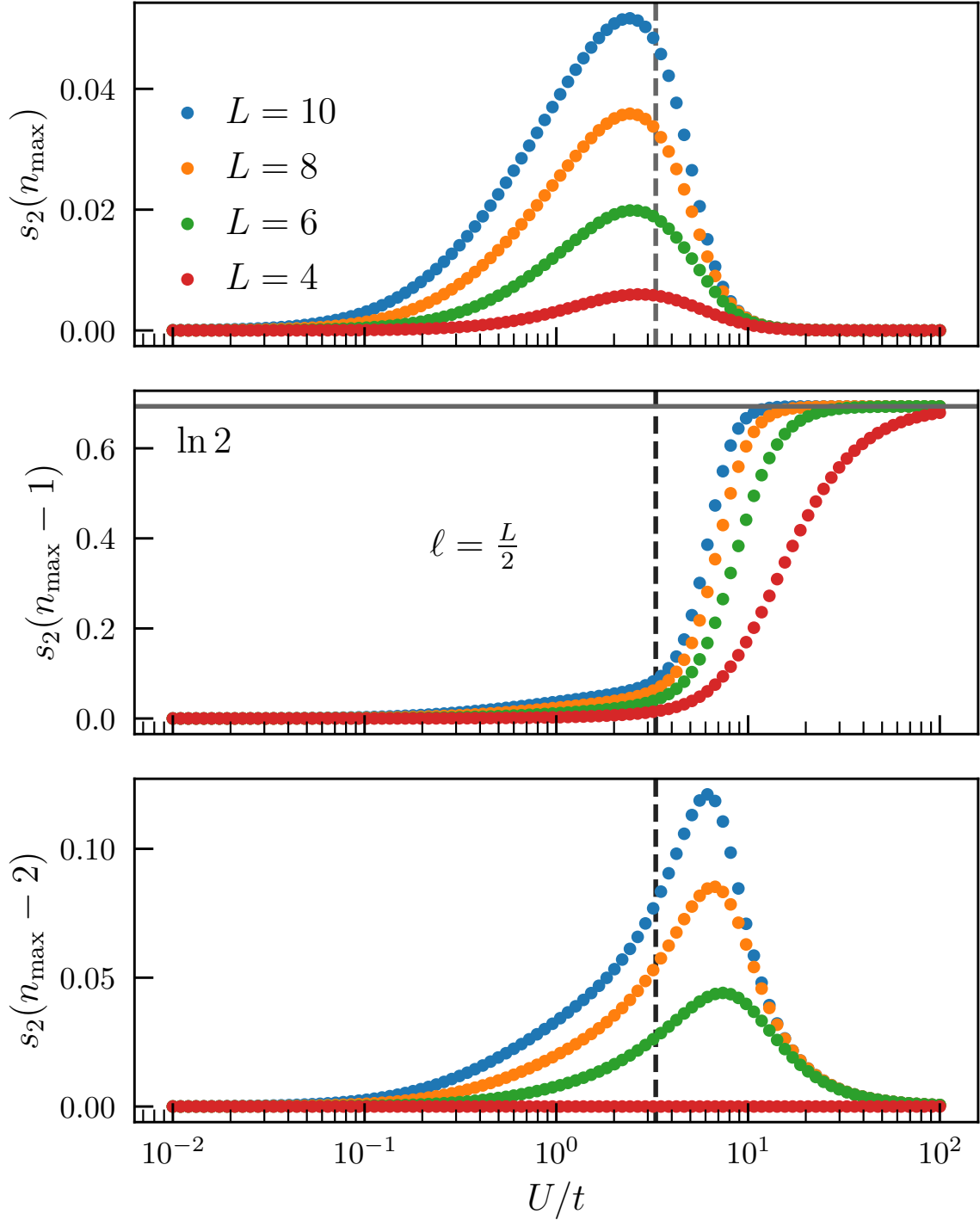
this interaction dependence for system sizes larger than what can be obtained with exact diagonalization and in the superfluid phase, where DMRG error is large.

Fig. 6.2 shows the symmetry-resolved entanglement as a function of interaction strength for some small systems available with ED. From top to bottom, the symmetry-resolved entanglement results shown correspond to the following particle number sectors:  $n_{\max}$ ,  $n_{\max} - 1$ , and  $n_{\max} - 2$ , where  $n_{\max}$  is the sector at which the probability distribution of local particle number in the subregion,  $P_n$ , is maximal. For all systems, the partition size has been set to half of the total system size,  $\ell = L/2$ . The  $n_{\max} - 1$  curve illustrates a result that has been confirmed in this thesis analytically and numerically with PIGSFLI, that  $s_2(n_{\max} - 1)$  vanishes in the superfluid phase and it becomes  $\ln 2$  deep into the Mott phase. Note that even for these small systems, some interesting behavior is already exhibited. The  $n_{\max}$  and  $n_{\max} - 2$  curves exhibit peaks near the phase transition, denoted by the vertical line, that grow larger with system size. A peak has also been previously identified for the accessible entanglement as a function of interaction strength in the  $1d$  Bose-Hubbard model [41]. The PIGSFLI algorithm will allow for the simulation of much larger systems that may help understand any potential scaling of these peaks.

### 6.1.3 Accessible and symmetry-resolved entanglement in two dimensions

In chapter 3, to show the effectiveness of the PIGSFLI algorithm in higher dimensions, the second Rényi entanglement entropy was computed for a  $2d$  system of square geometry with an embedded square subregion. For this result, the entanglement was seen to obey a boundary law scaling near the superfluid-insulating phase transition.

For the accessible and symmetry-resolved entanglement entropies in  $2d$ , there is no theory for the scaling of these quantities and no numerical results in the literature. One of our goals moving forward will be to use PIGSFLI to simulate large  $2d$  systems, and eventually  $3d$ , and investigate the finite size scaling of both of these quantities.



**Figure 6.2:** Interaction dependence of the symmetry-resolved entanglement. These results have been obtained via exact diagonalization (ED). The maximal sector,  $n_{\max}$ , and the  $n_{\max} - 2$  sector peak near the superfluid-insulating phase transition (vertical line) although at different sides of it. We would like to use PIGSFLI to better understand the scaling of these peaks. For the  $n_{\max} - 1$  sector, the symmetry-resolved entanglement saturates at  $\ln 2$  in the insulating phase and vanishes in the superfluid, a result seen and explained in chapter 3 of this thesis.

Although not shown here, in the current version of our implementation, the geometry of the subregion can be also set to a strip extending from top to bottom of the square system, rather than a square, for which the width can be varied. For this type of geometry, previous QMC results have shown how the entanglement is constant as a function of system size, since changing the width of the strip does not change the boundary size between subregions [66]. Thus, our current implementation of the PIGSFLI algorithm will allow for one of the first studies of accessible and symmetry-resolved entanglement entropies for two dimensional Bose-Hubbard models, with different types of subsystem geometries, and across any regime of the phase diagram.

We hope that our new algorithm introduced in this thesis opens up these and many more new exciting avenues of research in ultra cold lattice systems in the context of quantum information, condensed matter, and beyond.

# Bibliography

- [1] E. Casiano-Diaz, C. M. Herdman, and A. D. Maestro. “A path integral ground state Monte Carlo algorithm for entanglement of lattice bosons.” *SciPost Phys.* **14**, 054 (2023).  
<https://scipost.org/10.21468/SciPostPhys.14.3.054> vii, 6, 11, 110, 124, 125, 127
- [2] E. Casiano-Diaz, K. Barros, Y. W. Li, and A. D. Maestro. “Reduction of autocorrelation times in lattice path integral quantum monte carlo via direct sampling of the truncated exponential distribution.” (2023). vii, 15
- [3] H. Barghathi, E. Casiano-Diaz, and A. Del Maestro. “Particle partition entanglement of one dimensional spinless fermions.” *J. Stat. Mech. Theory Exp.* **2017**, 083108 (2017).  
<https://doi.org/10.1088/1742-5468/aa819a> viii, 1, 11, 66
- [4] T. Giamarchi. *Quantum Physics in One Dimension* (Oxford University Press, 2003). ISBN 9780198525004.  
<https://doi.org/10.1093/acprof:oso/9780198525004.001.0001> xxi, 19, 20, 99, 100, 106, 107
- [5] M. Thamm, H. Radhakrishnan, H. Barghathi, B. Rosenow, and A. Del Maestro. “One-particle entanglement for one-dimensional spinless fermions after an interaction quantum quench.” *Phys. Rev. B* **106**, 165116 (2022).  
<https://link.aps.org/doi/10.1103/PhysRevB.106.165116> 1



- [6] H. Radhakrishnan, M. Thamm, H. Barghathi, B. Rosenow, and A. D. Maestro. “A scaling function for the particle entanglement entropy of fermions.” (2023).
- [7] C. M. Herdman, P. N. Roy, R. G. Melko, and A. Del Maestro. “Particle entanglement in continuum many-body systems via quantum Monte Carlo.” *Phys. Rev. B* **89**, 140501 (2014).  
<https://journals.aps.org/prb/abstract/10.1103/PhysRevB.89.140501>  
1, 6, 11, 17, 24, 65, 66
- [8] M. B. Hastings, I. González, A. B. Kallin, and R. G. Melko. “Measuring Rényi Entanglement Entropy in Quantum Monte Carlo Simulations.” *Phys. Rev. Lett.* **104**, 157201 (2010).  
<https://journals.aps.org/prl/abstract/10.1103/PhysRevLett.104.157201> 7, 17, 24, 26, 66, 68, 77, 94, 97
- [9] C. M. Herdman and A. Del Maestro. “Particle partition entanglement of bosonic luttinger liquids.” *Phys. Rev. B* **91**, 184507 (2015).  
<https://link.aps.org/doi/10.1103/PhysRevB.91.184507> 17, 65, 97
- [10] C. M. Herdman, P. N. Roy, R. G. Melko, and A. Del Maestro. “Entanglement area law in superfluid  $4\text{He}$ .” *Nature Phys.* **13**, 556 (2017).  
<https://doi.org/10.1038/nphys4075> 18, 86
- [11] C. M. Herdman, S. Inglis, P. N. Roy, R. G. Melko, and A. Del Maestro. “Path-integral Monte Carlo method for Rényi entanglement entropies.” *Phys. Rev. E* **90**, 013308 (2014).  
<https://journals.aps.org/pre/abstract/10.1103/PhysRevE.90.013308>  
17, 24, 65, 97
- [12] C. M. Herdman, P.-N. Roy, R. G. Melko, and A. D. Maestro. “Spatial entanglement entropy in the ground state of the Lieb-Liniger model.” *Phys.*

Rev. B **94** (2016).

<https://doi.org/10.1103/PhysRevB.94.064524> 17, 94

- [13] N. M. Tubman and D. C. Yang. “Calculating the entanglement spectrum in quantum Monte Carlo with application to ab initio Hamiltonians.” Phys. Rev. B **90** (2014).

<https://doi.org/10.1103/PhysRevB.90.081116> 65

- [14] C.-M. Chung, L. Bonnes, P. Chen, and A. M. Läuchli. “Entanglement spectroscopy using quantum Monte Carlo.” Phys. Rev. B **89**, 195147 (2014).

<https://link.aps.org/doi/10.1103/PhysRevB.89.195147>

- [15] S. Humeniuk and T. Roscilde. “Quantum Monte Carlo calculation of entanglement Rényi entropies for generic quantum systems.” Phys. Rev. B **86**, 235116 (2012).

<https://link.aps.org/doi/10.1103/PhysRevB.86.235116> 24

- [16] S. Inglis and R. G. Melko. “Entanglement at a two-dimensional quantum critical point: a  $T = 0$  projector quantum Monte Carlo study.” New J. Phys. **15**, 073048 (2013).

<https://doi.org/10.1088/1367-2630/15/7/073048> 65

- [17] T. Grover. “Entanglement of interacting fermions in quantum Monte Carlo calculations.” Phys. Rev. Lett. **111**, 130402 (2013).

<https://link.aps.org/doi/10.1103/PhysRevLett.111.130402> 6, 11, 24

- [18] R. Islam, R. Ma, P. M. Preiss, M. E. Tai, A. Lukin, M. Rispoli, and M. Greiner. “Measuring entanglement entropy in a quantum many-body system.” Nature **528**, 77 (2015).

<https://doi.org/10.1038/nature15750> 6, 20, 24, 25, 86, 97, 132

- [19] A. Lukin, M. Rispoli, R. Schittko, M. E. Tai, A. M. Kaufman, S. Choi, V. Khemani, J. Léonard, and M. Greiner. “Probing entanglement in a many-body-localized system.” *Science* **364**, 256 (2019).  
<https://science.sciencemag.org/content/364/6437/256> 24, 25
- [20] A. J. Daley, H. Pichler, J. Schachenmayer, and P. Zoller. “Measuring entanglement growth in quench dynamics of bosons in an optical lattice.” *Phys. Rev. Lett.* **109**, 020505 (2012).  
<https://link.aps.org/doi/10.1103/PhysRevLett.109.020505> 6, 24, 97
- [21] H. M. Wiseman and J. A. Vaccaro. “Entanglement of indistinguishable particles shared between two parties.” *Phys. Rev. Lett.* **91** (2003).  
<https://doi.org/10.1103/PhysRevLett.91.097902> 7, 8, 26, 67, 88, 97, 98
- [22] H. Barghathi, C. Herdman, and A. Del Maestro. “Rényi generalization of the accessible entanglement entropy.” *Phys. Rev. Lett.* **121** (2018).  
<https://doi.org/10.1103/PhysRevLett.121.150501> 7, 8, 26, 67, 97, 98
- [23] H. A. Gersch and G. C. Knollman. “Quantum cell model for bosons.” *Phys. Rev.* **129**, 959 (1963).  
<https://link.aps.org/doi/10.1103/PhysRev.129.959> 9, 29, 96, 98, 124
- [24] J. Carrasquilla, S. R. Manmana, and M. Rigol. “Scaling of the gap, fidelity susceptibility, and Bloch oscillations across the superfluid-to-Mott-insulator transition in the one-dimensional Bose-Hubbard model.” *Phys. Rev. A* **87**, 043606 (2013).  
<https://journals.aps.org/pr/abstract/10.1103/PhysRevA.87.043606> 9, 12, 55, 81, 86, 99, 125

- [25] T. D. Kühner, S. R. White, and H. Monien. “One-dimensional Bose-Hubbard model with nearest-neighbor interaction.” *Phys. Rev. B* **61**, 12474 (2000).  
<https://link.aps.org/doi/10.1103/PhysRevB.61.12474>
- [26] J. K. Freericks and H. Monien. “Strong-coupling expansions for the pure and disordered Bose-Hubbard model.” *Phys. Rev. B* **53**, 2691 (1996).  
<https://link.aps.org/doi/10.1103/PhysRevB.53.2691>
- [27] N. Elstner and H. Monien. “Dynamics and thermodynamics of the Bose-Hubbard model.” *Phys. Rev. B* **59**, 12184 (1999).  
<https://link.aps.org/doi/10.1103/PhysRevB.59.12184> 86
- [28] T. D. Kühner and H. Monien. “Phases of the one-dimensional Bose-Hubbard model.” *Phys. Rev. B* **58**, R14741 (1998).  
<https://link.aps.org/doi/10.1103/PhysRevB.58.R14741>
- [29] V. A. Kashurnikov, A. V. Krasavin, and B. V. Svistunov. “Mott-insulator-superfluid-liquid transition in a one-dimensional bosonic Hubbard model: Quantum Monte Carlo method.” *J. Exp. Theor. Phys.* **64**, 99 (1996).  
<https://doi.org/10.1134/1.567139>
- [30] V. A. Kashurnikov and B. V. Svistunov. “Exact diagonalization plus renormalization-group theory: Accurate method for a one-dimensional superfluid-insulator-transition study.” *Phys. Rev. B* **53**, 11776 (1996).  
<https://link.aps.org/doi/10.1103/PhysRevB.53.11776>
- [31] S. Ejima, H. Fehske, and F. Gebhard. “Dynamic properties of the one-dimensional Bose-Hubbard model.” *EPL (Europhysics Letters)* **93**, 30002 (2011).  
<https://doi.org/10.1209/0295-5075/93/30002>
- [32] J. Zakrzewski and D. Delande. “Accurate determination of the superfluid-insulator transition in the one-dimensional Bose-Hubbard model.” *AIP*

Conference Proceedings **1076**, 292 (2008).

<https://aip.scitation.org/doi/abs/10.1063/1.3046265>

- [33] S. M. A. Rombouts, K. Van Houcke, and L. Pollet. “Loop updates for quantum Monte Carlo simulations in the canonical ensemble.” *Phys. Rev. Lett.* **96**, 180603 (2006).

<https://link.aps.org/doi/10.1103/PhysRevLett.96.180603>

- [34] W. Krauth. “Bethe ansatz for the one-dimensional boson Hubbard model.” *Phys. Rev. B* **44**, 9772 (1991).

<https://link.aps.org/doi/10.1103/PhysRevB.44.9772>

- [35] R. V. Pai, R. Pandit, H. R. Krishnamurthy, and S. Ramasesha. “One-dimensional disordered bosonic Hubbard model: A density-matrix renormalization group study.” *Phys. Rev. Lett.* **76**, 2937 (1996).

<https://link.aps.org/doi/10.1103/PhysRevLett.76.2937>

- [36] G. G. Batrouni, R. T. Scalettar, and G. T. Zimanyi. “Quantum critical phenomena in one-dimensional Bose systems.” *Phys. Rev. Lett.* **65**, 1765 (1990).

<https://link.aps.org/doi/10.1103/PhysRevLett.65.1765>

- [37] M. Pino, J. Prior, A. M. Somoza, D. Jaksch, and S. R. Clark. “Reentrance and entanglement in the one-dimensional Bose-Hubbard model.” *Phys. Rev. A* **86**, 023631 (2012).

<https://link.aps.org/doi/10.1103/PhysRevA.86.023631>

- [38] A. M. Läuchli and C. Kollath. “Spreading of correlations and entanglement after a quench in the one-dimensional Bose-Hubbard model.” *J. Stat. Mech. Theory Exp.* **2008**, P05018 (2008).

<https://doi.org/10.1088/1742-5468/2008/05/p05018> 86

- [39] S. Rachel, N. Laflorencie, H. F. Song, and K. Le Hur. “Detecting quantum critical points using bipartite fluctuations.” *Phys. Rev. Lett.* **108**, 116401 (2012).  
<https://link.aps.org/doi/10.1103/PhysRevLett.108.116401> 9, 20, 55, 86, 99, 106, 125, 135
- [40] C. Lanczos. “An iteration method for the solution of the eigenvalue problem of linear differential and integral operators.” *Journal of research of the National Bureau of Standards* **45**, 255 (1950). 11
- [41] H. Barghathi, C. Usadi, M. Beck, and A. Del Maestro. “Compact unary coding for bosonic states as efficient as conventional binary encoding for fermionic states.” *Phys. Rev. B* **105**, 121116 (2022).  
<https://journals.aps.org/prb/abstract/10.1103/PhysRevB.105.L121116> 12, 19, 21, 26, 66, 67, 81, 88, 90, 96, 98, 99, 102, 138
- [42] H. Barghathi, E. Casiano-Diaz, and A. Del Maestro. “Operationally accessible entanglement of one-dimensional spinless fermions.” *Phys. Rev. A* **100** (2019).  
<https://doi.org/10.1103/PhysRevA.100.022324> 20, 67, 98, 99, 100, 102, 103
- [43] M. Haque, O. S. Zozulya, and K. Schoutens. “Entanglement between particle partitions in itinerant many-particle states.” *J. Phys. A: Math. Theor.* **42**, 504012 (2009).  
<https://doi.org/10.1088/1751-8113/42/50/504012> 11, 66
- [44] S. R. White. “Density matrix formulation for quantum renormalization groups.” *Phys. Rev. Lett.* **69**, 2863 (1992).  
<https://link.aps.org/doi/10.1103/PhysRevLett.69.2863> 11
- [45] I. Peschel, M. Kaulke, X. Wang, and K. Hallberg. *Density-Matrix Renormalization: A New Numerical Method in Physics Lectures of a Seminar*

*and Workshop Held at the Max-Planck-Institut für Physik komplexer Systeme Dresden, Germany, August 24th to September 18th, 1998*, volume 528 of *Lecture Notes in Physics* (Springer Berlin Heidelberg, Berlin, Heidelberg, 1999). ISBN 3642085415. 12

- [46] U. Schollwöck. “The density-matrix renormalization group in the age of matrix product states.” *Annals of Physics* **326**, 96 (2011). January 2011 Special Issue.  
<https://www.sciencedirect.com/science/article/pii/S0003491610001752>
- [47] F. Verstraete, V. Murg, and J. Cirac. “Matrix product states, projected entangled pair states, and variational renormalization group methods for quantum spin systems.” *Advances in Physics* **57**, 143 (2008).  
<https://doi.org/10.1080/14789940801912366>
- [48] I. P. McCulloch. “From density-matrix renormalization group to matrix product states.” *Journal of Statistical Mechanics: Theory and Experiment* **2007**, P10014 (2007).  
<https://dx.doi.org/10.1088/1742-5468/2007/10/P10014> 11
- [49] J. M. Zhang and R. X. Dong. “Exact diagonalization: the bose–hubbard model as an example.” *European Journal of Physics* **31**, 591 (2010).  
<https://dx.doi.org/10.1088/0143-0807/31/3/016> 12
- [50] A. M. Läuchli. “Operator content of real-space entanglement spectra at conformal critical points.” *arXiv: Statistical Mechanics* (2013). 12
- [51] P. Young. “Everything you wanted to know about data analysis and fitting but were afraid to ask.” (2014). 15
- [52] V. Ambegaokar and M. Troyer. “Estimating errors reliably in Monte Carlo simulations of the ehrenfest model.” *American Journal of Physics* **78**, 150

(2010).

<https://doi.org/10.1119/1.3247985> 15

[53] F. Becca and S. Sorella. *Quantum Monte Carlo Approaches for Correlated Systems* (Cambridge University Press, 2017). 15

[54] N. Metropolis, A. W. Rosenbluth, M. N. Rosenbluth, A. H. Teller, and E. Teller. “Equation of state calculations by fast computing machines.” *The Journal of Chemical Physics* **21**, 1087 (1953).

<https://doi.org/10.1063/1.1699114> 15, 109

[55] D. M. Ceperley. “Path integrals in the theory of condensed helium.” *Rev. Mod. Phys.* **67**, 279 (1995).

<https://journals.aps.org/rmp/abstract/10.1103/RevModPhys.67.279>  
17, 24

[56] A. Sarsa, K. E. Schmidt, and W. R. Magro. “A path integral ground state method.” *J. Chem. Phys.* **113**, 1366 (2000).

<https://aip.scitation.org/doi/10.1063/1.481926> 17, 25

[57] N. V. Prokof’ev, B. V. Svistunov, and I. S. Tupitsyn. “Exact, complete, and universal continuous-time worldline Monte Carlo approach to the statistics of discrete quantum systems.” *J. Exp. Theor. Phys* **87**, 310 (1998).

<https://link.springer.com/article/10.1134/1.558661> 17, 18, 24, 32, 34,  
121, 124

[58] N. Prokof’ev and B. Svistunov. “Worm algorithms for classical statistical models.” *Phys. Rev. Lett.* **87**, 160601 (2001).

<https://journals.aps.org/prl/abstract/10.1103/PhysRevLett.87.160601> 24, 25, 122

[59] N. Sadoune and L. Pollet. “Efficient and scalable Path Integral Monte Carlo Simulations with worm-type updates for Bose-Hubbard and XXZ models.”



(2022).

<https://arXiv.org/abs/2204.12262> 25

- [60] B. Bauer, L. D. Carr, H. G. Evertz, A. Feiguin, J. Freire, S. Fuchs, L. Gamper, J. Gukelberger, E. Gull, S. Guertler, A. Hehn, R. Igarashi, S. V. Isakov, D. Koop, P. N. Ma, P. Mates, H. Matsuo, O. Parcollet, G. Pawłowski, J. D. Picon, L. Pollet, E. Santos, V. W. Scarola, U. Schollwöck, C. Silva, B. Surer, S. Todo, S. Trebst, M. Troyer, M. L. Wall, P. Werner, and S. Wessel. “The ALPS project release 2.0: open source software for strongly correlated systems.” *J. Stat. Mech. Theory Exp.* **2011**, P05001 (2011).  
<https://doi.org/10.1088/1742-5468/2011/05/p05001> 17, 25
- [61] N. V. Prokof’ev, B. V. Svistunov, and I. S. Tupitsyn. ““Worm” algorithm in quantum Monte Carlo simulations.” *Phys. Lett. A* **238**, 253 (1998).  
[https://doi.org/10.1016/s0375-9601\(97\)00957-2](https://doi.org/10.1016/s0375-9601(97)00957-2) 17, 18, 24, 122
- [62] M. Srednicki. “Entropy and area.” *Phys. Rev. Lett.* **71**, 666 (1993).  
<http://dx.doi.org/10.1103/PhysRevLett.71.666> 18, 66, 86
- [63] J. Eisert, M. Cramer, and M. B. Plenio. “Colloquium: Area laws for the entanglement entropy.” *Reviews of Modern Physics* **82**, 277 (2010).  
<https://doi.org/10.1103/RevModPhys.82.277> 66
- [64] M. M. Wolf, F. Verstraete, M. B. Hastings, and J. I. Cirac. “Area Laws in Quantum Systems: Mutual Information and Correlations.” *Phys. Rev. Lett.* **100**, 070502 (2008).  
<https://journals.aps.org/prl/abstract/10.1103/PhysRevLett.100.070502> 18, 86
- [65] J. D. Bekenstein. “Black holes and entropy.” *Phys. Rev. D* **7**, 2333 (1973).  
<https://link.aps.org/doi/10.1103/PhysRevD.7.2333> 18

- [66] A. B. Kallin, M. B. Hastings, R. G. Melko, and R. R. P. Singh. “Anomalies in the entanglement properties of the square-lattice Heisenberg model.” *Phys. Rev. B* **84** (2011).  
<https://doi.org/10.1103/PhysRevB.84.165134> 66, 88, 140
- [67] M. A. Metlitski and T. Grover. “Entanglement entropy of systems with spontaneously broken continuous symmetry.” (2011).  
<https://arXiv.org/abs/1112.5166> 18, 19, 88
- [68] H. F. Song, N. Laflorencie, S. Rachel, and K. Le Hur. “Entanglement entropy of the two-dimensional Heisenberg antiferromagnet.” *Phys. Rev. B* **83**, 224410 (2011).  
<https://link.aps.org/doi/10.1103/PhysRevB.83.224410> 66
- [69] I. Frérot and T. Roscilde. “Entanglement entropy across the superfluid-insulator transition: A signature of bosonic criticality.” *Phys. Rev. Lett.* **116**, 190401 (2016).  
<https://link.aps.org/doi/10.1103/PhysRevLett.116.190401> 81, 88
- [70] D. J. Luitz, X. Plat, F. Alet, and N. Laflorencie. “Universal logarithmic corrections to entanglement entropies in two dimensions with spontaneously broken continuous symmetries.” *Phys. Rev. B* **91**, 155145 (2015).  
<https://link.aps.org/doi/10.1103/PhysRevB.91.155145>
- [71] B. Kulchytskyi, C. M. Herdman, S. Inglis, and R. G. Melko. “Detecting goldstone modes with entanglement entropy.” *Phys. Rev. B* **92**, 115146 (2015).  
<https://link.aps.org/doi/10.1103/PhysRevB.92.115146>
- [72] E. M. Stoudenmire, P. Gustainis, R. Johal, S. Wessel, and R. G. Melko. “Corner contribution to the entanglement entropy of strongly interacting  $o(2)$  quantum critical systems in 2+1 dimensions.” *Phys. Rev. B* **90**, 235106 (2014).  
<https://link.aps.org/doi/10.1103/PhysRevB.90.235106> 19, 88

- [73] P. Calabrese and J. Cardy. “Entanglement entropy and quantum field theory.” *J. Stat. Mech. Theory Exp.* **2004**, P06002 (2004).  
<https://doi.org/10.1088/1742-5468/2004/06/p06002> 19, 24, 25, 97
- [74] P. Calabrese and J. Cardy. “Entanglement entropy and conformal field theory.” *Journal of Physics A: Mathematical and Theoretical* **42**, 504005 (2009).  
<https://dx.doi.org/10.1088/1751-8113/42/50/504005> 19
- [75] S. Nishimoto. “Tomonaga-luttinger-liquid criticality: Numerical entanglement entropy approach.” *Phys. Rev. B* **84**, 195108 (2011).  
<https://link.aps.org/doi/10.1103/PhysRevB.84.195108> 19, 100
- [76] H. F. Song, S. Rachel, C. Flindt, I. Klich, N. Laflorencie, and K. Le Hur. “Bipartite fluctuations as a probe of many-body entanglement.” *Phys. Rev. B* **85**, 035409 (2012).  
<https://link.aps.org/doi/10.1103/PhysRevB.85.035409> 20, 135, 136
- [77] H. F. Song, S. Rachel, and K. Le Hur. “General relation between entanglement and fluctuations in one dimension.” *Phys. Rev. B* **82**, 012405 (2010).  
<https://link.aps.org/doi/10.1103/PhysRevB.82.012405> 20, 135
- [78] B. Estienne, Y. Ikhlef, and A. Morin-Duchesne. “Finite-size corrections in critical symmetry-resolved entanglement.” *SciPost Phys.* **10**, 54 (2021).  
<https://scipost.org/10.21468/SciPostPhys.10.3.054> 21, 67, 98, 104, 134
- [79] J. C. Xavier, F. C. Alcaraz, and G. Sierra. “Equipartition of the entanglement entropy.” *Phys. Rev. B* **98**, 041106 (2018).  
<https://link.aps.org/doi/10.1103/PhysRevB.98.041106> 21, 104
- [80] E. Casiano-Diaz, C. Herdman, and A. Del Maestro. “PIGSFLI - Path Integral Ground State For Lattice Implementations.” <https://github.com/DelMaestroGroup/pigsfli> (2022).  
<https://doi.org/10.5281/zenodo.6885505> 21, 23, 25, 94, 129, 168

- [81] E. Casiano-Diaz, C. Herdman, and A. Del Maestro. “PIGSFLI benchmarking dataset.” (2022).  
<https://doi.org/10.5281/zenodo.6827186> 23
- [82] E. Casiano-Diaz, K. Barros, Y. Wai Li, and A. Del Maestro. “Truncated exponential sampling dataset.” (2023).  
<https://doi.org/10.5281/zenodo.7566332> 23, 129
- [83] E. Casiano-Diaz, C. Herdman, and A. Del Maestro. “All code, scripts and data used in this work are included in a GitHub repository.” <https://github.com/DelMaestroGroup/papers-code-pigsfli> (2022).  
<https://doi.org/10.5281/zenodo.6885517> 23
- [84] E. Casiano-Diaz, K. Barros, Y. Wai Li, and A. Del Maestro. “All code, scripts and data used in this work are included in a GitHub repository.” <https://github.com/DelMaestroGroup/papers-code-truncExponSampling> (2023).  
<https://github.com/DelMaestroGroup/papers-code-truncExponSampling> 23, 129
- [85] J. McMinis and N. M. Tubman. “Rényi entropy of the interacting Fermi liquid.” *Phys. Rev. B* **87**, 081108 (2013).  
<https://journals.aps.org/prb/abstract/10.1103/PhysRevB.87.081108> 24, 65
- [86] R. G. Melko, A. B. Kallin, and M. B. Hastings. “Finite-size scaling of mutual information in Monte Carlo simulations: Application to the spin- $\frac{1}{2}$   $XXZ$  model.” *Phys. Rev. B* **82**, 100409 (2010).  
<https://journals.aps.org/prb/abstract/10.1103/PhysRevB.82.100409> 24, 65

- [87] R. R. P. Singh, M. B. Hastings, A. B. Kallin, and R. G. Melko. “Finite-temperature critical behavior of mutual information.” *Phys. Rev. Lett.* **106**, 135701 (2011).  
<https://link.aps.org/doi/10.1103/PhysRevLett.106.135701>
- [88] S. Inglis and R. G. Melko. “Wang-Landau method for calculating Rényi entropies in finite-temperature quantum Monte Carlo simulations.” *Phys. Rev. E* **87**, 013306 (2013).  
<https://journals.aps.org/pre/abstract/10.1103/PhysRevE.87.013306>  
[24](#), [65](#)
- [89] M. Boninsegni, N. Prokof’ev, and B. Svistunov. “Worm algorithm for continuous-space path integral Monte Carlo simulations.” *Phys. Rev. Lett.* **96**, 070601 (2006). [24](#), [32](#), [122](#)
- [90] M. Troyer, F. Alet, S. Trebst, and S. Wessel. “Non-local updates for quantum Monte Carlo simulations.” *AIP Conference Proceedings* **690**, 156 (2003).  
<https://aip.scitation.org/doi/abs/10.1063/1.1632126>
- [91] L. Pollet, K. V. Houcke, and S. M. Rombouts. “Engineering local optimality in quantum Monte Carlo algorithms.” *J. Comput. Phys* **225**, 2249 (2007).  
<https://www.sciencedirect.com/science/article/pii/S0021999107001295> [24](#)
- [92] M. Boninsegni, N. V. Prokof’ev, and B. V. Svistunov. “Worm algorithm and diagrammatic Monte Carlo: A new approach to continuous-space path integral Monte Carlo simulations.” *Phys. Rev. E* **74**, 036701 (2006). [25](#), [32](#), [122](#)
- [93] Y. Yan and D. Blume. “Path integral Monte Carlo ground state approach: formalism, implementation, and applications.” *J. Phys. B: At. Mol. Opt. Phys* **50**, 223001 (2017).  
<https://doi.org/10.1088/1361-6455/aa8d7f> [25](#)

- [94] G. Carleo, F. Becca, S. Moroni, and S. Baroni. “Reptation quantum Monte Carlo algorithm for lattice Hamiltonians with a directed-update scheme.” *Phys. Rev. E* **82**, 046710 (2010).  
<https://link.aps.org/doi/10.1103/PhysRevE.82.046710> 25
- [95] M. Greiner, O. Mandel, T. Esslinger, T. W. Hansch, and I. Bloch. “Quantum phase transition from a superfluid to a Mott insulator in a gas of ultracold atoms.” *Nature* **415**, 39 (2002).  
<http://www.nature.com/nature/journal/v415/n6867/abs/415039a.html> 25
- [96] W. S. Bakr, A. Peng, M. E. Tai, R. Ma, J. Simon, J. I. Gillen, S. Fölling, L. Pollet, and M. Greiner. “Probing the superfluid-to-Mott insulator transition at the single-atom level.” *Science* **329**, 547 (2010).  
<http://www.sciencemag.org/content/329/5991/547.abstract?sid=f6a968f6-0145-4d06-995c-716afa5dd0d8> 25, 66
- [97] S. Trotzky, L. Pollet, F. Gerbier, U. Schnorrberger, I. Bloch, N. V. Prokofev, B. Svistunov, and M. Troyer. “Suppression of the critical temperature for superfluidity near the Mott transition.” *Nature Phys.* **6**, 998 (2010).  
<http://www.nature.com/nphys/journal/v6/n12/full/nphys1799.html> 25, 66
- [98] M. Goldstein and E. Sela. “Symmetry-resolved entanglement in many-body systems.” *Phys. Rev. Lett.* **120**, 200602 (2018).  
<https://link.aps.org/doi/10.1103/PhysRevLett.120.200602> 26, 67, 98, 102
- [99] R. G. Melko, C. M. Herdman, D. Iouchtchenko, P.-N. Roy, and A. Del Maestro. “Entangling qubit registers via many-body states of ultracold atoms.” *Phys. Rev. A* **93**, 042336 (2016).  
<https://link.aps.org/doi/10.1103/PhysRevA.93.042336> 26, 67, 81, 88, 98

- [100] J. Silva-Valencia and A. M. C. Souza. “First Mott lobe of bosons with local two- and three-body interactions.” *Phys. Rev. A* **84**, 065601 (2011).  
<https://link.aps.org/doi/10.1103/PhysRevA.84.065601> 26
- [101] C. M. Herdman, A. Rommal, and A. Del Maestro. “Quantum Monte Carlo measurement of the chemical potential of  $^4\text{He}$ .” *Phys. Rev. B* **89**, 224502 (2014).  
<https://link.aps.org/doi/10.1103/PhysRevB.89.224502> 29, 124, 168
- [102] N. M. Tubman and J. McMinis. “Rényi entanglement entropy of molecules: Interaction effects and signatures of bonding.” (2012).  
<https://arXiv.org/abs/1204.4731> 65
- [103] Y. Zhang, T. Grover, A. Turner, M. Oshikawa, and A. Vishwanath. “Quasiparticle statistics and braiding from ground-state entanglement.” *Phys. Rev. B* **85**, 235151 (2012).  
<https://link.aps.org/doi/10.1103/PhysRevB.85.235151>
- [104] A. Selem, C. M. Herdman, and K. B. Whaley. “Entanglement entropy at generalized Rokhsar-Kivelson points of quantum dimer models.” *Phys. Rev. B* **87**, 125105 (2013).  
<https://journals.aps.org/prb/abstract/10.1103/PhysRevB.87.125105>
- [105] J. Pei, S. Han, H. Liao, and T. Li. “The Rényi entanglement entropy of a general quantum dimer model at the RK point: a highly efficient algorithm.” *J. Condens. Matter Phys.* **26**, 035601 (2013).  
<https://doi.org/10.1088/0953-8984/26/3/035601>
- [106] P. Broecker and S. Trebst. “Rényi entropies of interacting fermions from determinantal quantum Monte Carlo simulations.” *J. Stat. Mech. Theory Exp.* **2014**, P08015 (2014).  
<https://doi.org/10.1088/1742-5468/2014/P08015>

- [107] C.-M. Chung, V. Alba, L. Bonnes, P. Chen, and A. M. Läuchli. “Entanglement negativity via the replica trick: A quantum Monte Carlo approach.” *Phys. Rev. B* **90** (2014).  
<https://doi.org/10.1103/PhysRevB.90.064401>
- [108] R. J. C. Farias and M. C. de Oliveira. “Entanglement and the Mott insulator–superfluid phase transition in bosonic atom chains.” *J. Condens. Matter Phys.* **22**, 245603 (2010).  
<https://doi.org/10.1088/0953-8984/22/24/245603>
- [109] L. Amico, R. Fazio, A. Osterloh, and V. Vedral. “Entanglement in many-body systems.” *Rev. Mod. Phys.* **80**, 517 (2008).  
<https://link.aps.org/doi/10.1103/RevModPhys.80.517>
- [110] M. Levin and X.-G. Wen. “Detecting topological order in a ground state wave function.” *Phys. Rev. Lett.* **96**, 110405 (2006).  
<https://link.aps.org/doi/10.1103/PhysRevLett.96.110405>
- [111] M. B. Hastings. “An area law for one-dimensional quantum systems.” *J. Stat. Mech. Theory Exp.* **2007**, P08024 (2007).  
<https://doi.org/10.1088/1742-5468/2007/08/p08024>
- [112] H. Casini and M. Huerta. “Entanglement entropy for the n-sphere.” *Physics Letters B* **694**, 167 (2010).  
<https://www.sciencedirect.com/science/article/pii/S0370269310011548>
- [113] S. Murciano, P. Ruggiero, and P. Calabrese. “Symmetry resolved entanglement in two-dimensional systems via dimensional reduction.” *J. Stat. Mech. Theory Exp.* **2020**, 083102 (2020).  
<https://doi.org/10.1088/1742-5468/aba1e5>



- [114] M. T. Tan and S. Ryu. “Particle number fluctuations, Rényi entropy, and symmetry-resolved entanglement entropy in a two-dimensional fermi gas from multidimensional bosonization.” *Phys. Rev. B* **101**, 235169 (2020).  
<https://link.aps.org/doi/10.1103/PhysRevB.101.235169>
- [115] L. Capizzi, P. Ruggiero, and P. Calabrese. “Symmetry resolved entanglement entropy of excited states in a CFT.” *J. Stat. Mech. Theory Exp.* **2020**, 073101 (2020).  
<https://doi.org/10.1088/1742-5468/ab96b6>
- [116] S. Fraenkel and M. Goldstein. “Symmetry resolved entanglement: exact results in 1d and beyond.” *J. Stat. Mech. Theory Exp.* **2020**, 033106 (2020).  
<https://doi.org/10.1088/1742-5468/ab7753>
- [117] N. Feldman and M. Goldstein. “Dynamics of charge-resolved entanglement after a local quench.” *Phys. Rev. B* **100**, 235146 (2019).  
<https://link.aps.org/doi/10.1103/PhysRevB.100.235146>
- [118] R. Bonsignori, P. Ruggiero, and P. Calabrese. “Symmetry resolved entanglement in free fermionic systems.” *J. Phys. A Math* **52**, 475302 (2019).  
<https://doi.org/10.1088/1751-8121/ab4b77>
- [119] M. Kiefer-Emmanouilidis, R. Unanyan, J. Sirker, and M. Fleischhauer. “Bounds on the entanglement entropy by the number entropy in non-interacting fermionic systems.” *SciPost Phys.* **8**, 83 (2020).  
<https://scipost.org/10.21468/SciPostPhys.8.6.083>
- [120] S. Murciano, G. D. Giulio, and P. Calabrese. “Symmetry resolved entanglement in gapped integrable systems: a corner transfer matrix approach.” *SciPost Phys.* **8**, 46 (2020).  
<https://scipost.org/10.21468/SciPostPhys.8.3.046>

- [121] F. Benatti, R. Floreanini, F. Franchini, and U. Marzolino. “Entanglement in indistinguishable particle systems.” *Phys. Rep.* **878**, 1 (2020).  
<https://www.sciencedirect.com/science/article/pii/S0370157320302520>
- [122] X. Turkeshi, P. Ruggiero, V. Alba, and P. Calabrese. “Entanglement equipartition in critical random spin chains.” *Phys. Rev. B* **102**, 014455 (2020).  
<https://link.aps.org/doi/10.1103/PhysRevB.102.014455>
- [123] D. Faiez and D. Šafránek. “How much entanglement can be created in a closed system.” *Phys. Rev. B* **101**, 060401 (2020).  
<https://link.aps.org/doi/10.1103/PhysRevB.101.060401>
- [124] D. X. Horváth and P. Calabrese. “Symmetry resolved entanglement in integrable field theories via form factor bootstrap.” *J. High Energy Phys.* **2020**, 131 (2020).  
[https://doi.org/10.1007/jhep11\(2020\)131](https://doi.org/10.1007/jhep11(2020)131)
- [125] R. Bonsignori and P. Calabrese. “Boundary effects on symmetry resolved entanglement.” *J. Phys. A Math* **54**, 015005 (2020).  
<https://doi.org/10.1088/1751-8121/abcc3a>
- [126] C. de Groot, D. T. Stephen, A. Molnar, and N. Schuch. “Inaccessible entanglement in symmetry protected topological phases.” *J. Phys. A Math* **53**, 335302 (2020).  
<https://doi.org/10.1088/1751-8121/ab98c7>
- [127] S. Zhao, C. Northe, and R. Meyer. “Symmetry-resolved entanglement in  $ads_3/cft_2$  coupled to  $u(1)$  chern-simons theory.” *J. High Energy Phys.* **2021** (2021).  
[http://dx.doi.org/10.1007/jhep07\(2021\)030](http://dx.doi.org/10.1007/jhep07(2021)030)

- [128] S. Fraenkel and M. Goldstein. “Entanglement measures in a nonequilibrium steady state: Exact results in one dimension.” *SciPost Phys.* **11** (2021).  
<http://dx.doi.org/10.21468/SciPostPhys.11.4.085>
- [129] D. X. Horváth, L. Capizzi, and P. Calabrese. “U(1) symmetry resolved entanglement in free 1+1 dimensional field theories via form factor bootstrap.” *J. High Energy Phys.* **2021**, 197 (2021).  
[https://doi.org/10.1007/jhep05\(2021\)197](https://doi.org/10.1007/jhep05(2021)197)
- [130] G. Perez, R. Bonsignori, and P. Calabrese. “Quasiparticle dynamics of symmetry-resolved entanglement after a quench: Examples of conformal field theories and free fermions.” *Phys. Rev. B* **103**, L041104 (2021).  
<https://link.aps.org/doi/10.1103/PhysRevB.103.L041104>
- [131] L. Capizzi and P. Calabrese. “Symmetry resolved relative entropies and distances in conformal field theory.” *J. High Energy Phys.* **2021** (2021).  
[http://dx.doi.org/10.1007/jhep10\(2021\)195](http://dx.doi.org/10.1007/jhep10(2021)195)
- [132] S. Murciano, R. Bonsignori, , and P. Calabrese. “Symmetry decomposition of negativity of massless free fermions.” *SciPost Phys.* **10**, 111 (2021).  
<https://scipost.org/10.21468/SciPostPhys.10.5.111>
- [133] D. X. Horvath, P. Calabrese, and O. A. Castro-Alvaredo. “Branch Point Twist Field Form Factors in the sine-Gordon Model II: Composite Twist Fields and Symmetry Resolved Entanglement.” *SciPost Phys.* **12**, 88 (2022).  
<https://scipost.org/10.21468/SciPostPhys.12.3.088>
- [134] S. Scopa and D. X. Horváth. “Exact hydrodynamic description of symmetry-resolved Rényi entropies after a quantum quench.” (2022).  
<https://arXiv.org/abs/2205.02924>

- [135] L. Piroli, E. Vernier, M. Collura, and P. Calabrese. “Thermodynamic symmetry resolved entanglement entropies in integrable systems.” (2022).  
<https://arXiv.org/abs/2203.09158>
- [136] F. Ares, S. Murciano, and P. Calabrese. “Symmetry-resolved entanglement in a long-range free-fermion chain.” *J. Stat. Mech. Theory Exp.* **2022**, 063104 (2022).  
<https://doi.org/10.1088%2F1742-5468%2Fac7644>
- [137] N. Feldman, A. Kshetrimayum, J. Eisert, and M. Goldstein. “Entanglement estimation in tensor network states via sampling.” (2022).  
<https://arXiv.org/abs/2202.04089>
- [138] B. Oblak, N. Regnault, and B. Estienne. “Equipartition of entanglement in quantum hall states.” *Phys. Rev. B* **105** (2022).  
<https://doi.org/10.1103%2Fphysrevb.105.115131>
- [139] L. Capizzi, D. X. Horváth, P. Calabrese, and O. A. Castro-Alvaredo. “Entanglement of the 3-state Potts model via form factor bootstrap: total and symmetry resolved entropies.” *J. High Energy Phys.* **2022** (2022).  
<https://doi.org/10.1007%2Fjhep05%282022%29113>
- [140] K. Weisenberger, S. Zhao, C. Northe, and R. Meyer. “Symmetry-resolved entanglement for excited states and two entangling intervals in AdS3/CFT2.” *J. High Energy Phys.* **2021** (2021).  
<https://doi.org/10.1007%2Fjhep12%282021%29104>
- [141] P. Calabrese, J. Dubail, and S. Murciano. “Symmetry-resolved entanglement entropy in Wess-Zumino-Witten models.” *J. High Energy Phys.* **2021** (2021).  
<https://doi.org/10.1007%2Fjhep10%282021%29067>
- [142] G. Perez, R. Bonsignori, and P. Calabrese. “Exact quench dynamics of symmetry resolved entanglement in a free fermion chain.” *J. Stat. Mech. Theory*

Exp. **2021**, 093102 (2021).

<https://doi.org/10.1088%2F1742-5468%2Fac21d7>

- [143] A. Neven, J. Carrasco, V. Vitale, C. Kokail, A. Elben, M. Dalmonte, P. Calabrese, P. Zoller, B. Vermersch, R. Kueng, and B. Kraus. “Symmetry-resolved entanglement detection using partial transpose moments.” *Npj Quantum Inf.* **7** (2021).

<https://doi.org/10.1038%2Fs41534-021-00487-y>

- [144] T. J. Volkoff and C. M. Herdman. “Generating accessible entanglement in bosons via pair-correlated tunneling.” *Phys. Rev. A* **100**, 022331 (2019).

<https://link.aps.org/doi/10.1103/PhysRevA.100.022331>

- [145] S. Zhao, C. Northe, K. Weisenberger, and R. Meyer. “Charged moments in W3 higher spin holography.” *J. High Energy Phys.* **2022** (2022).

<https://doi.org/10.1007%2Fjhep05%282022%29166> 67, 98

- [146] P. Buonsante and A. Vezzani. “Ground-state fidelity and bipartite entanglement in the Bose-Hubbard model.” *Phys. Rev. Lett.* **98**, 110601 (2007).

<https://link.aps.org/doi/10.1103/PhysRevLett.98.110601> 81

- [147] M. Pino, J. Prior, A. M. Somoza, D. Jaksch, and S. R. Clark. “Reentrance and entanglement in the one-dimensional Bose-Hubbard model.” *Phys. Rev. A* **86**, 023631 (2012).

<https://journals.aps.org/pr/abstract/10.1103/PhysRevA.86.023631>

81

- [148] V. Alba, M. Haque, and A. M. Läuchli. “Entanglement spectrum of the two-dimensional Bose-Hubbard model.” *Phys. Rev. Lett.* **110**, 260403 (2013).

<https://link.aps.org/doi/10.1103/PhysRevLett.110.260403> 81

- [149] T. G. Kiely and E. J. Mueller. “Superfluidity in the one-dimensional Bose-Hubbard model.” *Phys. Rev. B* **105**, 134502 (2022).  
<https://link.aps.org/doi/10.1103/PhysRevB.105.134502>
- [150] Y. Zhang, L. Vidmar, and M. Rigol. “Information measures for local quantum phase transitions: Lattice bosons in a one-dimensional harmonic trap.” *Phys. Rev. A* **100**, 053611 (2019).  
<https://journals.aps.org/prabstract/10.1103/PhysRevA.100.053611>
- [151] K. Kottmann, A. Haller, A. Acín, G. E. Astrakharchik, and M. Lewenstein. “Supersolid-superfluid phase separation in the extended Bose-Hubbard model.” *Phys. Rev. B* **104**, 174514 (2021).  
<https://journals.aps.org/prb/abstract/10.1103/PhysRevB.104.174514>  
81
- [152] S. V. Isakov, M. B. Hastings, and R. G. Melko. “Topological entanglement entropy of a Bose-Hubbard spin liquid.” *Nature Phys.* **7**, 772 (2011).  
<https://www.nature.com/articles/nphys2036> 81
- [153] R. Ghosh, N. Dupuis, A. Sen, and K. Sengupta. “Entanglement measures and nonequilibrium dynamics of quantum many-body systems: A path integral approach.” *Phys. Rev. B* **101**, 245130 (2020).  
<https://link.aps.org/doi/10.1103/PhysRevB.101.245130> 81
- [154] B. Capogrosso-Sansone, e. G. Söyler, N. Prokof’ev, and B. Svistunov. “Monte Carlo study of the two-dimensional Bose-Hubbard model.” *Phys. Rev. A* **77**, 015602 (2008).  
<https://journals.aps.org/prabstract/10.1103/PhysRevA.77.015602>  
86

- [155] D. Hinrichs, A. Pelster, and M. Holthaus. “Perturbative calculation of critical exponents for the Bose–Hubbard model.” *Appl. Phys. B* **113**, 57 (2013).  
<https://doi.org/10.1007%2Fs00340-013-5419-0> 86
- [156] H. Casini and M. Huerta. “Universal terms for the entanglement entropy in 2+1 dimensions.” *Nucl. Phys. B*. **764**, 183 (2007).  
<https://www.sciencedirect.com/science/article/pii/S0550321306010091> 88
- [157] J. Helmes and S. Wessel. “Entanglement entropy scaling in the bilayer heisenberg spin system.” *Phys. Rev. B* **89**, 245120 (2014).  
<https://link.aps.org/doi/10.1103/PhysRevB.89.245120> 88
- [158] E. Casiano-Diaz, C. M. Herdman, and A. Del Maestro. “A path integral ground state Monte Carlo algorithm for entanglement of lattice bosons.” (2022).  
<https://arxiv.org/abs/2207.11301> 96, 97, 99
- [159] K. Binder and D. Heermann. *Monte Carlo Simulation in Statistical Physics: An Introduction*. Graduate Texts in Physics (Springer Berlin Heidelberg, 2010). ISBN 9783642031632. 109
- [160] W. Krauth. *Statistical Mechanics Algorithms and Computations* (Oxford University Press, Oxford, 2006). ISBN 9781429459501 1429459506.
- [161] N. Giordano and H. Nakanishi. *Computational Physics* (Pearson/Prentice Hall, 2006). ISBN 9780131469907. 109
- [162] G. E. Forsythe. “Von Neumann’s Comparison Method for Random Sampling from the Normal and Other Distributions.” *Math. Comput.* **26**, 817 (1972).  
111
- [163] M. E. J. Newman and G. T. Barkema. *Monte Carlo methods in statistical physics* (Clarendon Press, Oxford, 1999). 111

- [164] R. M. Corless, G. H. Gonnet, D. E. G. Hare, D. J. Jeffrey, and D. E. Knuth. “On the LambertW function.” *Adv. Comput. Math.* **5**, 329 (1996).  
<https://link.springer.com/article/10.1007/BF02124750> 116
- [165] T. Fukushima. “Precise and fast computation of Lambert W-functions without transcendental function evaluations.” *J. Comput. Appl. Math* **244**, 77 (2013).  
<https://linkinghub.elsevier.com/retrieve/pii/S0377042712005213> 117
- [166] W. H. Press and S. A. Teukolsky. “Kolmogorov-Smirnov test for two-dimensional data.” *Comput. Phys.* **2**, 74 (1988).  
<https://aip.scitation.org/doi/abs/10.1063/1.4822753> 117
- [167] A. Justel, D. Peña, and R. Zamar. “A multivariate Kolmogorov-Smirnov test of goodness of fit.” *Stat. Probab. Lett.* **35**, 251 (1997).  
<https://www.sciencedirect.com/science/article/pii/S0167715297000205> 117
- [168] C. Miles, B. Cohen-Stead, O. Bradley, S. Johnston, R. Scalettar, and K. Barros. “Dynamical tuning of the chemical potential to achieve a target particle number in grand canonical Monte Carlo simulations.” *Phys. Rev. E* **105**, 045311 (2022).  
<https://link.aps.org/doi/10.1103/PhysRevE.105.045311> 124
- [169] U. Wolff. “Critical slowing down.” *Nuclear Physics B - Proceedings Supplements* **17**, 93 (1990).  
[https://doi.org/10.1016/0920-5632\(90\)90224-i](https://doi.org/10.1016/0920-5632(90)90224-i) 125
- [170] D. Foreman-Mackey, D. W. Hogg, D. Lang, and J. Goodman. “emcee: The mcmc hammer.” *Publications of the Astronomical Society of the Pacific* **125**, 306 (2013).  
<https://dx.doi.org/10.1086/670067> 125



- [171] J. Goodman and J. Weare. “Ensemble samplers with affine invariance.” *Communications in Applied Mathematics and Computational Science* **5**, 65 (2010). [125](#)
- [172] A. D. Sokal. “Monte Carlo Methods in Statistical Mechanics: Foundations and New Algorithms Note to the Reader.” In “Functional Integration: Basics and Applications,” pages 131–192 (Springer US, 1996). [125](#)

# Appendix

# Appendix A

## Obtaining and Running the Code

In the spirit of promoting open science, the PIGSFLI source code has been made public and can be obtained from the Del Maestro Group code repository [80] via:

```
git clone https://github.com/DelMaestroGroup/pigsfli.git
```

After compiling the code following the instructions in the repository [80], the executable `pigsfli.e` will be generated and simulations can now be performed. An example call would be:

```
./pigsfli.e -D 1 -L 4 -N 4 -l 2 -U 1.995 --mu 1.998 --beta 2.001 --seed 1968
```

In the call above, only some parameters have been set from the command-line, with the rest being set to their default values. The full list of parameters can be found on the code repository or can be seen by calling `./pigsfli.e --help`.

In the first stage of the code, the chemical potential ( $\mu$ ) is updated using the method in [101] until the average number of particles is at least within 33% of the target number  $N$ . To improve sampling efficiency, worldline updates are rejected if they would take the total particle number outside the interval  $[N - 1, N + 1]$ . In this stage, we also simultaneously perform a coarse tuning of the worm fugacity ( $\eta$ ). We have chosen the coarse tuning to be  $\eta \approx 1/\langle N_{\text{flats}} \rangle$ , where  $\langle N_{\text{flats}} \rangle$  is the average number of flat regions sampled each time that a distribution  $P(N)$  was built.

A fine tuning of  $\eta$  is then performed until the fraction of worldline configurations with no worm ends, or diagonal fraction (`Z-frac` in the code output shown) is within

a desired window. This fraction needs to be low enough that physical observables can be measured, but high enough that worm ends are present to help push the dynamics of the worldline configuration forward. We've chosen a window between 40% and 45% for the target value of the diagonal fraction. The  $\eta$  updating is performed by asymmetrically increasing or decreasing its value by some multiplicative constant. For example, if the fraction is too low, we decrease  $\eta$  by 50% and if too high, increase it by 45%. Note that we still keep updating  $\mu$  in this stage in case that the new  $\eta$  causes the average total particle number to stray too far away from the target value.

After tuning  $\mu$  and  $\eta$ , there is an equilibration stage where worldline updates are performed for a chosen number of Monte Carlo sweeps, but no measurements are performed. The number of equilibration sweeps is set to a default value but can also be set from the command line.

And finally, the last stage is the main Monte Carlo loop, where not only worldline updates are performed, but also measurements of the desired quantities. After the main loop, the number of times that each update was accepted over the number of times it was proposed is shown. Notice that the “forward” and “backward” updates of each pair of complementary updates is accepted roughly the same time, as expected from the principle of detailed balance.

The code output for the example call above is:

```

      -      -- --
      (.)      / _| (.)
  _ _ _ _ _ _ _ _ _ _ | | | |
 | ' _ \ | / _ ' / _ | | | | | | |
 | | ) | | ( | \ _ \ | | | |
 | . _ / | _ \ _ , | _ _ / | | | |
 | |      _ _ / |
 | _ |      | _ _ /

Path-Integral Ground State (Monte Carlo) For Lattice Implementations

Stage (1/3): Determining mu and eta...

mu: 1.998 eta: 0.5 Z-frac: 13.004%
N      P(N)
4      **

```

```

5 *****
<N>: 4.98985

mu: -0.291113 eta: 0.153571 Z-frac: 18.221%
N P(N)
3 *****
4 *****
5 *****
<N>: 4.16743

Fine tuning eta... (Want: 10% < Z-frac < 15%)

mu: -0.291113 eta: 0.16197 Z-frac: 20.453%
N P(N)
3 ***
4 *****
5 *****
<N>: 4.4351

mu: -1.02474 eta: 0.0809852 Z-frac: 29.8528%
N P(N)
4 *****
5 *****
<N>: 4.24996

mu: -1.02474 eta: 0.0404926 Z-frac: 54.4598%
N P(N)
3 *****
4 *****
5 *****
<N>: 3.94856

mu: -1.02474 eta: 0.0587143 Z-frac: 40.3%
N P(N)
3 *****
4 *****
5 *****
<N>: 4.2089

Stage (2/3): Equilibrating...

Stage (3/3): Main Monte Carlo loop...

----- Detailed Balance -----

Insert Worm: 38470/2772581
Delete Worm: 36544/44720

Insert Anti: 37646/2090863
Delete Anti: 35628/39821

```

```
InsertZero Worm: 396535/6277132
DeleteZero Worm: 398573/475282

InsertZero Anti: 433392/4407244
DeleteZero Anti: 435430/522308

InsertBeta Worm: 396510/6280347
DeleteBeta Worm: 398416/476129

InsertBeta Anti: 432507/4409839
DeleteBeta Anti: 434413/519043

Advance Head: 1572275/1578564
Recede Head: 1572292/1597065

Advance Tail: 1573978/1598309
Recede Tail: 1575285/1581400

IKBH: 1508373/3785551
DKBH: 1509684/1697842

IKAH: 946308/3783103
DKAH: 945886/1120626

IKBT: 945858/2638223
DKBT: 945478/1119408

IKAT: 1508438/3787390
DKAT: 1507908/1697276

SWAP: 5932134/14723038
UNSWAP: 5932132/14811285

SWAP Advance Head: 313417/321052
SWAP Recede Head: 313426/344143

SWAP Advance Tail: 312995/342388
SWAP Recede Tail: 312737/319738

Elapsed time: 13.5167 seconds
```

In Stage (1/3), histograms of the total particle number distribution are shown, where each of the asterisks (\*) represents a normalized count. For canonical ensemble simulations, like the one shown above, the only particle numbers visited are  $N - 1$ ,  $N$ , and  $N + 1$ , where  $N$  is the target number of particles. A grand canonical simulation will show histograms with more particle numbers than these. Once the peak of the distribution is at  $N$ , and it's at least 33

Stage (2/3), the code is ran without taking any measurement as a en equilibration step. The number of equilibration steps are currently determined by the sweeps parameter from the command line.

Finally, Stage (3/3) is where measurements are performed and samples collected. Once the desired number of samples are collected, the simulation stops. Near the bottom of the terminal output above, the number of times that each of the updates is accepted and proposed are shown as a fraction. The number of times that the update is accepted is shown in the numerator, whereas the times that it was proposed is shown in the denominator.

The total run time of equilibration and Main Monte Carlo loops is shown at the bottom of the output, in seconds.

# Vita

Emanuel Casiano-Diaz was born in Puerto Rico, where he grew up in the city of Bayamón. He attended a middle and high school in San Juan specialized in the training of classical musicians. Afterwards, he attended the University of Puerto Rico, Rio Piedras, where he received a Bachelor's degree in Physics and discovered in his Senior year a passion for scientific computing. After taking a year off from his own academic pursuits to work as a high school math teacher in his hometown, he decided to pursue a Master's degree in Physics at University of Vermont, under the supervision of Dr. Adrian Del Maestro. Motivated by this Master's project, he then decided to also pursue a Physics PhD, once again under the supervision of Dr. Adrian Del Maestro, this time at The University of Tennessee Knoxville. For his PhD project, he developed a quantum Monte Carlo algorithm for the simulation of bosonic lattices at zero temperature. His research interests include computational physics, quantum entanglement measures, and algorithmic development, with education and music being two of his other core interests. He is beyond grateful for the education received from his teachers of the Puerto Rico public school system and from his university professors in Puerto Rico, Vermont, and Tennessee. He would also like to thank his family and loved ones for their never ending support so he could stand here today defending his Physics PhD.